HUNGARIAN UNIVERSITY OF
AGRICULTURE AND LIFE SCIENCES

Experimental and DEM model of abrasion of rotary shaft/seal contact with lunar regolith simulants

PhD. Dissertation

by

Hailemariam Shegawu

Gödöllő

2025

Doctoral School and Program denomination:

Doctoral School of Engineering Sciences
Doctoral Program of Mechanical Engineering

Science: Engineering

Head of School: Prof. Dr. László Bozó, MHAS
Institute of Environmental Sciences
Hungarian University of Agriculture and Life Science, Budapest,
Hungary

Program leader: Prof. Dr. Gábor Kalácska, DSc
Institute of Technology
Hungarian University of Agriculture and Life Science, Gödöllő,
Hungary

Supervisor: Prof. Dr. Gábor Kalácska, DSc
Institute of Technology
Hungarian University of Agriculture and Life Science, Gödöllő,
Hungary

Co-Supervisor: Prof. Dr. István Keppler, PhD
Institute of Technology
Hungarian University of Agriculture and Life Science, Gödöllő,
Hungary

…………………………………   …………………………………………

Affirmation of supervisor(s)   Affirmation of head of doctoral program

CONTENT

LIST OF ABBREVIATIONS AND SYMBOLS

SEM	Scanning electron Microscopy
EDX	Energy-dispersive X-ray spectroscopy
PoD	Pin-on-Disc tribo-system
PTFE	Polytetrafluoroethylene
LHS1	Lunar Highland Simulant
LMS1	Lunar Mare Simulant
MGS1	Mars Global simulant
JEZ1	Martian Jezero crater Simulant
F_N	Normal force [N]
μ	Friction coefficient [-]
v	Sliding speed [m/s]
Dp	A non-standard, domain-specific tribological parameter: The "Degree of Penetration"
SS	Stainless Steel
ASTM	American Society for Testing and Materials
EN	European Norm Standards
DIN	Deutsches Institut für Normung Standards
Rx	Run x time [min]
HV0.3	Micro-hardness, HV
E	Modulus of elasticity [MPa]
GF	Glass fibre
MoS2	Molybdenum disulphide
ESMATS	European Space Mechanisms and Tribology Symposium
SPSS	Statistical Package for the Social Sciences
Ra	2D measure, Arithmetical mean roughness [μm]
Rz	2D measure, "Peak-to-valley" roughness [μm]
Rq	2D measure, Root mean square roughness (RMS) [μm]
Ry	2D measure, Maximum Height of the Profile [μm]
Sa	3D measure, Arithmetic Mean Height [μm]
Sz	3D measure, Maximum Height of the Profile [μm]
Sq	3D measure, Root Mean Square Roughness [μm]
Ssk	3D measure, Skewness of the Profile [-]
Sku	3D measure, Kurtosis of the Profile [-]
PR	Relative ratio of particle size
τ	Shear strength of the contact junctions (material-dependent) [N/mm^2]
Ar	Real area of contact [mm^2]
V	wear volume [mm^3]

K	Dimensionless wear coefficient (material-dependent [-]
W	Normal load [N]
L	Sliding distance [mm]
H	Hardness of the softer material [N/mm^2]
α	Abrasive wear coefficient influenced by particle shape and hardness ratio [-]
σ	Contact stress) [N/mm^2]
m	Material-dependent exponent [-]
N	Number of loading cycles [-]
k	Wear coefficient, dependent on abrasive geometry and contact conditions [-]
Dp	Degree of penetration [-]
Rz	Ten point height [μm]
P_1	Average separation peak one [μm]
P_2	Average separation peak two [μm]
P_3	Average separation peak three [μm]
P_4	Average separation peak four [μm]
P_5	Average separation peak five [μm]
V_1	Average separation valley one [μm]
V_2	Average separation valley two [μm]
V_3	Average separation valley three [μm]
V_4	Average separation valley four [μm]
V_5	Average separation valley five [μm]
Rsm	Mean spacing at mean line [μm]
R_a	Roughness average [μm]
R_q	Root mean square roughness [μm]
R_t	Maximum peak to valley height [μm]
R_{max_1}	Largest single peak to valley height one [μm]
R_{max_2}	Largest single peak to valley height two [μm]
R_{max_3}	Largest single peak to valley height three [μm]
R_{max_4}	Largest single peak to valley height four[μm]
R_{max_5}	Largest single peak to valley height five [μm]
L	Sampling length [m]
z	Height of the profile along 'x' [m]
Wg	Individual load on the particle [μm]
d	Depth of indentation [-]
α	Slope angle of the cone [°]
σ_y	Materials yield stress under indentation [N/mm^2]
Vg	Volume of material removed by the cone [mm]

l	Distance travelled by the cone [mm]
V_{tot}	Total wear [mm³]
W_{tot}	Total load [N]
θ	Angle of attack [°]
P	Load [N]
H	Wear surface of hardness [N/mm²]
2w	Groove width [mm]
h	Groove height [mm]
L	Groove length [mm]
Λ	Groove area [mm²]
Ω	Projected penetration area [mm²]
TBM	Tunnel boring machine
SET	solid expandable tubular
PEEK	Polyether ether ketone
H_2	Chemical formula of hydrogen gas
JSC-1AF	Johnson Space Center (finer than 27μm)
NU-LHT-2 M	Northeastern University Lunar highland Simulant Type 2
JSC-1A	Johnson Space Center (finer than 1mm)
DMP	Dust Management Project
NASA	National Aeronautics and Space Administration
EVAS	Extravehicular Activity Systems
EMU	extravehicular mobility unit
MGS-1	Mars Global Simulants
JSC-1	Johnson Space Center-1
MLS-1	Minnesota Lunar Simulant
FJS-1	Fuji Japanese Simulant
FJS-2	Fuji Japanese Simulant (contains more olivine in FJS-1)
FJS-3	Fuji Japanese Simulant (produced by adding ilmenite and olivine in FJS-1)
TJ-1	Tong Ji University type 1 (contain low-titanium basaltic regolith)
TJ-2	Tong Ji University type 2
GRC-3	Glen Research Center type 3
CAS-1	Chinese Academy of Sciences type 1
BP-1	Black point one
JSC Mars-1	Johnson Space Center Martian dust simulant one
JPL Lab 107	Jet Propulsion Laboratory (JPL);consists of dust-free washed silica sand
JPL Lab 82	JPL; consists of dust-free washed ruby garnet mix
MER Yard 317	Indoor Mars Exploration Rover test facility
MMS sand I	Mojave Mars Simulant sand I (Basaltic simulant in rock, sand and dust form)

MMS sand II	Mojave Mars Simulant sand II (Basaltic simulant in rock, sand and dust form)
MMS dust I	Mojave Mars Simulant dust I
MMS dust II	Mojave Mars Simulant dust II
ES-1	Engineering Soil simulant-1 (sandy material, based upon Nepheline sternoy 7.)
ES-2	Engineering Soil simulant-2 (sandy material, based upon Red Hill 110.)
ES-3	Engineering Soil simulant-3 (sandy material, based upon Leighton buzzard DA 30)
JMSS-1	Jining Mars Soil Simulant Type 1
BEMA	Bogie Electro-Mechanical Assemblies
ESA	European Space Agency's
MDA	MacDonald Dettwiler and Associates
Roscosmos	European Space Agency and the Russian Space Agency
MER	Mars Exploration Rover
MI	Microscopic Imager
MB	Mössbauer Spectrometer
ISEM	Image scanning electron microscopy
JPL	Jet Propulsion Laboratory
MRP	Mercury Robotic Payload
SBGM	SEALED BRUSH GEAR MOTOR
DC	Direct electric current
GRC	Glenn Research Centre
GA	Greenland Anorthosite
DEM	Discrete Element Method
BPM	Bonded-particle model
CA	Cellular automata
V_1	velocity of particle one before contact
V_2	velocity of particle two before contact
V'_1	velocity of particle one after contact
V'_2	velocity of particle two after contact
JKR	Johnson, Kendall, and Roberts
DMT	Derjaguin, Muller, and Toporov
δ	Displacement [mm]
F_n	Normal contact force [N]
F_t	Tangential contact force [N]
δ_n	Normal displacement [mm]
δ_t	Tangential displacement [mm]
K_n	Normal spring constant[N/mm]
K_t	Tangential spring constant[N/mm]
E^*	Equivalent Young's modulus [MPa]

E_i	Young's modulus of i particle in contact [MPa]
E_j	Young's modulus of j particle in contact [MPa]
ν	Poisson's ratio of the two particles in contact [-]
ν_i	Poisson's ratio of the i particles in contact [-]
ν_j	Poisson's ratio of the j particles in contact [-]
$G*$	Equivalent shear modulus [MPa]
G_i	shear modulus of the i particles in contact [MPa]
G_j	shear modulus of the j particles in contact [MPa]
$R*$	Equivalent radius [mm]
R_i	particle radii of the i particles in contact [mm]
R_j	particle radii of the j particles in contact [mm]
F_c	Contact force [N]
F_h	Non-linear Hertz component [N]
F_d	Damping component [N]
C_n	Damping coefficients in the normal direction [-]
$\dot{\delta}_n$	Normal velocity in the normal direction [mm/s]
C_t	Damping coefficients in the shear direction [-]
$\dot{\delta}_t$	Tangential velocity in the tangential direction [mm/s]
e	Coefficient of restitution [-]
r_1	Position vector of spherical center one [mm]
r_2	Position vector of spherical center two [mm]
M_p	Torque of particle centre mass [N.m]
I_p	Particle's moment of inertia [kg.m^2]
β	Damping ratio [-]
$\overrightarrow{v_n^{rel}}$	Normal component of the relative velocity [mm/s]
$\overrightarrow{v_t^{rel}}$	Tangential component of the relative velocity [mm/s]
μ_s	Coefficient of static friction [-]
n_i	Total particle numbers contacting the particle i [-]
u_i	Translational velocity of the particle i [mm/s]
ω_i	Rotational velocity of the particle i [rad/s]
I_i	Rotational inertia of the particle i [kg.m^2]
$F_{cn,ij}$	Normal contact force between particle i and j [N]
$F_{ct,ij}$	Tangential contact force between particle i and j [N]
$F_{dn,ij}$	Normal damping force between particle i and j [N]
$F_{dt,ij}$	Tangential damping force between particle i and j [N]
g	Gravitation acceleration [m/s^2]
$T_{t,ij}$	Torque from tangential forces between particle i and j [N.m]

$M_{r,ij}$	Rolling friction torque between particle i and j [N.m]
ΔS	Sliding distance [m]
F_{body}	Body force [N]
$F_{surface}$	Surface (contact) force acting up on particle [N]
M	Resultant moment [Nms/rad]
T_{damp}	Damping moment [Nms/rad]
K_H	Stiffness coefficient [-]
C_H	Damping coefficient [-]
L_i	Contacting pair particle sizes [mm]
L	A single particle size for particle–boundary collision [mm]
μ_d	Dynamic friction coefficient [-]
$S_{t,max}$	Maximum relative tangential displacement [mm]
ΔV	Volume loss [mm^3]
ΔW^t	Shear work performed by particles [Nm]
C	Volume/shear work ratio [-]
F_{ij}^n	Normal contact force between particles i and j [N]
F_{ij}^{dn}	Normal damping force between particles i and j [N]
F_{ij}^t	Tangential contact force between particles i and j [N]
F_{ij}^{dt}	Tangential damping force between particles i and j [N]
F_{ij}^{bn}	Normal bonding force between particles i and j [N]
F_{ij}^{bt}	Tangential bonding force between particles i and j [N]
M_{ij}^t	Torques caused by tangential force between particles i and j [N.m]
M_{ij}^r	Torques caused by rolling friction between particles i and j [N.m]
M_{ij}^{bn}	Torques caused by normal bonding force between particles i and j [N.m]
M_{ij}^{bt}	Torques caused by tangential bonding force between particles i and j [N.m]
k_n	Bond normal stiffness [N/m]
k_t	Bond tangential stiffness [N/m]
R_B	Radius of rod like solid bond [mm]
R_i	Vector from the particle i centre point to the contact point [mm]
μ_r	Rolling coefficient of friction [-]
$\widehat{\omega}_{rel}$	Vector of relative angular velocity [rad/s]
$\Delta\theta_n$	Normal rotation angle in a time step [°]
$\Delta\theta_t$	Tangential rotation angle in a time step [°]
F^e	Elastic force in the spring [N]
F^v	Damping viscous components [N]
F^{sint}	Sintering force [N]

F^{ext}	External load [N]
a	Contact area [mm^2]
γ	Surface energy [J/m^2]
LSD	linear spring-dashpot model
F_l	Linear spring component [N]
F_d	Linear damping component [N]
$(F_l^t)_o$	Shear force at the end of the previous time step [N]
K_1	Spring constant in the loading stage [N/m]
K_2	Spring constant in the unloading stage [N/m]
δ_{n0}	Normal displacement when the unloading curve goes to zero [mm]
Y^1	Yield strength of material one participant in the contact [N/m^2]
Y^2	Yield strength of material two participant in the contact [N/m^2]
δ_0	Residual overlap [mm]
AoR	Angle of repose [°]
RR	Rolling resistance coefficient [-]
DF	Dynamic friction of the friction coefficients [-]
FEM	Finite Element Method
θ	Repose angle [°]
θ_1	Angle of repose one [°]
θ_2	Angle of repose two [°]
θ_{ave}	Average angle of repose [°]
W	Force [N]
F_s	Tangential force [N]
T_r	Resistance torque [Nm]
D_A	Diameter of bulk solid heap [mm]
D_a	Height of bulk solid heap [mm]
D	Width of repose angle [mm]
H	Height of repose angle [mm]
ΔE_τ	Shear work by the particles [Nm]
ΔQ	Volume wear loss [mm^3]
S	Sliding distance [mm]
L	Sliding force [N]
Δd_i	Depth [mm]
A_i	Area [mm^2]
W_{shear}	Shear work [Nm]
XX. century	Century spanning from 1901 to 2000
Early XXI. century	Interval from 2001 to circa 2010

2010s – 2020s	To a transition between two successive decades: the 2010s (2010-2019) and the 2020s (2020-2029)
Up-to mid of 2020s	Interval from January 1, 2020, to the midpoint of the decade, January 1, 2025
ESA 4000136800/21/NL/CBi	European Space Agency, grant number 4000136800/21/NL/CBi
Cr	Chromium
Ni	Nickel
Ln	natural PTFE lip seal material
RH	Relative humidity [%]
R2	Running time with two minutes [min]
R6	Running time with six minutes [min]
R15	Running time with fifteen minutes [min]
R30	Running time with thirty minutes [min]
x	Common symbol for magnification
X	A unit of distance previously employed for quantifying the wavelength of x-rays and gamma rays
α	Angle of repose [°]
AB	Line [mm]
AC	Line [mm]
AD	Line [mm]
α_{ave}	Average angle of repose [°]
α_1	Angle of repose value for experimental one [°]
α_2	Angle of repose value for experimental two [°]
α_3	Angle of repose value for experimental three [°]
α_4	Angle of repose value for experimental four [°]
α_5	Angle of repose value for experimental five [°]
AOR_{bottom}	angle of repose at the bottom of the powder heap [°]
n	normal direction
t	tangential direction
j	Number of contact point, j = 1,2 ...
$\delta_{n,j}$	Normal displacement, number of contact point [mm]
$\delta_{t,j}$	Tangential displacement, number of contact point [mm]
$F_{n,s}$	Normal contact force of Hertzian spring [N]
$F_{n,d}$	Normal contact force of Hertzian dashpot [N]
$F_{n,jkr}$	Normal contact force of adhesive use JKR model [N]
m	Total number of contact points
F_{Totc}^n	Total normal contact force [N]
$F_{t,s}$	Tangential contact force of Hertzian spring [N]
$F_{t,d}$	Tangential contact force of Hertzian dashpot [N]

$F_{t,f}$	Friction force in tangential direction [N]
F_{Totc}^t	Total tangential contact force [N]
F_c^R	Resultant contact force [N]
T_t	Torque from tangential forces [Nm]
R_n^*	Equivalent radius between particles or particle to wall in the normal direction [μm]
Δt^{crit}	Critical time step [μs]
r_{min}	Minimum particle radius [μm]
ρ	Density of particle $\left[\frac{kg}{m^3}\right]$
G	Shear modulus of particle [MPa]
ν	Poisson's ratio [-]
Δt	Time step [μs]
$d_{p,e}$	Distance between the particle and the element [μm]
r	Particle radius [μm]
L	Sliding distance value [mm]
v_R	Resultant velocity [m/s]
p	normal pressure [MPa]
Cof R2	Coefficient of friction interaction among Ln-SS-LHS1 materials for running time with two minutes [-]
Cof R6	Coefficient of friction interaction among Ln-SS-LHS1 materials for running time with six minutes [-]
Cof R15	Coefficient of friction interaction among Ln-SS-LHS1 materials for running time with fifteen minutes [-]
Cof R30	Coefficient of friction interaction among Ln-SS-LHS1 materials for running time with thirty minutes [-]
Dp	Wear curves or displacement [mm]
Dp 2	Wear curves or displacement from the interaction of Ln-SS-LHS1 materials by two minutes running of time [mm]
Dp 6	Wear curves or displacement from the interaction of Ln-SS-LHS1 materials by six minutes running of time [mm]
Dp 15	Wear curves or displacement from the interaction of Ln-SS-LHS1 materials by fifteen minutes running of time [mm]
Dp 30	Wear curves or displacement from the interaction of Ln-SS-LHS1 materials by thirty minutes running of time [mm]
Δm	Changing mass loss [g]
R2 Pin	Pin surface analysis after two minutes running time [min]
R6 Pin	Pin surface analysis after six minutes running time [min]
R5 Pin	Pin surface analysis after fifteen minutes running time [min]
R3 Pin	Pin surface analysis after thirty minutes running time [min]
Ln-SS- LHS1-R2 Pin	Interaction of Ln, SS, and LHS1 with two minutes running time
Ln-SS-LHS1- R6 Pin	Interaction of Ln, SS, and LHS1 with six minutes running time

Ln-SS-LHS1- R15 Pin	Interaction of Ln, SS, and LHS1 with fifteen minutes running time
Ln-SS-LHS1- R30 Pin	Interaction of Ln, SS, and LHS1 with Thirty minutes running time
Dp	Degree of penetration [-]
Ln-SS- LMS1-R2 Pin	Interaction of Ln, SS, and LHS1 with two minutes running time
Ln-SS-LMS1- R6 Pin	Interaction of Ln, SS, and LHS1 with six minutes running time
Ln-SS-LMS1- R15 Pin	Interaction of Ln, SS, and LHS1 with fifteen minutes running time
Ln-SS-LMS1- R30 Pin	Interaction of Ln, SS, and LHS1 with Thirty minutes running time
Cof R2	Coefficient of friction interaction among Ln-SS-LMS1 materials for running time with two minutes [-]
Cof R6	Coefficient of friction interaction among Ln-SS-LMS1 materials for running time with six minutes [-]
Cof R15	Coefficient of friction interaction among Ln-SS-LMS1 materials for running time with fifteen minutes [-]
Cof R30	Coefficient of friction interaction among Ln-SS-LMS1 materials for running time with thirty minutes [-]
Dp 2	Wear curves or displacement from the interaction of Ln-SS-LMS1 materials by two minutes running of time [mm]
Dp 6	Wear curves or displacement from the interaction of Ln-SS-LMS1 materials by six minutes running of time [mm]
Dp 15	Wear curves or displacement from the interaction of Ln-SS-LMS1 materials by fifteen minutes running of time [mm]
Dp 30	Wear curves or displacement from the interaction of Ln-SS-LMS1 materials by thirty minutes running of time [mm]
θ	Angle of repose [°]
h	Pile height [mm]
r	Mean base radius of the heap [mm]
φ_{bottom}	Angle of repose [°]
$\varphi(\mu_0)$	Angle of repose [°]
μ_0	Interparticle static friction coefficient [°]
L	Maximal increase in angle attributable to frictional effects [°]
k	Characterizes the sensitivity of the angle to changes in friction [-]
μ_i	Inflection point indicating the most responsive friction range [-]
φ_0	Base angle of repose in the hypothetical limit of zero friction [°]
R^2	High coefficient of determination [-]
φ	Angle of repose [°]
E	Adhesive surface energy [mJ/m²]
F_y	Vertical force acting on the pin slice [N]
k	Wear coefficient [$\mu m^3/J$]
d	Worn-out material thickness [mm]

1. INTRODUCTION, TASKS OF RESEARCH

This chapter outlines the context and aims of the present investigation.

1.1. Introduction

Friction and wear remain persistent challenges in mechanical engineering, particularly in applications where machinery is exposed to harsh, abrasive environments. Abrasive wear, characterized by the removal of material due to hard particles interacting with component surfaces, poses significant risks to the integrity of machine elements such as bearings, gears, and seals. While terrestrial machinery used in agriculture, mining, and road construction is vulnerable to damage from contaminants like soil and sand, the challenges are even more severe in extra-terrestrial environments.

Lunar regolith, the fine, loose layer covering the Moon's surface, is notorious for its extreme abrasive properties. Unlike Earth's surface materials, lunar regolith particles have not undergone weathering processes due to the absence of an atmosphere. As a result, these particles are highly angular, sharp-edged, and possess reactive surfaces that promote aggressive micro-cutting and surface fatigue. Even minimal contact with moving mechanical parts can lead to significant material removal, accelerated wear, and eventual component failure. For instance, delicate elements such as shaft seals and sliding bearings are especially susceptible to the abrasive effects of lunar dust, which can infiltrate small clearances and compromise the performance of entire systems.

In contrast, Martian regolith exhibits notable differences stemming from Mars' unique environmental conditions. Martian particles are generally coarser and are enriched with iron oxides and silicates, which influence their abrasive behaviour. While Martian dust storms contribute to continuous surface contamination and can cause wear through persistent deposition and impact, the overall abrasive potential is somewhat mitigated by the larger, less reactive particle size compared to lunar regolith. Despite these differences, both lunar and Martian environments underscore the critical need for advanced materials and design strategies that can withstand abrasive conditions. However, the Moon's harsher abrasive characteristics demand a particularly focused evaluation.

The severe wear effects observed during past lunar missions have revealed that the infiltration of regolith into mechanical systems can lead to premature degradation of vital components. During lunar landings and surface operations, regolith-induced damage to seals, joints, and optical assemblies has been documented, resulting in reduced performance and increased maintenance challenges. Given that on-site repairs in extra-terrestrial settings are highly impractical, ensuring the durability and reliability of machinery through innovative design and material selection is paramount.

1.2. Tasks of research

This dissertation focuses primarily on the abrasive wear challenges posed by lunar regolith. By systematically analysing the interaction between lunar abrasive particles and critical machine element materials, the research aims to elucidate the underlying wear mechanisms and reveal the features of damages under lunar regolith. Over this research the final goal is to develop robust mitigation strategies through improved material formulations and optimized component

designs that can enhance the longevity and performance of machinery destined for future lunar missions.

- Analyses of lunar dust abrasion on rotary shaft's stainless-steel material and static seals machined from natural polytetrafluoroethylene (PTFE).
- Coupon-scale laboratory abrasive test on pin-on-disc machine, measuring the abrasive friction and wear on-line beside microscopic analyses of the original and worn surfaces.
- Analysing the selected regolith simulant: particles shape, profile, size distribution
- DEM development to simulate the abrasive wear process by lunar regolith
- Sensitivity analysis of developed DEM model: influence of different parameters (internal friction, surface energy, particle size and shape)
- DEM validation with pin-on-disc results measured on-line

2. LITERATURE REVIEW

2.1   Introduction to tribology: Friction and wear fundamentals

Foundational literature, such as (Bushan, 2001), (Kato & Adachi, 2001), (Ludema, 1996), and (G. Stachowiak & Batchelor, 2005), defines Tribology as " the science and engineering of interacting surfaces in relative motion." It encompasses the study of friction, wear, and lubrication. Originating from the Greek word tribos, meaning "rubbing," tribology has evolved into a multidisciplinary field crucial for mechanical engineering, materials science, and manufacturing. Its importance lies in enhancing the performance, reliability, and longevity of mechanical systems by understanding and managing surface interactions. In mechanical engineering, tribology plays a pivotal role in the design and maintenance of components such as bearings, gears, seals, and other moving parts where frictional forces impact efficiency and wear.

Friction: Friction is the resistance to relative motion between two contacting surfaces. It is a fundamental tribological phenomenon influencing energy consumption, wear rates, and operational stability in mechanical systems. Friction is generally categorized into three types: static friction (resistance before motion starts), kinetic friction (resistance during motion), and rolling friction (resistance in rolling contact). In the context of mechanical systems, dry friction occurring between unlubricated solid surfaces is of particular significance. Understanding the mechanisms and models of dry friction helps in designing efficient and durable mechanical components (G. W. Stachowiak & Batchelor, 2015).

Components of friction:

Adhesion and deformation: The frictional force between two surfaces primarily arises from two mechanisms: adhesion and deformation. Adhesion occurs due to intermolecular forces at the microscopic contact points between surfaces. When two surfaces come into contact, microscopic asperities (surface roughness peaks) form junctions that create adhesive bonds. During relative motion, these bonds must be sheared or broken, contributing to the frictional resistance. The strength of this adhesive component is influenced by factors such as material properties, surface roughness, and environmental conditions.

Deformation component of frictions is associated with the energy dissipated due to elastic or plastic deformation of asperities under load. As surfaces move relative to each other, asperities are deformed, leading to energy dissipation as heat. In dry friction scenarios, this component becomes more pronounced when the contact involves rough or soft materials where plastic deformation is significant.

Friction models for dry contact: Several theoretical models have been developed to describe dry friction behaviour, focusing on the adhesive and deformation components. The most notable ones include (G. W. Stachowiak & Batchelor, 2015):

Amontons-Coulomb law: One of the earliest models, it states that friction is proportional to the normal load and independent of the apparent contact area. Mathematically, it is expressed as:

$$F = \mu\,N \tag{2.1}$$

Where:

F frictional force

μ Coefficient of friction

N Normal load

Although widely used for its simplicity, this model does not account for surface roughness or material properties.

Bowden and Tabor model: This model emphasizes the role of real contact area formed by asperity junctions. It suggests that friction is proportional to the shear strength of the material at the microscopic contact points, providing a more accurate representation of adhesive friction (Wilson, 1998).

$$F = \tau \, A_r \tag{2.2}$$

Where:

τ Shear strength of the contact junctions (material-dependent)

A_r Real area of contact

The real area of contact (A_r) is much smaller than the apparent contact area because surfaces are rough at the microscopic level.

Contact only occurs at asperity peaks. A_r is proportional to the normal load (N) and inversely proportional to the hardness (H) of the softer material:

$$A_r = {}^N\!/_H, \text{ Thus } F = \tau \left({}^N\!/_H\right) \tag{2.3}$$

Where:

H Hardness of the softer material

This shows that friction is proportional to the normal load, aligning with Amontons-Coulomb's law but providing a physical basis by considering the microscopic contact mechanics.

Greenwood-Williamson model: Focusing on surface roughness, this model considers the distribution of asperity heights and their elastic or plastic deformation under load. It provides a statistical approach to contact mechanics, making it more suitable for complex rough surfaces (G. W. Stachowiak & Batchelor, 2015).

Rate and state friction models: These models incorporate the time dependency and history of contact, allowing for the analysis of dynamic frictional behaviour such as stick-slip motion. They are particularly useful for understanding earthquake mechanics and other dynamic systems. Understanding the mechanisms and models of friction is fundamental to the field of tribology.

By analyzing the adhesive and deformation components, engineers can design more efficient and reliable mechanical systems.

Dry friction models, from the classical Amontons-Coulomb law to more advanced approaches like the Greenwood-Williamson model, provide critical insights into the complex interactions at contacting surfaces.

In mechanical engineering, this knowledge is essential for optimizing material selection, surface treatments, and lubrication strategies to minimize wear and energy losses.

Classification of wear mechanisms and wear modes: The categorisation of wear parameters (G. W. Stachowiak & Batchelor, 2015), along with descriptive terminology of the wear mechanisms, is presented in table 2.1.

Table 2.1. Classification of wear parameters (G. W. Stachowiak & Batchelor, 2015).

Class	Parameter				
Friction type	Rolling	Rolling–sliding	Sliding	Fretting	Impact
Contact shape	Sphere/ sphere	Cylinder/ cylinder	Flat/ flat	Sphere/ flat	Cylinder/ flat	Punch/ Flat
Contact pressure level	Elastic		Elasto-plastic		Plastic	
Sliding speed or loading speed	Low		Medium		High	
Flash temperature	Low		Medium		High	
Mating contact material	Same	Harder	Softer	Compatible	Incompatible
Environment	Vacuum		Gas		Liquid	Slurry
Contact cycle	Low (single)		Medium		High	
Contact distance	Short		Medium		Long	
Phase of wear	Solid	Liquid	Gas	Atom	Ion
Structure of wear particle	Original		Mechanically mixed		Tribochemically formed	
Freedom of wear particle	Free		Trapped		Embedded	Agglomerated
Unit size of wear	mm scale		μm scale		nm scale	
Elemental physics and chemistry in wear	Physical adsorption, chemical adsorption, tribochemical activation and tribofilm formation, oxidation and delamination, oxidation and dissolution, oxidation and gas formation, phase transition, recrystallization, crack nucleation and propagation, adhesive transfer and retransfer				
Elemental system dynamics related to wear	Vertical vibration	Horizontal vibration	Self-excited vibration	Harmonic vibration	Stick-slip motion
Dominant wear process	Fracture (ductile or brittle)	Plastic flow	Melt flow	Dissolution	Oxidation	Evaporation
Wear mode	Abrasive	Adhesive	Flow	Fatigue	Corrosive	Melt	Diffusive
Wear type	Mechanical		Chemical		Thermal	

Wear: Wear is the progressive material loss from solid surfaces due to mechanical action, such as friction or contact with another surface. It significantly impacts the performance, efficiency, and longevity of mechanical components. In tribology, understanding wear mechanisms and predicting wear rates are crucial for designing reliable systems and reducing maintenance costs. Frictional interactions give rise to several wear mechanisms, each governed by distinct physical and chemical processes.

Main wear mechanisms: Among many basic tribology literatures, handbooks (G. W. Stachowiak & Batchelor, 2015), (Kato & Adachi, 2001), (Ludema, 1996), (Bushan, 2001) and (G. Stachowiak & Batchelor, 2005) works give a detailed overview. Based on these established references, the primary wear mechanisms are defined as:

Adhesive wear: It occurs when two surfaces in relative motion form atomic or molecular bonds at asperity contact points. These micro-junctions break during sliding, leading to material transfer or detachment. It commonly occurs in metallic contacts with high adhesion forces. Archard's wear law describes adhesive wear:

$$V = KW\,L/H \tag{2.4}$$

Where:

> V wear volume
> K Dimensionless wear coefficient (material-dependent)
> W Normal load
> L Sliding distance

Abrasive wear: It occurs when a harder surface or particle plows into a softer surface, removing material by cutting or scratching. It is categorized into: two-body abrasion, when direct contact between two surfaces having hard asperities on one surface cut into the other, and three-body abrasion that involves loose particles between two surfaces, rolling or sliding and causing wear. Hutchings' Model for Abrasive Wear:

$$V = \alpha W\, L/H \tag{2.5}$$

Where:

> α Abrasive wear coefficient influenced by particle shape and hardness ratio

This model emphasizes the role of hardness and abrasive severity. The abrasion is further discussed in 2.2. As it is a core tribological phenomenon at my research program.

Fatigue wear: it results from cyclic loading and unloading at contact points, leading to crack initiation and propagation. Over time, these cracks join, causing material detachment as wear particles. It commonly occurs in rolling or sliding contacts, such as bearings and gears. Wear rate correlates with contact stress and the number of cycles (Coffin-Manson model).

$$V \propto \sigma^m N \tag{2.6}$$

Where:

> σ Contact stress
> m Material-dependent exponent
> N Number of loading cycles

Originally developed to describe low-cycle fatigue in metals due to plastic strain. It has been adapted to analyse fatigue wear by relating the wear volume to cyclic stress and loading cycles.

Fretting wear: Fretting wear occurs at contact surfaces under small amplitude oscillatory motion, typically in bolted joints or spline couplings. It combines adhesion, micro-abrasion, and oxidation. This wear mechanism often leads to surface damage, fatigue cracks, and corrosion. Coffin-Manson model can also be used, as wear is primarily due to repeated loading and unloading, leading to crack initiation and propagation, such as in fretting wear, rolling contact fatigue, and fatigue in sliding contacts.

Tribo-chemical wear: Tribo-chemical wear occurs when chemical reactions at the contact interface are accelerated by frictional heat and mechanical action. These reactions lead to the formation or removal of surface layers, influencing wear behaviour. This mechanism is common in high-temperature applications, corrosive environments, and in the presence of reactive lubricants or contaminants.

2.2   Abrasive wear

Importance of abrasive wear in mechanical engineering: Abrasive wear is particularly significant in mechanical engineering due to its prevalence in industrial applications. It

frequently occurs in cutting tools, conveyor systems, mining equipment, and hydraulic machinery, where hard particles or contaminants are present. Abrasive wear can lead to rapid material degradation, impacting performance and operational efficiency. In harsh environments, such as in mining, construction, and agriculture, abrasive wear is the primary cause of component failure. Consequently, engineers prioritize abrasion resistance in material selection and design. Strategies to mitigate abrasive wear include:

- Material Selection: Using harder materials, surface hardening techniques, or wear-resistant coatings.
- Design Modifications: Optimizing surface geometry to minimize abrasive interactions.
- Lubrication and Sealing: Preventing the ingress of abrasive particles into contact zones.

In conclusion, understanding abrasive wear is crucial for improving the durability and reliability of mechanical systems. Accurate prediction models, such as Hutchings' model, and advanced materials engineering are essential tools for managing abrasive wear in practical applications.

Mechanisms of abrasive wear: The surface of a polymer box degrades swiftly upon contact with a metal box, as the softer polymer material exhibits a lesser hardness compared to the metal surface. The grooves are present in abrasive wear tracks formed at the interface of two analogous metals undergoing sliding friction. The production of wear particles or debris during this process affects subsequent wear on the material's surface. The creation of wear particles is attributed to work hardening, phase change, or the contact with a third body at the interface. Various mechanisms of abrasive wear have been suggested to better understand the process of material removal: cutting, fracture, fatigue and grain formation:

Abrasive wear due to cutting: The cut produced by the sharp grit or asperity leads to abrasive on the surface of the softer substance, resulting in wear.
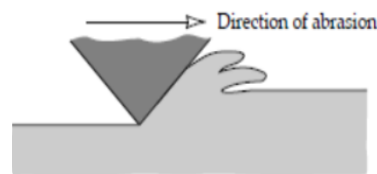

Fig.2.1. Abrasive wear by cutting (Lin Shenxing et al., 2005).

Abrasive wear due to fracture: The wear due to the formation of brittle fracture initiated by a subsurface crack.
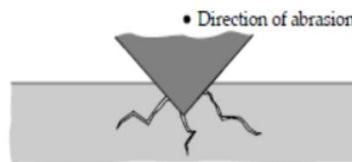

Fig.2.2. Abrasive wear by fracture (Lin Shenxing et al., 2005)**.**

Abrasive wear by fatigue: The grits on the surface, which induce abrasive wear, result in recurrent strain on the metal surface, leading to fatigue.
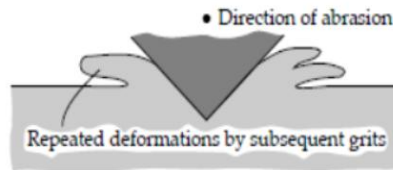
Fig.2.3. Abrasive wear by fatigue (Lin Shenxing et al., 2005).

Abrasive wear by grain formation: Pulled-out or shattered grains constitute the wear debris resulting from the grain pull-out process.
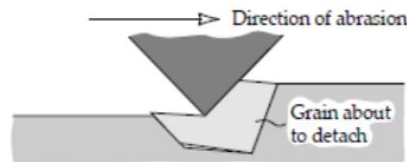

Fig.2.4. Abrasive wear by grain formation (Lin Shenxing et al., 2005).

Abrasive wear mechanism modes: Abrasive wear can be categorised into two groups two-body abrasive wear and three-body abrasive wear based on the migration of wear debris generated outside the worn surface during the abrasive process.

Two-body abrasive wear: In this phase, wear results from the abrasion of surface materials by sharp grits or hard particles.
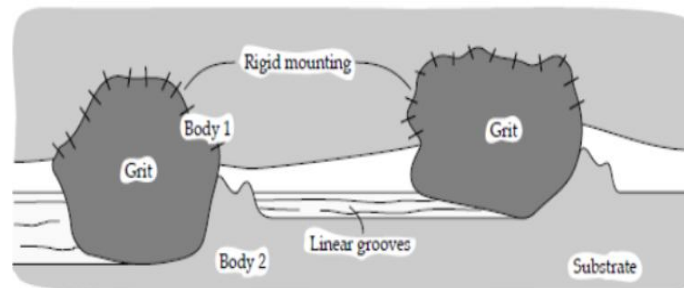
Fig.2.5. Abrasive wear by two-body abrasive wear (Lin Shenxing et al., 2005).

Three-body abrasive wear: The grits freely roll and slide at the interface, with surface hardness being a crucial characteristic that influences wear.
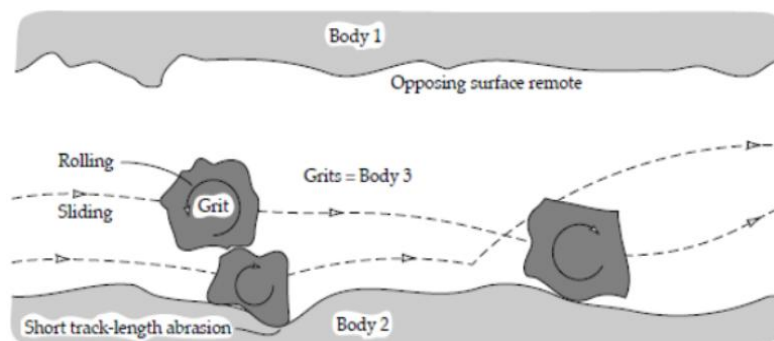

Fig.2.6. Abrasive wear by three-body abrasive wear (Lin Shenxing et al., 2005).

Two influential models for predicting abrasive wear are the Rabinowicz model and the Hutchings model. Although they both address abrasive wear mechanisms, they differ in their approaches, assumptions, and applications.

Rabinowicz Model: it is one of the earliest theoretical approaches to abrasive wear. It is based on the concept that abrasive particles or asperities cut grooves into the softer material. Rabinowicz emphasized the geometrical aspects of abrasive action and the material's mechanical properties. It is featured as: abrasive particles or asperities are rigid and harder than the worn material, material removal occurs through micro-cutting, similar to machining processes, particles maintain a fixed attack angle while moving over the surface (G. W. Stachowiak & Batchelor, 2015).

$$V = k W \,^{L}/_{H} \qquad (2.7)$$

Where:

k Wear coefficient, dependent on abrasive geometry and contact conditions

The abrasive wear coefficient "k" depends on the abrasive shape, attack angle, and cutting efficiency. It primarily applies to two-body abrasion, where rigid particles or asperities slide over the worn surface.

Hutchings Model was introduced in 2.1, but it is worth to mention that extends the understanding of abrasive wear by incorporating detailed analysis of abrasive particle dynamics and deformation mechanisms. It accounts for both cutting and plowing actions of abrasives, offering a more comprehensive description of the wear process. It is featured as: abrasive particles can deform elastically or plastically, depending on contact stresses, wear results from a combination of cutting (material removal) and plowing (plastic deformation), the model considers the role of abrasive particle shape, hardness ratio, and attack angle (G. W. Stachowiak & Batchelor, 2015). Comparison of the models (Table 2.2) based on the mentioned literatures in 2.1 and 2.2.

Table 2.2. Comparison of the generic abrasive models.

Aspect	Rabinowicz model	Hutchings model
Mechanism focus	Primarily micro-cutting action	Cutting and plowing mechanisms
Abrasive dynamics	Assumes rigid abrasives with fixed attack angle	Considers elastic/plastic deformation of abrasives
Wear coefficient	Empirical, depends on geometry and efficiency	More detailed, includes shape, hardness ratio, and angle
Wear coefficient	Empirical, depends on geometry and efficiency	More detailed, includes shape, hardness ratio, and angle
Complexity and accuracy	Simpler but less accurate for complex contacts	More comprehensive and accurate
Material considerations	Focuses on hardness as resistance to wear	Considers hardness and plastic deformation behavior

Rabinowicz model is suitable for simple two-body abrasive wear scenarios where rigid abrasives cut the softer surface. It is often used for initial wear estimations or when detailed particle dynamics are not needed. Hutchings Model is more versatile, applicable to complex wear situations involving both cutting and plowing. It is preferred in cases with varying abrasive particle shapes, hardness ratios, and dynamic contact conditions.

While both models are fundamental to understanding abrasive wear, the Rabinowicz model provides a simpler, geometry-focused approach, whereas the Hutchings model offers a more detailed and accurate representation by considering particle deformation and interaction dynamics. The choice of model depends on the complexity of the wear environment and the desired accuracy of the wear predictions.

Often in tribology, both model is called "modified" Archard model due to the similarity, but emphasizing the role of "k" factor differences. Later, when the DEM models will be introduced, the modified Archard's model will come back.

Degree of penetration (Dp) during abrasion: Wear micro-mechanism characterization with D_p as it was introduced by.(Hokkirigawa & Kato, 1988). D_p of a wear groove, not only serves as a tool to identify the micro-abrasion processes from the wear track geometry but also gives an indication about the wear severity. Height characteristics are typically defined by parameters such roughness average, root mean square roughness, mean maximum peak-to-valley height, ten-point height, among others. Certain height parameters are delineated in Table 2.3. The mean Dp of all the grooves that are present on the worn surface is calculated with ten point height and mean spacing at mean line, corresponding to the groove depth and the groove width of a single scratch.

$$D_p = \frac{R_z}{\frac{R_{sm}}{2}} \tag{2.8}$$
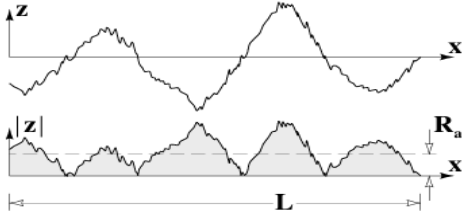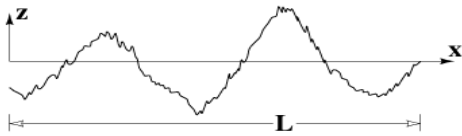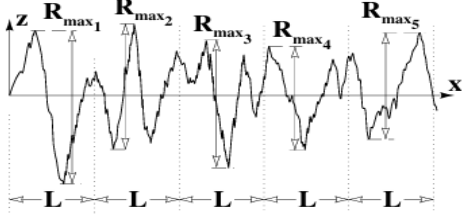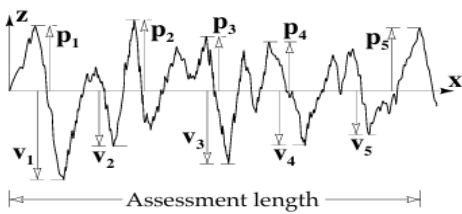
Where:

D_p Degree of penetration
R_z Ten point height [µm]
R_{sm} Mean spacing at mean line [µm]

Cone-fit analysis (CFA): The method known as CFA has developed from the traditional abrasion model introduced by Rabinowicz, in which the asperities of abrasive surfaces or particles are depicted as cones. The efficacy of an abrasive particle to abrade is significantly influenced by its orientation relative to the worn surface, or the angle of attack. The abrasiveness of a particle is contingent upon the extent of its penetration and abrasion of the wearing surface. According to this concept, highly abrasive particles may be depicted by cones with a steep angle of attack. Fig.2.7 schematically depicts the classical abrasion model, wherein a singular cone-shaped asperity, positioned at an angle of attack, is pressed against and abrades a flat surface.

Table 2.3. Commonly used height parameters (Lin Shenxing et al., 2005).

Roughness average (CLA or $\mathbf{R_a}$)	$$R_a = \frac{1}{L}\int_0^L |z|\, dx$$	
Root mean square roughness (RMS or $\mathbf{R_q}$)	$$R_q = \sqrt{\frac{1}{L}\int_0^L z^2\, dx}$$	
Maximum peak-to-valley height ($\mathbf{R_t}$)	Largest single peak-to-valley height in five adjoining sample lengths $$R_t = \frac{1}{5}\sum_{i=1}^{5} R_{max_i}$$	
Ten-point height ($\mathbf{R_z}$)	Average separation of the five highest peaks and the five lowest valleys within the sampling length $$R_z = \frac{p_1 + ... + p_5 + v_1 + ... + v_5}{5}$$	

Where:
  L sampling length [m]
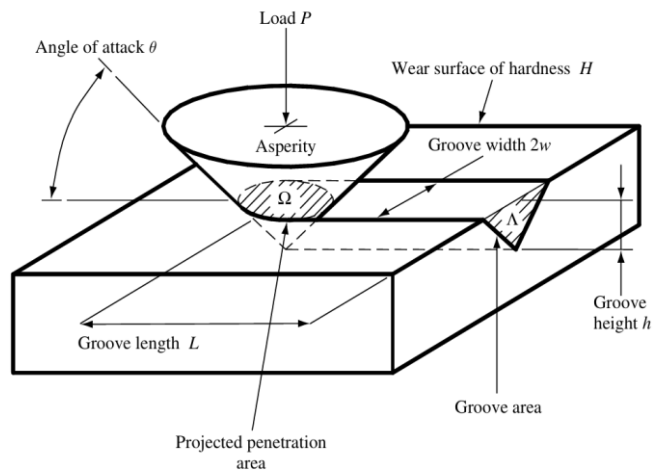 z height of the profile along 'x' [m]

Fig.2.7. Schematic representation of the projected penetration area $\mathbf{\Omega}$ and groove area Λ (G. W. Stachowiak & Batchelor, 2015).

11

Analytical models of abrasive wear: In a fundamental and ancient model of abrasive wear, a firmly secured grit is represented by a cone that indents a surface while being traversed along it, as image in Fig.2.8. This model assumes that all material displaced by the cone is lost as wear debris.
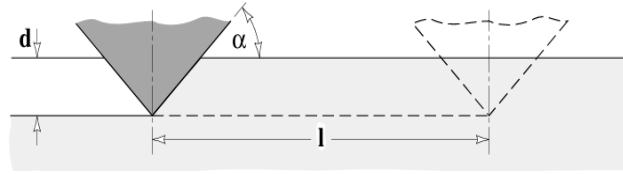

Fig.2.8. Image of abrasive wear caused by an individual particle (Lin Shenxing et al., 2005).

In this abrasive wear model, the load on the particle is determined by the product of the projected area of the indentation created by the cone and the material's yield stress during indentation (Lin Shenxing et al., 2005):

$$W_g = 0.5\pi(d\cot\alpha)^2\sigma_y \tag{2.9}$$

Where:

W_g Individual load on the particle
d Depth of indentation
α Slope angle of the cone
σ_y Materials yield stress under indentation

The estimated volume of the material excised by the cone is the product of the cross-sectional area of the indentation, 'd²cotα', and the distance traversed, 'l':

$$V_g = ld^2\cot\alpha \tag{2.10}$$

Where:

V_g Volume of material removed by the cone

l Distance travelled by the cone

Substituting "d" from equation 2.9 into equation 2.10 yields an expression for the worn volume of material as a function of the stress on the particle, the particle's morphology, and the sliding distance:

$$V_g = \frac{2l\tan\alpha}{\pi H} \times W_g \tag{2.11}$$

The total wear is the aggregate of the individual volumes of material worn by particle.

$$V_{tot} = \sum V_g = \frac{2l\tan\alpha}{\pi H} \times \sum W_g \tag{2.12}$$

$$V_{tot} = \frac{2l\tan\alpha}{\pi H} \times W_{tot} \tag{2.13}$$

Where:

V_{tot} Total wear

W_{tot} Total load

Abrasiveness of particles: A particle or grit is typically classified as abrasive when it may induce rapid or effective abrasive wear. The abrasiveness of a particle is contingent upon its hardness, dimensions, and morphology. (G. W. Stachowiak & Batchelor, 2015).

- **Effect of particle hardness:** The material's hardness must be below 0.8 of the particle hardness for fast abrasion to transpire. A finite degree of abrasive wear and surface damage persists unless the yield stress of the material surpasses that of the abrasive particle. Extremely gradual abrasive wear continues until the hardness of the abrasive and the worn material become equivalent. Certain materials with soft phases or insufficient strain hardening may endure wear until their hardness reaches 1.2 to 1.4 times that of the abrasive.

- **Influence of particle dimensions:** The dimensions and geometry of a grit are additional factors influencing the abrasivity of a particle. A primary constraint on the abrasiveness of particles with exceedingly small particle dimension is the surface energy of the substance being abraded. As particle dimension diminishes, the fraction of frictional energy utilised for the formation of a new surface escalates.

- **Influence of particle morphology:** The geometry of the particle is crucial in determining the deviation of the particle's morphology from that of an ideal sphere, as well as the quantity of edges or corners present on the particle.

Abrasive wear resistance of materials: The foundation of abrasive wear resistance in materials is hardness, and it is well acknowledged that harder materials exhibit slower abrasive wear rates compared to softer materials.

- **Abrasive wear resistance of steels:** The choice of steel is contingent upon the hardness of the abrasive.

- **Abrasive wear resistance of polymers and rubbers:** Polymers can exhibit an unexpectedly high level of resistance to abrasive wear when compared to a metal of equivalent hardness. The abrasive wear characteristics of plastics can be significantly influenced by additions like fillers and plasticisers.

Impact of temperature on abrasive wear: The impact of temperature on abrasive wear can be categorised into the impact of ambient temperature and the influence of temperature increases caused by the plastic deformation of worn material in contact with abrasives.

Effect of humidity on abrasive wear: Moisture significantly affects abrasive wear rates. Abrasive wear rates typically escalate with increased atmospheric moisture content; nevertheless, there are instances where an opposing impact is observed.

Control of abrasive wear: The fundamental approach to controlling or mitigating abrasive wear involves increasing the hardness of the worn surface to a minimum of 0.8 times the hardness of the abrasive grit. No other type of deterioration permits such a straightforward justification for its mitigation.

2.3 Abrasive problems of sealing solution

Many books and engineering literatures as (Blau, 2016), (Neale, 1995), (B. Tan & Stephens, 2019), (Y. Li et al., 2024), introduces sealing solutions for rotary and static cases. Based on those I briefly sum the followings:

The primary subject of this work is the study of friction in sliding seals, as indicated by the subtitle. Initially, provide a concise explanation of the function of sliding seals. Secondly, it

presented the categorisation of sliding seals. Thirdly, friction is typically not a key concern for static seals, although it is significant for dynamic seals. Fourthly Seals should ideally possess low friction and minimal wear while demonstrating effective sealing capabilities. Fifthly, the selection of appropriate materials for seal applications, such as low-friction polymers like polytetrafluoroethylene (PTFE), has proven effective in lip and face seals; however, hard ceramics, including silicon carbide and high-alumina ceramics, have also been utilised in applications such as water pump seals. Finally, a table has been developed that enumerates preferred seal materials along with their limits, including maximum pressure, maximum temperature, material composition, and usual applications (Blau, 2016).

The main focus of this subtitle in the book is the choosing of seals. Initially, provide a concise overview of the fundamental types of seals and accurately characterise each one. The enumerates the features of dynamic seals, including contact seals, clearance seals, sealing interface, leakage, friction, lifespan, and dependability. Thirdly, provide a detailed explanation of the types of dynamic and static seals. Fourthly, provide a detailed explanation of the use of dynamic contact seals in the six dynamic sealing scenarios: liquid to liquid, liquid to gas, liquid to vacuum, gas to gas, gas to vacuum, and vacuum to vacuum, accompanied by a two-dimensional illustration. A fifth developed checklist for seal selection, encompassing parameters such as temperature, speed, pressure, size, leakage, fluid compatibility, abrasion resistance, and vibration. Provide a concise explanation of operating seals against dirt and dust conditions, including the source, nature, and impact of pollutants. Seventh iteration of the sealing mechanism to mitigate the impact of dirt and dust. Comprehensive elucidations about lip seals, encompassing design variations, operational conditions, and a tabulated inventory of lip seal materials (rubbers), seals for reciprocating shafts, packing types, materials, extrusion clearance, metal component design, and friction considerations (Neale, 1995).

This research focuses on the viscoelastic behaviour of polytetrafluoroethylene (PTFE) based materials. PTFE-based materials are extensively utilised in tribology, especially in sealing applications, due to their exceptional self-lubricating characteristics. PTFE seals are extensively utilised in conventional markets such as pneumatics and hydraulics, as well as in aerospace, energy, oil and gas, among others. PTFE materials are appropriate for deployment in extreme environments with temperatures spanning from cryogenic conditions (about $-150°C$) to $300°C$, alongside highly corrosive substances. Numerous applications utilise PTFE-based seals. It is employed as an O-ring for static seals. For dynamic and radial sealing. PTFE-based material is extensively employed in aerospace and aircraft sealing applications, including rotary seals, static seals, airframe seals, and hydraulic rod seals. PTFE has exceptional friction and sliding qualities, along with the absence of stick-slip, resulting in great sealing efficiency. The storage modulus, loss modulus, and tanδ are measured and analysed in the frequency domain using a dynamic mechanical analyser. The relaxation modulus and creep compliance are measured and analysed in the time domain. The compositions of the materials are analysed using an Energy Dispersive X-ray Spectrometer for composite assessment. The experimental data is modelled with optimal fit curves with the Prony series and compared to the empirical data (B. Tan & Stephens, 2019).

The emphasis was on wear morphology, chemical alterations, and the mechanisms of wear failure under various dry friction situations. The tunnel boring machine (TBM) is a sophisticated, large-scale engineering apparatus that is intricately connected with various professional fields, including materials science, geology, mechanical engineering, civil

engineering, computer science, and information systems. The primary elastomer seal of the main drive functions as a protective barrier for the TBM core main drive. The elastomer seal operates under severe conditions and effectively inhibits the ingress of sand and gravel into the precise machinery (Y. Li et al., 2024). The analysis focused on the alterations in intermolecular interactions and macroscopic mechanical properties influenced by temperature during the friction process, due to the TBM main drive seal's inadequate oil lubrication. The high-speed ring-block friction and wear test investigated the intrinsic relationship between friction heat and the friction coefficient during dry friction across various working conditions, elucidating the wear morphology, chemical alterations, and failure mechanisms under differing dry friction scenarios. As the temperature rises, polyurethane elastomer sealing materials will experience three phases: viscous flow softening; secondary cross linking at elevated temperatures; and complete disintegration and carbonisation. The augmentation of rotation speed and load will improve the dry friction running-in effect between the polyurethane elastomer and the metal counterpart, resulting in more stable steady-state friction and a reduced friction coefficient. The phenomena of sudden temperature rise, at a specific rate, serves as a critical criterion for monitoring and managing the wear and failure characteristics of elastomer sealing materials.

Basic seal types and their characteristics:

- Dynamic seal: Sealing occur between surfaces in sliding contact or in close proximity.
- Static seal: Sealing transpires between stationary surfaces that exhibit no relative motion.
- Pseudo-static seal: This seal allows for limited relative movement at the sealing interfaces, exemplified by swivel couplings for pipes and flexible diaphragms;
- Exclusion seal: A mechanism intended to restrict the entry of contaminants, such as dirt, into a system, often used in conjunction with a dynamic seal.

Categories of dynamic and static sealing: seals are categorised into two types: contact and clearance (Neale, 1995). Various types of seals are depicted in fig 2.9 below.
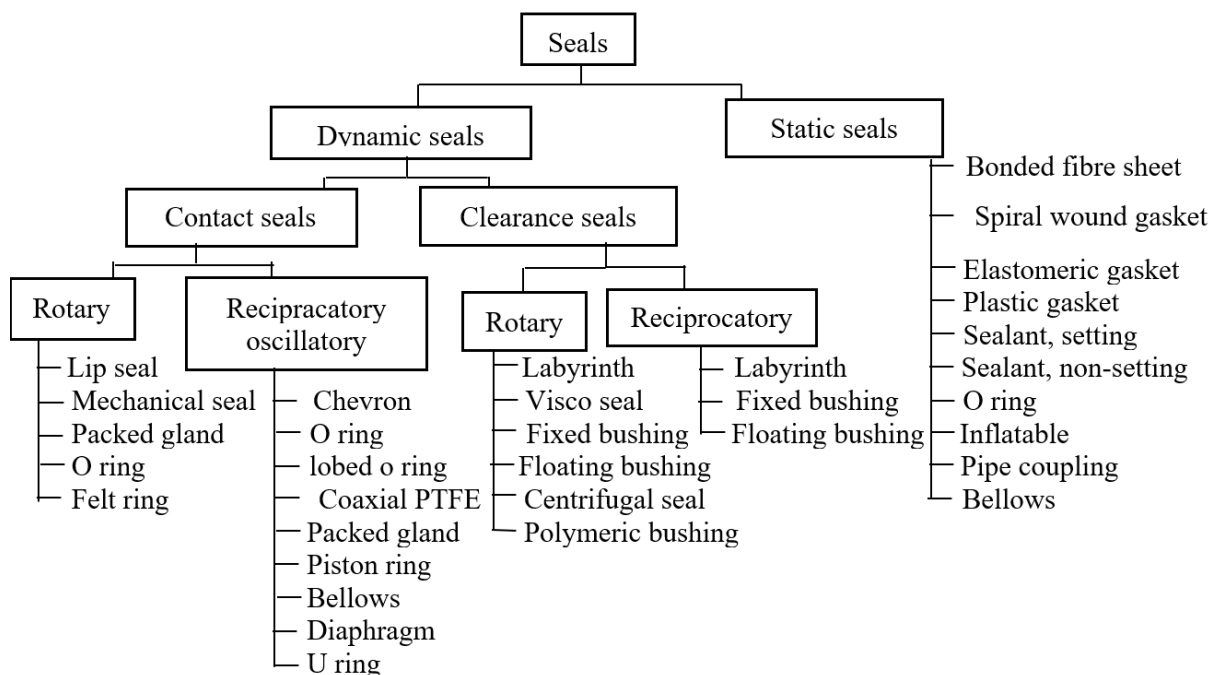

Fig.2.9. Several types of seals.

15

The dissertation concentrates on rotary lip seals and packing gland seals from the aforementioned list of seals. Fig.2.10 (a) and (b) illustrate the rotary lip seal and packed gland.
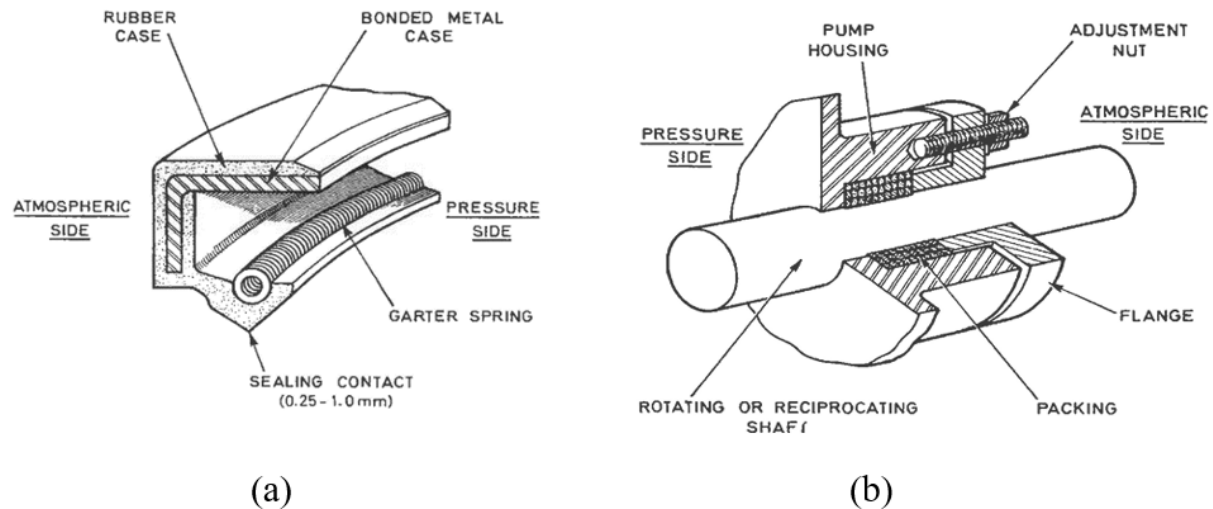

Fig.2.10. Illustrate of: (a) Rotary lip seal and (b) packing gland (Neale, 1995).

Sealing dirt and grit: Utilisation of various sealing lip types for rotating shafts (Neale, 1995)., including: a) single seals suitable for standard workshop or roadway conditions, b) auxiliary sealing lips that offer marginally enhanced performance over individual seals, though not warranting the extra cost, and c) double seals designed for demanding environments, short of immersion in saturated muck. Fig. 2.11 shows several sealing lip for rotating shafts.

Fig.2.11. Shows several sealing: a) single seal, b) auxiliary sealing lip ,and c) double seal (Neale, 1995).

The irregular wear distribution indicates eccentricity or lateral loading. 'O' ring rolling results in variations in the shape and dimensions of the segment.

Table 2.4. Type and causes of failure (Neale, 1995).

Type	Usual symptom	Cause
Abrasive wear	Flat on 'O' ring. Circumferential groove on lip seal. Sharp sealing edge on lip seal.	Pressure too high or abrasive mating surface

Packing gland seals: Packed glands are mostly utilised for sealing valve stems, rotary pump shafts, and reciprocating pump plungers (Neale, 1995)**.**

16

Table 2.5. Materials for use in packed glands (Neale, 1995).

Material	Maximum operating temperature ℃	Special properties	Typical application
Expanded graphite foil	550℃ up to 2500℃ in non-oxidising environments	Low friction, self-lubrication, low compression set and contains no volatile constituents. Available as rings	Valve stems
Graphite/yarn filament	550℃	Available as cross plaited square section lengths. Resistant to extrusion	Valve stems
Aramid (Kevlar)	250℃	Tough and abrasion resistant	Valve stems and pumps
PTFE, filament	250℃	Low friction and good chemical resistance	Valve stems. Pumps at surface speed <10 m/s
Hybrid graphite	250℃	Particularly suitable for high speed rotary shaft. Close brush clearances needed to reduce risk of extension. Good resistance to abrasives.	Pumps shafts for speeds of the order of 25 m/s
Ramie	120℃	Good water resistance	Rotary and reciprocating water pumps

The selection criteria of seals are enumerated below, with explanations (Neale, 1995):

- **Temperature:** Seals may exhibit significant temperature constraints, contingent upon the material used. At reduced temperatures, some fluoro-elastomers may exhibit diminished elasticity and may provide inferior sealing performance under elevated pressure.

Table 2.6. Materials with temperature range (Neale, 1995).

seals materials	Natural rubber	Nitrile rubber	Fluorocarbon rubber	Perfluorocarbon	PTFE, plastic
Temperature (℃)	-40 to +130	-40 to +130	-40 to +200	-10 to +300	-10 to +280

- **Speed**

17

- **Pressure**

- **Size**

- **Leakage**

- **Fluid compatibility:** check all materials which may be exposed to the fluid, especially rubbers.

- **Abrasion resistance:** While harder sliding contact materials are generally superior, it is advisable to avoid the presence of abrasives near the seal whenever feasible, such as by employing a clean fluid for flushing. Polyurethane and natural rubber are notably abrasion-resistant polymers. In applications requiring low friction, filled PTFE may be considered.

- **Vibration:** vibration should be minimised, but rubber seals are likely to function better than hard seals.

- **Sealing against dirt and dust:** The reliability of equipment in dirty and dusty circumstances is predominantly contingent upon the quantity of abrasive material present. Natural soils comprise abrasive elements in proportions ranging from 98% to 20% by weight.

Table 2.7. The source, nature and effect of contaminants (Neale, 1995).

Source	Nature of contaminant	Operating conditions, effect on reliability and basic requirements		
		Wet (more than 15% by weight of water)	Dry	Wet and dry
Contact with soils (high silicon)	Sharp faceted grains predominantly silica (Sio2) 98% by weight occurs frequently	Severe, highly abrasive. Considerable loss of reliability unless extensive sealing provided	Some loss of reliability. Machinery ingesting air requires efficient air cleaning	Severest, maximum abrasive effect. Very good air cleaning and sealing required
(Low silicon)	Predominantly grains of Calcium (CaO). Silica less than 25% by weight.	Clogging rather than abrasive. Some loss of reliability. Sealing required	Little loss of reliability. Good air cleaners and sealing required	Poor conditions. Good air cleaning and sealing required
Airborne dust	Any finely divided material in the dry state picked up in air currents	–	Reduction in reliability dependent on dust concentration. Very large air cleaners required for highest concentrations	–

Design of sealing systems to mitigate the impact of dirt and dust (Neale, 1995):

- Minimise the exposure of rotating or sliding components to adverse circumstances.
- Ensure localised clean environments for bearings and sealing configurations.
- Ensure sufficient space in the sealing mechanism for oil lubrication.
- Avoid employing grease lubrication for bearings unless the design for oil lubrication is deemed economically unfeasible.
- Ensure sufficient provisions for the replenishing of lubricant; readily accessible.
- Safeguard lubricating nipples in situ to prevent breakage caused by stones and soil.
- Facilitate effective methods for verifying the quantity of lubricant within the housing.
- Abrasive material is likely to infiltrate the ram system, posing a significant threat to precise mechanisms.
- The configuration of components must be designed for casting or for usage with machined surfaces.
- Position the air cleaner intakes to prevent the creation of localised dust clouds caused by the movement of the mechanism.

2.3.1 Some relevant research results published about seals in abrasive load

Abrasive wear is a prevalent wear process that diminishes the sealing efficacy and service life of rubber seals. Abrasive wear is a primary failure mechanism that is challenging to prevent in sealing systems. This research enhances the understanding of rubber degradation and wear mechanisms related to abrasive sizes, aiding in the reduction of sealant wear and the extension of their service life (M. X. Shen et al., 2016).

In extended sliding contacts, dynamic seals fail mostly owing to abrasion and compression set, which are the most common failures. The consequence of deteriorated seals is the formation of holes that lead to leakage. To avert such a failure, the seal must be replaced promptly; nevertheless, hasty replacement is inadvisable as it disrupts machinery function, resulting ill financial losses. Therefore, more appropriate wear testing methodologies are required to forecast the longevity of seals. To simulate the actual operational conditions of dynamic seals, numerous experimental testing methodologies established (Farfán-Cabrera et al., 2016).

Dynamic seals, including reciprocating and rotary seals, are prone to failure due to wear caused by sliding contact. Typically, dynamic seals are evaluated using intricate test benches to assess their frictional behaviour, wear resistance, lubrication, and sealing efficacy under realistic conditions. However, the extended duration of these tests restricts the exploration of a broad spectrum of parameters, including materials, temperature, contact pressure, design, and roughness. Consequently, tribological testers represent a viable method to simulate the operational conditions of seals through accelerated testing. The degradation of dynamic seals may result from two-body abrasion and/or three-body abrasion. The micro scale abrasion test may serve as an expedited wear assessment to characterise and choose sealing elastomers before conducting intricate and time-intensive evaluations of dynamic seals under more realistic conditions (Farfán-Cabrera et al., 2017).

Particles can penetrate sealing interfaces, as these seals expose a significant portion of the surface to an abrasive environment, often resulting in quick seal failure. Consequently, seals employed in such operational settings often had a limited lifespan. The tribological test findings indicate that, under conditions of non-uniform abrasive particle size, wear scars attributable to

large-grained particles are distinctly observable. The level of seal damage caused by large particles exacerbated, whilst that caused by smaller particles diminished (Qin et al., 2019).

During operation, hydraulic seals undergo constant wear, which not only restricts their service life but also modifies the geometry of the sealing edge. Thus, this wear-dependent geometric variation results in a progressive alteration of the friction and leakage characteristics of the hydraulic seal during its operational lifespan. The Archard model, established in 1953, is a commonly utilised method for calculating wear. The model was first developed for adhesive wear, however it is frequently employed for abrasive wear as well. The proposed model can be utilised to simulate the variation in hydraulic seal leakage as wear increases during the operational lifespan of any hydraulic component (Angerhausen et al., 2019).

The wear of a seal ring and the corresponding increase in contact breadth significantly affect the temperature distribution within the seal ring. A significant temperature gradient within the seal ring volume identified. Initially, finite element models that integrate thermal and mechanical load steps built based on these scientific discoveries. An in-depth understanding of the contact temperature distribution aids in selecting a suitable elastomeric material (Frölich et al., 2014). The development of oil carbon resulting from elevated contact temperatures could therefore be prevented. The impact of wear on friction torque could also be examined. Design optimisations, such as minimising friction torque, could be performed using the parametric model setup.
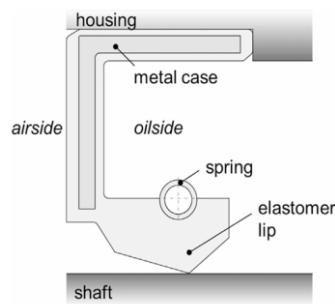

Fig.2.12. Schematic of radial shaft seal ring components (Frölich et al., 2014).

Among all mechanisms contributing to seal degradation, wear caused by abrasive particles from the surrounding drilling fluid (the "mud") is regarded as the predominant mode in most instances. Consequently, comprehending the seal abrasive wear process is essential for enhancing seal durability. Several pivotal research have enhanced the comprehension of seal failure due to abrasive wear. In accordance with the established optimisation criteria, a novel seal with a distinct contact pressure profile was engineered and subsequently evaluated on a rotary seal tester against the standard o-ring design. Testing data demonstrated that the proposed design significantly prolonged the service life of the sealing system. The enhancement in seal performance was validated by the measurement of reduced frictional torque, surface temperature, and material degradation. The surface wear scars demonstrated that the proposed design was superior in preventing the entry of abrasive particles compared to the o-ring seal (Sui & Anderle, 2011).

The rubber sealing pairs are highly susceptible to hard particles, which can readily compromise the lubricating fluid film between the seals, hence hastening their excessive wear. These particles mostly originate from external abrasives, including sand particles, airborne dust, and

detritus, in addition to mechanical internal exfoliation during operation and debris generated by friction. The material qualities, dimensions, and morphologies of the abrasives significantly affect the tribological characteristics of the sealing pairs. Abrasive concentration is a crucial parameter for examining the tribological characteristics of tribo-pairs. Reduced coefficients of friction are primarily influenced by the three-body abrasive present in conditions of low particle concentration (M. xue Shen et al., 2020).

Recent study indicates that in extreme conditions, sealing materials may experience atypical wear, leading to seal failure and negatively affecting their longevity. Recent studies demonstrate that the friction and wear characteristics of rubber materials are affected by various factors, including the physicochemical properties of the material, environmental conditions (such as temperature and humidity), the attributes of the counterpart materials in friction pairs, and operational conditions (such as speed and load). In light of the reported phenomena of heightened oxidation at elevated velocities, it is advisable to advance anti-oxidation coating technology and, considering the attributes of abrasive and adhesive wear, investigate treatment procedures to enhance surface wear resistance (D. Tan et al., 2025). These comprehensive research will enhance the design and utilisation of seals, hence improving their performance and reliability in adverse conditions.

A solid expandable tubular (SET) technology system would be necessarily affected by fluid and string vibrations in downhole conditions, resulting in continuous reciprocating sliding between the rubbers and casing (Fig.2.13a). The constant sliding resulted in significant and rapid degradation of the rubber elastomer, as depicted in fig. 2.13c, d. Upon the occurrence of a sealing failure between the rubber elastomer and N80, substantial leakage may ensue, hence markedly elevating safety production risks. The wear issue of rubber is presently regarded as the primary cause of sealing failure. Under dry conditions, the wear process of the rubber elastomer in SET resembles actual downhole conditions, which should be circumvented. The appropriate sealing material must be chosen based on the downhole operating conditions (Qiao et al., 2024).
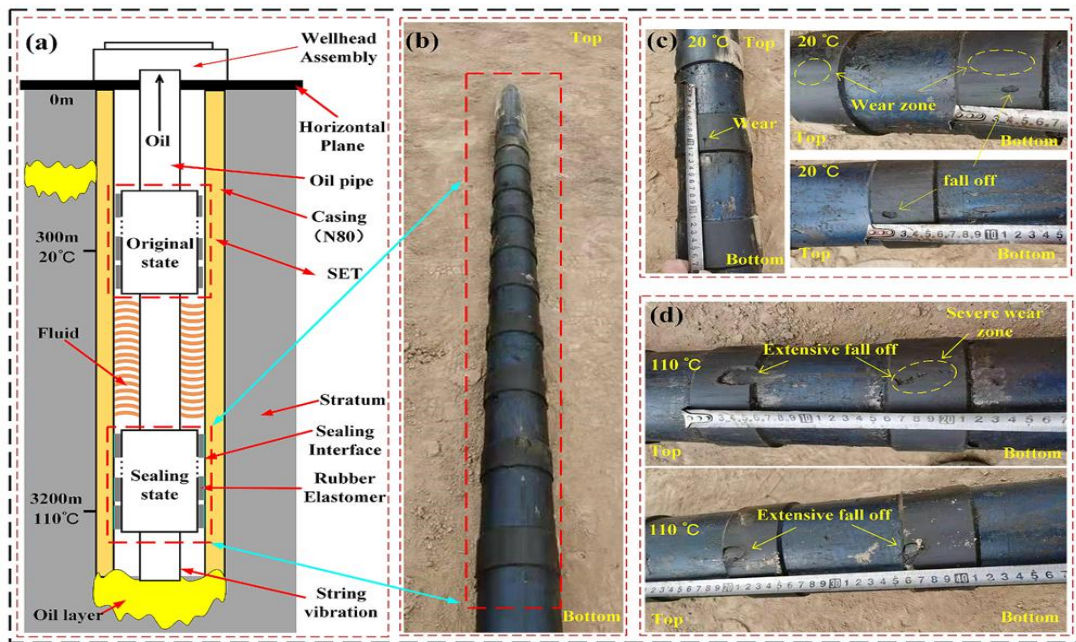

Fig.2.13. Depicted of sealing & shaft failure of solid expandable tubular (Qiao et al., 2024).

Seals can fail due to many causes, including abrasion, compression set, and chemical and thermal degradation. In the case of dynamic seals, surface wear progressively increases over time, ultimately resulting in the formation of a gap and subsequent leakage. The reliability of seals is essential for the prolonged lifespan of machinery, as failure may result in catastrophic damage. Like other materials, elastomers are susceptible to wear during prolonged sliding contact, which is recognised as the primary cause of dynamic seal failure. Therefore, to enhance the design of seals for extended durability, a comprehensive understanding of the tribological properties of seal materials is essential. The tribological behaviour of elastomers is significantly affected by the material's viscoelastic properties, in contrast to metals or ceramics (Lee et al., 2012). Prolonged stress on the contact area will ultimately result in the degradation and failure of the seal's surface. To avert such a failure, the seal must be replaced promptly; however, premature replacement is inadvisable since it results in machine downtime and cost detriment.

The failure of reciprocating seals may lead to environmental contamination, a significant decrease in system efficiency, and jeopardise the safety of the hydraulic system. Combined seals integrate the benefits of rubber's hyper-elasticity with PTFE's low friction coefficient and superior anti-wear properties. In certain critical operational environments, such as aerospace hydraulic systems and deep-sea manipulators, a single lip is insufficient to ensure seal dependability; hence, double-lip seals are recommended The two-lip configuration also presents several issues, including increased frictional force relative to the single-lip seal. The PTFE component of the composite seal exhibits a reduced friction coefficient. The integration of combined seals with a double-lip structure mitigates high-friction issues and is gaining popularity in reciprocating applications (Peng et al., 2023).
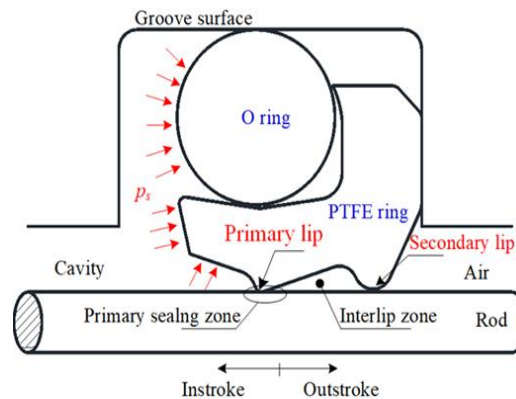

Fig.2.14. Schematic of the double-lipped seal (Peng et al., 2023).

Polytetrafluoroethylene (PTFE) rotary lip seals are extensively utilised for sealing industrial components, such as crankshafts, in high-temperature, high-pressure, or other severe environmental conditions that elastomeric rotary lip seals cannot endure. The contact width and pressure between the seal and spinning shaft may alter owing to wear, leading to leakage after extensive cyclic operations (Huang et al., 2022). Standard PTFE lip seals typically exhibit elevated leak rates at high velocities. To characterise the microscopic roughness of the seal lip, samples of the PTFE rotary lip seal with the cross-sectional geometry parameters were manufactured. The seal consists of a PTFE lip and a rubber gasket affixed to a metallic frame.
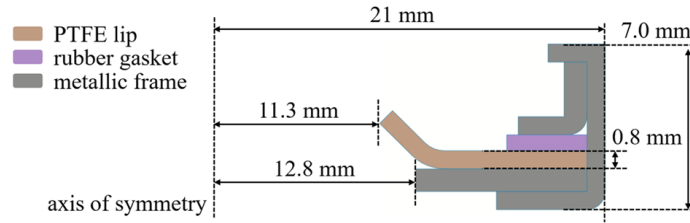
Fig.2.15. Represent of the cross sectional geometry of lip seal (Huang et al., 2022).

Polytetrafluoroethylene rotary lip seals are frequently utilised as industrial components due to their ability to endure extreme conditions, including elevated temperatures, pressures, and chemical corrosion. Nevertheless, alterations in the seal lip shape resulting from wear may impair sealing efficacy under high cycle loading situations. Experimental findings indicated that PTFE rotary lip seals exhibit more frictional torque compared to rubber seals following prolonged use. Progressive alterations in the seal lip shape owing to wear may result in substantial fluctuations in contact pressure, potentially leading to leakage. The asperity contact pressure is computed and used into the modified Archard wear model to evaluate the wear depth of the seal lip during lubricated operation (Huang et al., 2023).

Identifying the fundamental frictional events and failure characteristics just through seal simulation is challenging. Therefore, experimental research is essential for comprehending the frictional characteristics of sealing rings. Enhanced velocity typically led to an escalation in friction. The material properties and testing conditions affected the surface temperature and leakage rate. The wear mechanisms were contingent upon the material composition. The comprehensive indications demonstrate that PEEK and PTFE composites are more suitable as materials for sealing rings within a pv factor range of $8-65.4\ MPa \cdot m/s$ (Gong et al., 2015).

To avert contamination of H_2 by volatile compounds like lubricating oils and greases, oil-free reciprocating compressors are often utilised, with sealing and lubrication reliant on the characteristics of sealing rings. These components must adhere to stringent criteria, exhibiting low friction coefficients and minimal wear rates against steel, to guarantee maximum performance. The motion of sealing components in high-pressure hydrogen storage systems induces fretting, rendering the seals more susceptible to failure than conventional sliding mechanisms. When hydrogen is diluted with nitrogen, the tribological performance of PTFE enhances, while tribo-chemistry is not facilitated (Yin et al., 2025).

Polymer-based sealing materials presently hold significant importance across nearly all industrial sectors. Owing to its exceptional chemical resistance and low friction coefficient, PTFE seals are extensively utilised in various sectors, including traditional sealing markets such as pneumatics and hydraulics, as well as aerospace, energy, oil and gas, life sciences, and renewable energy. Notwithstanding its exceptional qualities, PTFE exhibits inadequate wear resistance, leading to leakage issues during sealing. The wear resistance of PTFE can be markedly enhanced with appropriate filler material additives. In commercial PTFE-based composite seals, the prevalent micro-sized fillers include glass fibre, graphite, molybdenum disulphide, and bronze (Daneshmand et al., 2023). The incorporation of micro-sized (1–100 µm) fillers can diminish PTFE wear by a factor of 10 to 100.

2.4   Regolith: Abrasives on Mars and Moon

The hardness and grain structure significantly influence the abrasive characteristics of geological materials. The lunar regolith exhibits high abrasivity, posing risks to astronauts and

equipment during lunar missions. Therefore, it is crucial that any simulants employed in mechanical testing of equipment designed for lunar surface operations accurately replicate the abrasive properties of genuine lunar regolith. Previously established simulants with inadequate mineralogical fidelity, such as JSC-1AF and NU-LHT-2 M, demonstrate abrasiveness comparable to or less than that of regular silica. LHS-1 and LMS-1, which are mineralogically precise, exhibit considerably more abrasiveness at the 95% confidence level compared to ordinary silica, alumina, JSC-1A, and NU-LHT-2 M. LMS-1 is considerably more abrasive than LHS-1, and both LHS-1 and LMS-1 exhibit greater abrasiveness than the standard materials and other examined simulants, attributable to the variances in mineralogy across these simulants (Long-Fox et al., 2023). The findings affirm that mineralogical precision is crucial in the mechanical testing of lunar regolith simulants, as the inherent grain morphology and hardness of each mineral influence the total abrasiveness.

During the Apollo period of lunar exploration, unforeseen challenges arose from the harmful abrasion of materials caused by exposure to the tiny, irregularly shaped dust on the Moon's surface. The examination of lunar abrasion difficulties is part of the Dust Management Project (DMP) project at the National Aeronautics and Space Administration (NASA) to address challenges in future exploration missions. Accurately estimating the material lifespan for activities is essential, as it affects launch mass and failure mechanisms. The specific impacts of lunar dust on Extravehicular Activity Systems (EVAS) during the Apollo era were highlighted, along with the observation that the gravity of dust-related issues was continually underestimated by terrestrial experiments. The lunar science community recognised the abrasive characteristics of lunar dust as one of the five most significant physical qualities of interest. The significance of abrasion was classified as 'high' due to its impact on any material that is in motion or possesses a sealing surface. To build space exploration equipment that will interact with dusty regolith, the aforementioned input parameters can be characterised and theoretically integrated to formulate a non-dimensional abrasion index. The establishment of an abrasion index serves as a design tool to enhance the efficacy of exploration systems in several domains: identification of abrasive risks; formulation of specific mitigation strategies; mission design, including landing sites or field operations; hardware design; laboratory testing protocols; and material selection for surface systems. An abrasion index is established that encompasses risk level, mineral hardness, abrasion mode severity, and frequency of particle contacts (Kobrick et al., 2011).

The moon of Earth is enveloped in a thin layer of loosely aggregated, unconsolidated substance known as "lunar regolith." The superior strata, referred to as "lunar dust," posed several challenges during the Apollo lunar missions in the 1960s and 1970s. A primary and harmful characteristic of lunar dust is its capacity to abrade surfaces. During the Apollo 17 lunar mission, lunar dust abraded the sunshade of NASA astronaut Harrison Schmitt's helmet, impairing his visibility in some directions. Lunar dust extensively eroded gauge dials, rendering them illegible. Lunar dust caused considerable abrasion to the textiles of the astronaut's extravehicular mobility unit (EMU) spacesuit. Lunar dust-induced wear, influenced by its effects on the Apollo missions and the anticipated plans for further lunar trips, has been a focal point of research for several years. The literature identifies two principal wear mechanisms of lunar dust particles: abrasive wear and erosive wear (Mpagazehe et al., 2014).

Mars Global Simulants (MGS-1) are also advised for applications involving the testing of flight hardware, such as drilling, where geomechanical qualities are critical. MGS-1 is suitable for these instances as the synthesis procedure yields a "regolith" of polymineralic grains with a customisable particle size distribution, rather than merely combining dry powders. Nevertheless, the geomechanical characteristics of authentic Martian regolith are inadequately defined in contrast to the widely analysed lunar regolith returned to Earth. Furthermore, the

prototypes lacked control over specific factors like as particle morphology, which can significantly affect geomechanical behaviour, and our preliminary assessments of physical attributes in this study are constrained. Alternative simulants, especially those derived from lunar sources, have gained from comprehensive crushing methods designed to emulate lunar geomechanical characteristics. Currently, it can only be asserted that MGS-1 based simulants may be rendered equally suitable or more so for hardware testing in comparison to prior Mars simulants (Cannon et al., 2019).

Regolith is a broad term that refers to the layer of fractured and unconsolidated rock components, with formation processes differing across various locations or planetary bodies. Regolith is generated on Earth by distinct terrestrial processes that utilise oxygen, the effects of wind and water, and various other terrestrial activities. Conversely, the lunar regolith is a product of the incessant impact of meteoroids and the bombardment of the lunar surface by charged particles predominantly originating from the Sun. The Martian regolith comprises a combination of weathered and aeolian materials. The upper 5-meter layer of Martian regolith primarily consists of nearly cohesionless basaltic sand and a limited number of pebbles. Concerning the deeper strata, it is anticipated that they comprise a multitude of bigger particles and rocks. The compositions of Lunar and Martian regolith exhibit shared properties. Specifically, oxides such as Silicon dioxide (SiO_2) and Aluminium oxide (Al_2O_3) constitute the predominant components of both Martian and Lunar soil, exhibiting nearly identical weight percentages (Kalapodis et al., 2020).

Table 2.8. List of Lunar and Martian original sample sand simulants (Kalapodis et al., 2020).

Lunar Regolith			Martian Regolith		
Original Samples	1	Lunar Orbiter (1966)	Original Samples	1	Viking Lander 1 (1975)
	2	Surveyor I (1966)		2	Viking Lander 1&2 (1975)
	3	Surveyor III And VI (1967)		3	Viking Lander 2 (1975)
	4	Apollo 11 (1969)		4	MPF Sojourner (1996)
	5	Apollo 12 (1969	Simulants	5	JSC Mars-1
	6	Luna-16 (1970)		6	JPL Lab 107
	7	Apollo 14 (1971)		7	JPL Lab 82
	8	Apollo 15 (1971)		8	MER Yard 317
Simulants	9	JSC-1		9	MARS Yard
	10	MLS-1		10	MMS sand I
	11	FJS-1		11	MMS sand II
	12	FJS-2		12	MMS dust I
	13	FJS-3		13	MMS dust II
	14	JSC-1A		14	ES-1
	15	TJ-1		15	ES-2
	16	TJ-2		16	ES-3
	17	GRC-3		17	JMSS-1
	18	CAS-1			
	19	BP-1			

2.5 Space applications and abrasive wear

Bogie electro-mechanical assemblies (BEMA): In the European Space Agency's (ESA) Rosalind Franklin Mars rover mission, MacDonald Dettwiler and Associates (MDA), a subsidiary of Maxar Technologies Ltd., designed the BEMA to facilitate the rover's locomotion (Kanji & Buratynsky, 2019). A comprehensive testing programme was conducted to mitigate technical risks for the inaugural European-funded rover scheduled for deployment to mars in 2020. The Rosalind Franklin rover is a mars rover mission led by ESA and Roscosmos, scheduled for launch in 2020, subsequent to the Exomars Trace Gas Orbiter, which was deployed to orbit Mars in 2016. The Rosalind Franklin rover will utilise the Orbiter as a

communication relay to drill into the Martian surface to a depth of two metres in pursuit of life, whether past or present.
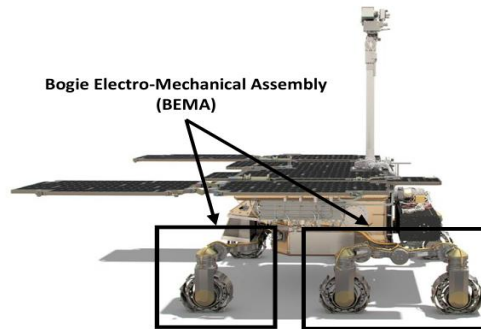

Fig.2.16. BEMA on the Rosalind Franklin rover (Kanji & Buratynsky, 2019).

The rover features a Canadian-engineered locomotion technology known as BEMA, created by MDA in Brampton and Montreal. The BEMA comprises the wheels and suspension system of the rover, featuring six compliant metal wheels, each associated with three freely rotating bogie beams.
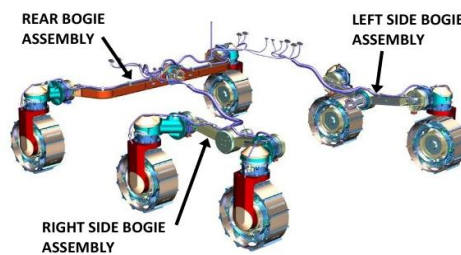

Fig.2.17. BEMA wheels and suspension system (Kanji & Buratynsky, 2019).

BEMA rotary actuators: The ExoMars 2020 mission is a collaborative project between the European Space Agency (ESA) and the Russian Space Agency (Roscosmos) (Grandy et al., 2019). The Kazachok lander (Roscosmos) will be transported to the Martian surface, from where the Rosalind Franklin rover (ESA) will be deployed. The mission prime contractor is Thales Alenia space Italy, while airbus defence and space oversees the rover module, with the locomotion subsystem built by MDA. The principal scientific aims of the Exomars rover are to investigate evidence of past or present life on mars and to describe the water and geochemical conditions in the shallow subsurface. The vehicle is outfitted with an exobiology sensor suite, ground-penetrating radar, and a drill capable of extracting samples from a depth of up to 2 metres to achieve these aims.
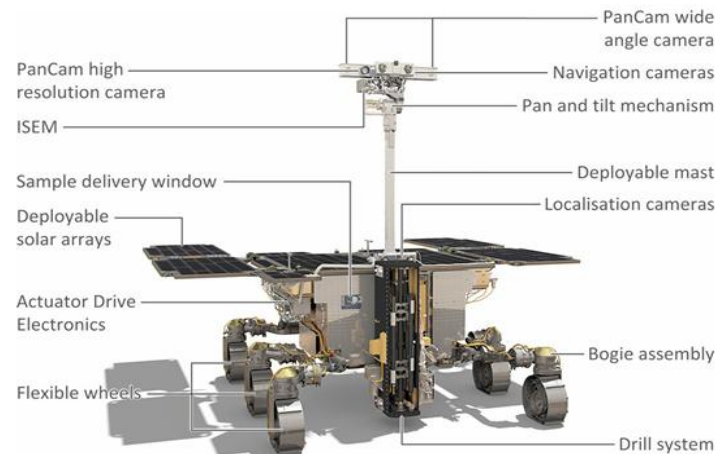
Fig.2.18. Exomars rover showing key subsystems (Grandy et al., 2019).

Mars exploration rover (MER): Three mechanisms were created for the mars exploration rover (MER) programme, which aims to land two rovers on the Martian surface in January 2004: The microscopic-imager dust cover, the microscopic-imager contact sensor, and the mössbauer spectrometer contact sensor (Dougherty, 2003). These processes augment the functionalities of the rovers and their in situ scientific instruments, particularly the microscopic imager (MI) and mössbauer spectrometer (MB), positioned at the terminus of the rover's robotic arm. The MI dust cover mechanism safeguards the lens of the microscopic imager against dust and accidental contact when the instrument is not operational. The cover opens when the MI is aligned with a target and closes when a sequence of photos has been captured. The MI and MB contact sensors detect touch with the Martian surface, signifying that the instrument is correctly positioned relative to the target and can commence measurements. The MER programme was initiated in the summer of 2000, aiming to land two rovers on mars in January 2004. The MER is integral to NASA's ongoing initiative to investigate mars, with the jet propulsion laboratory (JPL) assuming main responsibility for its development, consistent with prior mars missions.

Fig.2.19. MER on the surface of mars (Dougherty, 2003).

Nanokhod micro rover: Mobile robotic rover systems are essential for planetary surface exploration missions and can yield a substantially greater scientific return. Given the stringent limitations on available payload mass for planetary lander systems, the development and implementation of compact mobile exploration systems is essential. The miniaturisation of essential mechanisms for micro rover systems, capable of enduring the severe conditions of space and planetary environments, is particularly challenging (Gewehr et al., 2021). Potential mission scenarios on the lunar surface for the future application of the tethered The study examined the prerequisites for a prolonged mission lasting up to one year, the accessibility of

harsh conditions such as crater slopes, lava tubes, and collapsed skylights, along with prospective (micro-) swarm uses.
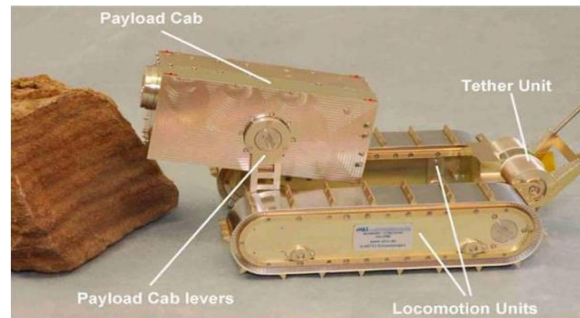

Fig.2.20. Nanokhod micro rover model for mercury robotic payload (Gewehr et al., 2021).
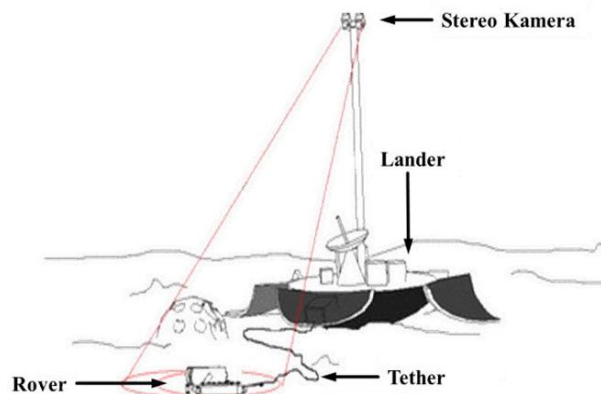

Fig.2.21. Sketch: Nanokhod mission scenario for bepicolombo (Gewehr et al., 2021).

Sealed brush gear motor (SBGM): Brushed DC motors sometimes exhibit reliability concerns in a vacuum due to problems with the brushes in the commutator. The proposed actuator addresses problems such as debris production from brushes, arcing, and excessive brush friction by the implementation of a hermetically sealed housing that maintains its own atmosphere (Zimmermann et al., 2013). The minimal leak rate maintains the internal pressure at an adequate level for almost 50 years in orbit. Torque is conveyed from the motor to the gear head using a magnetic hysteresis coupler. This coupler possesses a distinctive feature that enables it to not only restrict the transmitted torque but also to sustain the pre-set torque during slippage within the coupler.
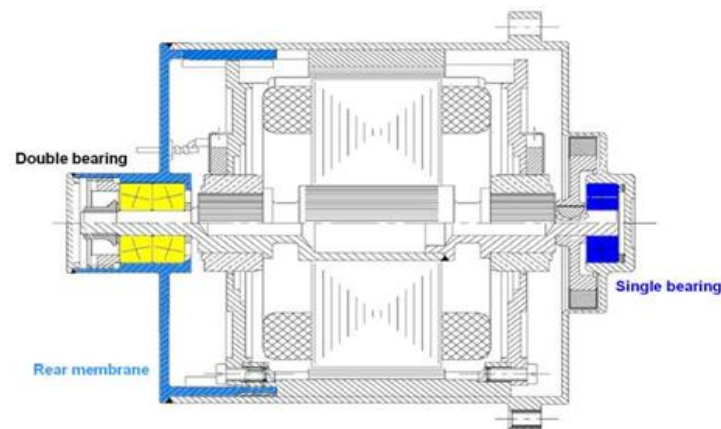

Fig.2.22. SBGM sealed motor (Zimmermann et al., 2013).

The moon's surface is coated with a coating of fragmented, space-altered rock, referred to as lunar regolith. Darker and brighter parts on the lunar surface are referred to as mare and highland regions, respectively. The lunar mares are composed of the oldest lunar regolith. The highland regions constitute the moon's extensively cratered zones. The earth's moon is not only a subject of significant scientific interest but also presents considerable technical challenges. Significant temperature disparities exist between shaded regions and those immediately exposed to sunlight, alongside high vacuum and radiation conditions; yet, as Gene Cernan said following the Apollo 17 mission, lunar dust may offer one of the most formidable difficulties for future lunar expeditions (Bühler, 2015).

The moon of earth is enveloped in a thin layer of loosely aggregated, unconsolidated substance known as "lunar regolith." The superior layers, referred to as "lunar dust," presented several challenges during the Apollo lunar missions in the 1960s and 1970s. A primary and harmful characteristic of lunar dust is its capacity to abrade surfaces (Mpagazehe et al., 2014).

During the Apollo era of lunar exploration, unforeseen challenges arose due to the harmful abrasion of materials caused by the fine-grained, irregularly shaped dust on the Moon's surface, as documented by Gaier at the national aeronautics and space administration (NASA) glenn research centre (GRC). The examination of lunar abrasion difficulties is part of NASA's dust Management Project (DMP) project, aimed at reducing these challenges in future exploration missions. A primary objective of the research done within the DMP is to formulate recommendations and standardised testing methodologies for assessing the effects of lunar dust abrasion on proposed surface system materials and operations (Kobrick et al., 2011).

When space application robots, such as rovers, were deployed to the moon, specifically on the surface of the lunar highland. The failure of rover assembly components, such as the rotary shaft and static seal, was attributed to friction and wear. Due to the ingress of hard abrasive dust particles originating from the lunar highland of the moon. Lunar science community recognised the abrasive characteristics of lunar dust as one of the five primary physical features of interest. The significance of abrasion was classified as 'high' due to its impact on any material that is in motion or possesses a sealing surface (Kobrick et al., 2011). Abrasion, in the domain of tribology, constitutes one of the four fundamental types of wear or mechanisms for material removal or displacement (fig.2.23) and represents the most severe and expensive form of wear. While fig.2.24 examines interactions between two analogous or dissimilar space building materials and dust, it may essentially be seen as dust separately interacting with each surface under the same applied force.
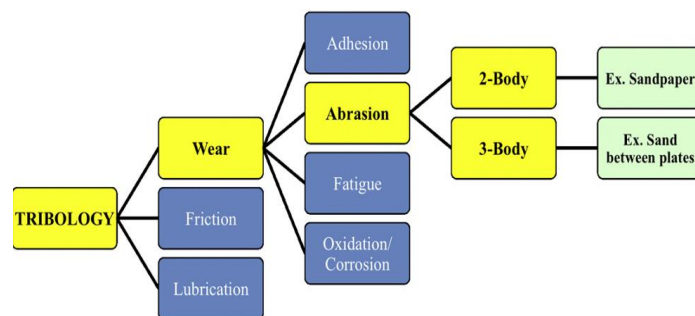

Fig.2.23. Summary of tribology and classifications of wear in relation to lunar abrasion (Kobrick et al., 2011).
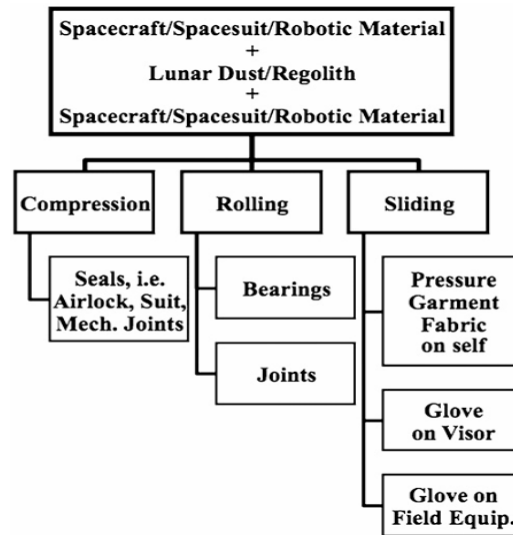
Fig.2.24. Materials & parts engaging with lunar dust in mutual interaction (Kobrick et al., 2011).

Polytetrafluoroethylene (PTFE) seals and bearings find extensive application in aerospace, energy, oil, and gas, etc. PTFE offers numerous benefits, including affordability, long-lasting durability, recyclability, low friction, self-lubricating characteristics, and a reduction in stick-slip phenomena. PTFE exhibits drawbacks such as creep or cold flow behaviour, leading to significant deformation even at room temperature when subjected to continuous applied load. It shows minimal resilience and wears out rapidly (B. Tan & Stephens, 2019).

The harsh attributes of the lunar environment, including a temperature fluctuation of approximately 150 °C during the day and -225 °C at night, along with solar and intergalactic cosmic radiation, and lunar regolith, contribute to premature failures. Lunar dust is regarded as the most detrimental factor, inflicting significant abrasive and erosive damage on material systems. The angular particles in lunar dust, resulting from the absence of wind and water erosion, enhance the friction angles and cohesive forces relative to terrestrial soils. Abrasive wear tests have been performed with lunar simulants due to the scarcity of regolith reserves on earth. Lunar simulants are substances that imitate the morphological and elemental characteristics of lunar regolith utilising accessible terrestrial resources. Abrasive wear was primarily influenced by the particle size of the simulant and its hardness (Sukumaran et al., 2023). JSC-1A and Greenland Anorthosite (GA) lunar simulants were acquired from NASA's marshall space flight centre located in Huntsville, Alabama. GA, a representation of the lunar highlands depicted in Fig. 2.25A and B, is abundant in calcium and aluminium.
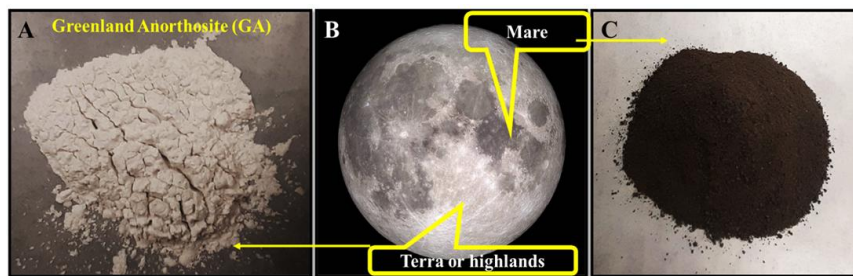

Fig.2.25. Depicted: (A. Greenland Anorthosite ,B. mare and highlands, and C. JSC-1A) (Sukumaran et al., 2023).

2.6   Discrete Element Model (DEM)

The discrete element method (DEM), developed by Cundall and Strack ((Jiménez-Herrera et al., 2018)., is a simulation technique that models the motion and interactions of rigid independent particles using Newtonian laws of motion and contact models DEM has gained broad acceptance as an efficient approach for resolving engineering challenges in granular and discontinuous materials, particularly in granular flows, rock mechanics, *powder mechanics*, fluidised beds, and comminution. DEM are computationally demanding, restricting either the duration of a simulation or the particle count.

The bonded-particle model (BPM) was created to accurately replicate the behaviour of particles resembling a cemented granular material composed of irregularly shaped grains and cement, where the connections (cement) may fracture when subjected to force over a critical threshold. The BPM conceptual model can, in theory, elucidate various facets of the particle's mechanical behaviour. The connections represent an element that unites two spheres (*i* and *j*), functioning as a cementing bond (Fig.2.26). Upon establishing the connections, the forces and torques among the fundamental particles are computed using expressions that reflect the bonds inside the model (Jiménez-Herrera et al., 2018).
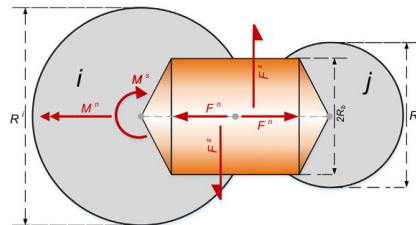

Fig.2.26. Illustration of the bonded-particle model (BPM) (Jiménez-Herrera et al., 2018).

Progress application of discrete element Model: Models of discrete element types have been developed for geotechnical purposes and subsequently utilised in several fields, including tribology (Iliescu et al., 2010).Subsequent models utilising discrete elements have been suggested for the examination of the abrasion process. These models, utilising a Lagrangian framework, track the motion of each particle. The laws of particle interaction are the forces exerted on these particles. The integration of the fundamental law of dynamics enables the calculation of each particle's trajectory. The application of these models to quantitatively mimic an actual scenario remains challenging. Nevertheless, they appear especially adept at elucidating fundamental physical phenomena.

2.6.1   *The fundamental principles of discrete element model (DEM)*

As it was summarized (Yeom et al., 2019):

- The force exerted by adjacent particles or boundaries on each particle is computed in a single time step utilising the contact model.
- Newton's second law is employed to determine particle velocity.
- Similarly, rotational momentum balances are resolved to monitor the rotational velocity of particles.
- The new position of the particle is calculated for a specified time-step duration.

DEM is often categorised into four models: cellular automata (CA), Monte Carlo method, hard-sphere model, and soft-sphere model (Yeom et al., 2019).

The merits and demerits of the hard-sphere and soft-sphere models have been elucidated comprehensively in numerous research.

In the hard-sphere model, particles are regarded as rigid, and contact between particles, dictated by the binary contact rule, is presumed to be immediate, as illustrated in fig.2.27a (where V_1 and V_2 the velocity of each particle before contact; V_1' and V_2' the velocity of each particle after contact). This premise indicates that the hard-sphere model is appropriate for conditions of significant agitation or microgravity.

Consequently, the hard-sphere model may exhibit computing efficiency when utilised in a relatively sparse system (Yeom et al., 2019).

The soft-sphere model is perhaps the most prevalent and adaptable in discrete element modelling (DEM) (Yeom et al., 2019). The soft-sphere model posits that particle contact is enduring, as illustrated in fig.2.27b, and allows for both multiple and binary connections between particles.

The assumptions regarding particle contact suggest that the soft-sphere model is advantageous for examining prolonged and numerous particle interactions in a densely packed environment.

The soft-sphere model entails a straightforward simulation approach comprising the following steps (Yeom et al., 2019):

- Configuring the properties of particles and equipment within the computational domain

- Introducing the particles into the computational domain by specifying their position and velocity

- Identifying particle-particle and particle-geometry interactions

- Computing the forces exerted on each particle utilising a suitable contact model

- Establishing particle acceleration through Newton's second law, which is integrated over time to ascertain the updated particle states, including position and velocity.
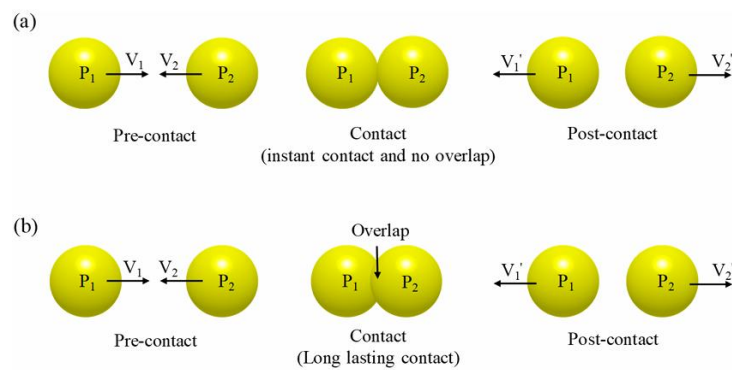

Fig.2.27. Diagram of (a) hard-sphere model and (b) soft-sphere model (Yeom et al., 2019).

Contact model: The contact model can be classified based on the physical properties of particles, including elasticity, plasticity, viscosity, dry friction, and adhesion (Yeom et al., 2019). Detailed classification of interaction force models between particles to particles and particles to geometries, categorised into contact and non-contact forces.
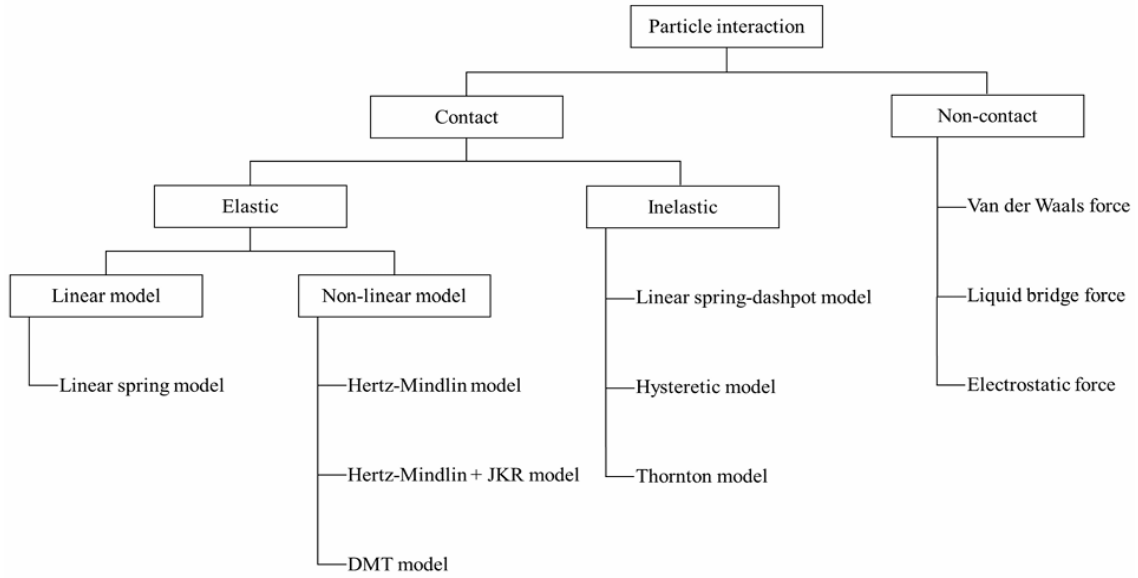
Fig.2.28. Categorisation of particle interaction force models based on contact and non-contact forces (Yeom et al., 2019).

Fig.2.29 indicates the complex relationship between force and displacement across different contact models:

(a)   Linear spring model

(b)   Hertz-Mindlin model

(c)   Hertz-Mindlin + JKR model
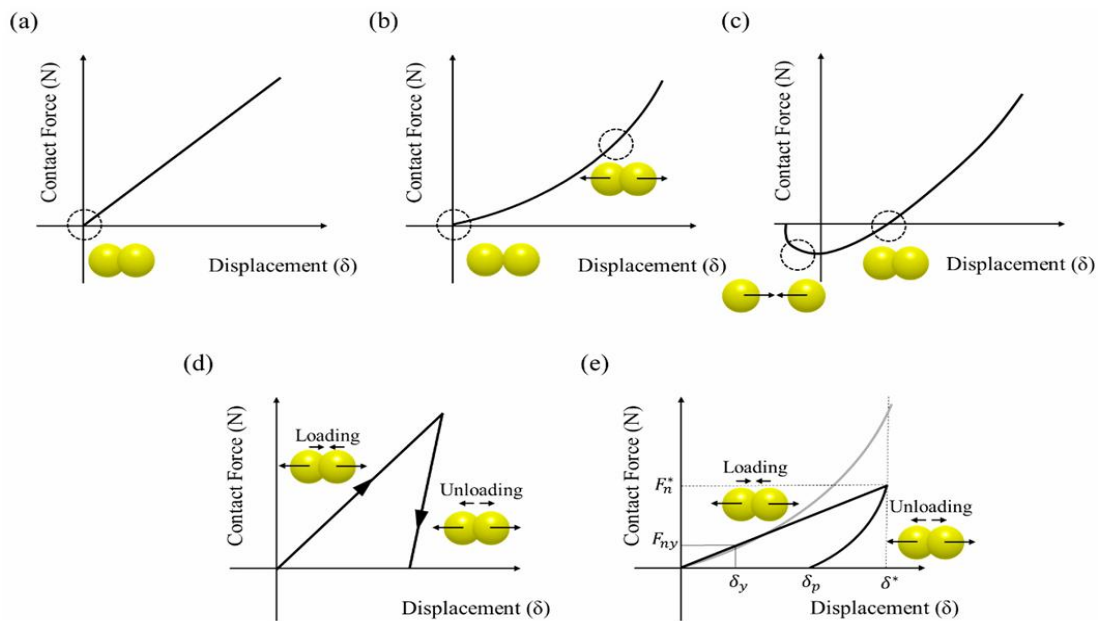
(d)   Hysteretic model

(e)   Thornton model

Fig.2.29. Relationship between force and displacement in various contact models (Yeom et al., 2019).

2.6.2 Linear elastic model

A perfectly elastic collision in which the particle expends no energy and exits the collision with the identical velocity it possessed initially (J. Thompson, 2023).

Elastic contact models are often categorised as linear elastic or nonlinear elastic models. The linear elastic model is simplified to a spring, whereas the nonlinear elastic model is founded on the more intricate Hertz theory (Yeom et al., 2019).

Linear spring model is the fundamental contact model that illustrates the linear correlation between force and displacement, as depicted in fig.2.29a. This linear relationship is obtained from the subsequent equations (Yeom et al., 2019):

$$F_n = -K_n \delta_n \tag{2.14}$$

$$F_t = -K_t \delta_t \tag{2.15}$$

Where:

F_n Normal contact force

F_t Tangential contact force

δ_n Normal displacement

δ_t Tangential displacement

K_n Normal spring constant

K_t Tangential spring constant

2.6.3 Nonlinear elastic contact model

The realistic situation in which a particle releases certain amounts of its energy into the impacted material (J. Thompson, 2023).

Hertz-Mindlin model: The Hertz-Mindlin model is a quintessential nonlinear elastic model that delineates the nonlinear correlation between normal force and displacement, as illustrated in fig2.29b. The Hertz-Mindlin model posits that contact between two particles in the normal direction is derived from Hertz's hypothesis (Yeom et al., 2019). The interaction between two particles in the tangential direction was posited by the Mindlin and Deresiewicz theory (Yeom et al., 2019). The comprehensive Hertz-Mindlin model outlined in prior studies possesses a computational constraint owing to its significant complexity. Furthermore, the comprehensive Hertz-Mindlin model is computationally intensive when applied to the contact of several particles. Consequently, the Hertz-Mindlin model was refined to the Hertz-Mindlin no slip model, drawing on Hertz's theory for the normal direction and Mindlin's enhanced no slip model for the tangential direction (Yeom et al., 2019). In the Hertz-Mindlin no-slip model, the normal and tangential contact forces are determined using the following equations (Yeom et al., 2019):

$$F_n = -\frac{4}{3} E^* \sqrt{R^*} \delta_n^{3/2} \tag{2.16}$$

$$F_t = 8 G^* \sqrt{R^* \delta_n} \delta_t \tag{2.17}$$

Where:

E^* Equivalent Young's modulus and $E^* = \left(\frac{1-v_i^2}{E_i} + \frac{1-v_j^2}{E_j} \right)^{-1}$

v Poisson's ratio of the two particles in contact

E Young's modulus of the two particles in contact

R^* Equivalent radius and $R^* = \left(\frac{1}{R_i} + \frac{1}{R_j} \right)^{-1}$

R particle radii of the two particles in contact

G^* Equivalent shear modulus and $G^* = \left(\frac{1-v_i}{G_i} + \frac{1-v_j}{G_j} \right)^{-1}$

G shear modulus of the two particles in contact

In the Hertz-Mindlin contact model, the contact force is decomposed into a non-linear Hertz component and a damping component (Coetzee, 2017):

$$F_c = F_h + F_d \tag{2.18}$$

Where:

F_c Contact force

F_h Non-linear Hertz component

F_d Damping component

The Hertz component can be further delineated into normal and tangential components (Coetzee, 2017):

$$F_h^n = k_n \delta_n \tag{2.19}$$

$$F_h^t = (F_l^t)_0 + k_t \Delta \delta_t \tag{2.20}$$

Coulomb-type frictional slip is permitted in the tangential direction, indicating that the computed shear force (Coetzee, 2017):

$$F_l^t = \begin{cases} F_{l_*}^t \text{ if } F_{l_*}^t \leq \mu F_l^n \\ \mu F_l^n \text{ otherwise} \end{cases} \tag{2.21}$$

The normal stiffness and shear stiffness are expressed in relation to the material's modulus of elasticity and the particle radius (Coetzee, 2017):

$$k_n = \frac{4}{3} E^* \sqrt{R^* \delta_n} \tag{2.22}$$

$$k_t = 8 G^* \sqrt{R^* \delta_n} \tag{2.23}$$

The damping forces in the normal and tangential are specified as follows (Coetzee, 2017):

$$F_d^n = C_n \dot{\delta}_n \delta_n^{1/4} \tag{2.24}$$

$$F_d^t = C_t \dot{\delta}_t \delta_t^{1/4} \tag{2.25}$$

Where:

C_n Damping coefficients in the normal direction

$\dot{\delta}_n$ Normal velocity in the normal direction

C_t Damping coefficients in the shear direction

$\dot{\delta}_t$ Tangential velocity in the tangential direction

The damping coefficients in the normal and shear are specified as follows (Coetzee, 2017):

$$C_n = \frac{lne}{\sqrt{ln_e^2 + \pi^2}}\sqrt{m^* k_n} \tag{2.26}$$

$$C_t = \frac{lne}{\sqrt{ln_e^2 + \pi^2}}\sqrt{m^* k_t} \tag{2.27}$$

Where:

e Coefficient of restitution

The contact model is employed in DEM calculations to simulate particle collisions. Fig.2.30 illustrates the schematic diagram of the contact force model between two particles, A and B. The Hertz–Mindlin no-slip contact model inside the discrete element approach is employed to compute the normal force when discrete particles are in elastic contact with the structure. As particle and structural deformation are excluded from the DEM computation, the collision between a particle and the wall is effectively analogous to the collision between particles, allowing the wall to be regarded as a particle as well (Jiang & Xie, 2023). In the event that two spherical particles collide and make contact, their normal overlap is defined as:

$$\delta_n = R_1 + R_2 - |r_1 - r_2| \tag{2.28}$$

Where:

r_1 Position vector of spherical center one
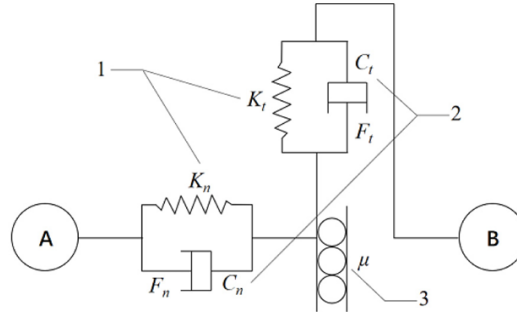
r_2 Position vector of spherical center two

Fig.2.30. Contact model (1. spring stiffness 2. Damper 3. Friction) (Jiang & Xie, 2023).

Contacts between particles and between particles and walls are computed using the Hertz-Mindlin model (Luo et al., 2021). Utilising the soft ball model, continuous multi-sphere contact was established by the dynamic monitoring of particle interactions. The velocity of particles generally adheres to Newton's second law and is affected by gravitational and contact forces. The equations of motion are as follows (Luo et al., 2021):

$$m_P \frac{dv_P}{dt} = mg + F_c \tag{2.29}$$

$$\frac{d\omega_P}{dt} = \frac{M_P}{I_P} \tag{2.30}$$

Where:

M_P Torque of particle centre mass

I_P Particle's moment of inertia

The total normal force is the aggregate of the normal force component and the damping normal force component (Jiménez-Herrera et al., 2018):

$$F_n = -K_n \delta_n + C_n \overrightarrow{v_n^{rel}} \tag{2.31}$$

Where:

C_n Damping coefficient in normal and $C_n = 2\sqrt{\frac{5}{6}}\beta\sqrt{S_n m^*}\overrightarrow{v_n^{rel}}$, $S_n = 2E^*\sqrt{R^*\delta_n}$

β Damping ratio expressed by $\beta = \dfrac{lne}{\sqrt{ln_e^2+\pi^2}}$

$\overrightarrow{v_n^{rel}}$ Normal component of the relative velocity

The total tangential force is limited by Coulomb's law of friction, yielding (Jiménez-Herrera et al., 2018):

$$F_t = \min\left\{\mu_s F_n, K_t \delta_t + C_t \overrightarrow{v_t^{rel}}\right\} \tag{2.32}$$

Where:

C_t Damping coefficient in tangential and $C_t = 2\sqrt{\frac{5}{6}}\beta\sqrt{K_t m^*}\overrightarrow{v_t^{rel}}$

$\overrightarrow{v_t^{rel}}$ Tangential component of the relative velocity

μ_s Coefficient of static friction

The particle interacts with adjacent particles or boundaries during motion, facilitating the exchange of momentum and energy (Rong et al., 2023). The inter-particle contact model is illustrated in Fig.2.31 (a), featuring springs and dashpots in the normal direction, together with springs, dashpots, and sliders in the tangential direction. Fig.2.31 (b) the interaction forces among particles. According to Newton's second rule of motion, at any certain time t, the equations regulating the translational and rotational motion of particles are expressed as follows (Rong et al., 2023):

$$m_i \frac{du_i}{dt} = \sum_{j=1}^{n_i}\left(F_{cn,ij} + F_{ct,ij} + F_{dn,ij} + F_{dt,ij}\right) + m_i g \tag{2.33}$$

$$m_i \frac{d\omega_i}{dt} = \sum_{j=1}^{n_i}\left(T_{t,ij} + M_{r,ij}\right) \tag{2.34}$$

Where:

n_i Total particle numbers contacting the particle i

u_i Translational velocity

ω_i Rotational velocity

I_i Rotational inertia of the particle i, $I_i = \frac{2}{5}m_i R_i^2$

$F_{cn,ij}$ Normal contact force between particles i and j and $F_{cn,ij} = -\frac{4}{3}E^*\sqrt{R^*|\delta_n|}\delta_n$

$F_{ct,ij}$ Tangential contact force between particles i and j and $F_{ct,ij} = -8G^*\sqrt{R^*|\delta_n|}\delta_t$

$F_{dn,ij}$ Normal damping force between and $F_{dn,ij} = 2\sqrt{\frac{5}{6}}\frac{lne}{\sqrt{ln_e^2+\pi^2}}\sqrt{m^*K_n}V_{n,ij}$

$F_{dt,ij}$ Tangential damping force and $F_{dt,ij} = 2\sqrt{\frac{5}{6}}\frac{lne}{\sqrt{ln_e^2+\pi^2}}\sqrt{m^*K_n}V_{t,ij}$

g Gravitation acceleration

$T_{t,ij}$ Torque from tangential forces and $T_{t,ij} = R^*n \times \left(F_{ct,ij} + F_{dt,ij}\right)$
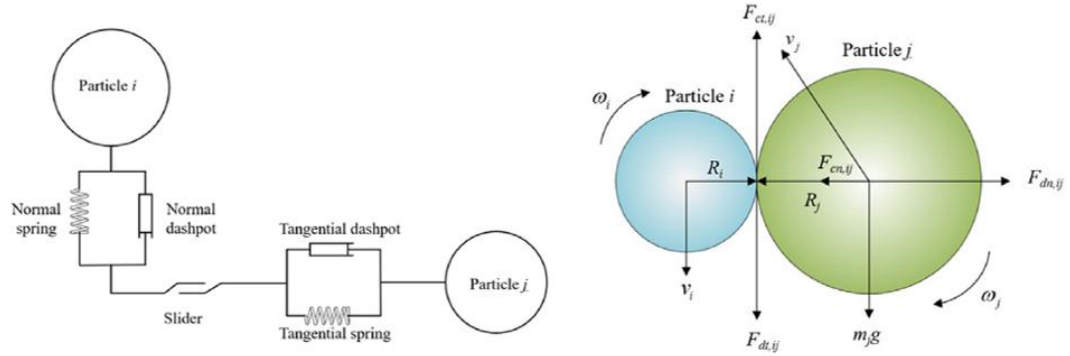
$M_{r,ij}$ Rolling friction torque and $M_{r,ij} = \frac{-\mu_r R_i |F_{n,ij}|\omega_{t,ij}}{|\omega_{t,ij}|}$

The Archard wear model is an augmented version of the normal Hertz-Mindlin model, founded on J.F. Chard's wear theory (Rong et al., 2023). This model is capable of calculating the geometric wear depth of components. The wear volume V is determined by (Rong et al., 2023):

$$V = K\frac{F_{cn,ij}\Delta S}{H} \tag{2.35}$$

Where:

ΔS Sliding distance

a) Depiction of contact model in DEM   b) Interactive forces of particles

Fig.2.31. Particle contact model (Rong et al., 2023).

Newton's second rule of motion and Euler's rotational equation (Zolotarevskiy et al., 2022):

$$\sum F_{net} = \sum F_{body} + \sum F_{surface} = m\frac{dv}{dt} \tag{2.36}$$

$$\sum M + T_{damp} = I\frac{d\omega}{dt} + \omega \times I \tag{2.37}$$

Where:

F_{net} Net (resultant) force

F_{body} Body force and $F_{body} = mg$

$F_{surface}$ Surface (contact) force acting up on particle

M Resultant moment

T_{damp} Damping moment

The numerical integration of equation (2.36) yields new translational and angular velocities v_{new}, ω_{new} at the subsequent time step, along with a new position x_{new}. The technique is thereafter reiterated until the desired system state is attained or the simulation reaches the predetermined conclusion time (Zolotarevskiy et al., 2022). This study employs the Hertz–Mindlin normal contact force model with a dampening mechanism and the Mindlin–Deresiewicz tangential contact force model. The standard contact force, expressed in relation to the typical overlap, is as follows (Zolotarevskiy et al., 2022):

$$F_n = K_H S_n^{\frac{3}{2}} + C_H s_n^{\frac{1}{4}} \dot{S}_n \tag{2.38}$$

Where:

K_H Stiffness coefficient and $K_H = \frac{4}{3} E^* \sqrt{R^*}$

C_H Damping coefficient and $C_H = \sqrt{5}\eta\sqrt{m^* K_H}$

A boundary in this context refers to the non-particle components of the system, meshed with boundary triangular elements, and R^* is designated as the equivalent radius (Zolotarevskiy et al., 2022):

$$\frac{1}{R^*} = \begin{cases} \frac{1}{L_1} + \frac{1}{L_2} & \text{for particle} - \text{particle collision} \\ \frac{1}{L} & \text{for particle} - \text{boundary collision} \end{cases} \tag{2.39}$$

Where:

L_i Contacting pair particle sizes

L A single particle size for particle–boundary collision

The tangential contact force is expressed as (Zolotarevskiy et al., 2022):

$$F_t = \mu F_n \left(1 - \zeta^{\frac{3}{2}}\right) \frac{S_t}{|S_t|} + \eta_t \sqrt{\frac{6\mu m^* F_n}{S_{t,max}}} \zeta^{\frac{1}{4}} \dot{S}_t \tag{2.40}$$

Where

$\zeta = 1 - \frac{\min(|S_t|, S_{t,max})}{S_{t,max}}$

μ Coefficient of friction and $\mu = \begin{cases} \mu_s & \text{if no sliding takes place at the contact} \\ \mu_d & \text{if sliding does take place at the contact} \end{cases}$

μ_d Dynamic friction coefficient

$S_{t,max}$ Maximum relative tangential displacement, $S_{t,max} = \mu \left(\frac{1-\nu_1}{2-\nu_1} + \frac{1-\nu_2}{2-\nu_2}\right)^{-1} S_n$

The wear in this study is forecasted using the incremental form of Archard's equation, whereby the volume loss between two successive time intervals is directly proportional to the shear work performed by particles impacting a surface during that period (Zolotarevskiy et al., 2022):

$$\Delta V = C \Delta W^t \tag{2.41}$$

Where:

ΔV Volume loss

ΔW^t Shear work performed by particles

C Volume/shear work ratio is given by $C = k/H$

Hertz-Mindlin + JKR model: The Hertz-Mindlin + JKR model was introduced by Johnson, Kendall, and Roberts, building upon Hertz's idea. This model elucidates the adhesive theory by balancing stored elastic energy with the dissipation of surface energy (Yeom et al., 2019). Fig.2.29c illustrates the nonlinear correlation between force and displacement in the Hertz-Mindlin + JKR model. The Hertz-Mindlin + JKR model exhibits an opposing force due to the adhesive pulling force that arises when contact between particles commences (Yeom et al., 2019).

The JKR model was employed to characterise the cohesive elastic force between particles (L. J. Li et al., 2022). DEM monitors the paths and rotations of discrete particles in accordance with Newton's laws of motion, expressed as (L. J. Li et al., 2022):

$$m_i \frac{dv_i}{dt} = \Sigma\left(F_{ij}^n + F_{ij}^{dn} + F_{ij}^t + F_{ij}^{dt} + F_{ij}^{bn} + F_{ij}^{bt}\right) + m_i g \qquad (2.42)$$

$$m_i \frac{d\omega_i}{dt} = \Sigma\left(M_{ij}^t + M_{ij}^r + M_{ij}^{bn} + M_{ij}^{bt}\right) \qquad (2.43)$$

Where:

F_{ij}^n Normal contact force and expressed by $F_{ij}^n = \frac{4E^*}{3R^*}a^3 - 4\sqrt{\pi\gamma E^*}a^{\frac{3}{2}}$

F_{ij}^{dn} Normal damping force and given by $F_{ij}^{dn} = -C\sqrt{E^* m^*}(R^*\delta_n)^{1/4}V_{ij,n}$

F_{ij}^t Tangential contact force and equating with $F_{ij}^t = (-8G^*\sqrt{R^*\delta_n}\delta_t, -\mu_s F_{ij}^n)\max$

F_{ij}^{dt} Tangential damping force and $F_{ij}^{dt} = -2C\sqrt{G^* m^*}(R^*\delta_n)^{1/4}V_{ij,t}$

F_{ij}^{bn} Normal bonding force and $F_{ij}^{bn} = \Sigma -k_n\pi R_B^2\Delta\delta_n$

F_{ij}^{bt} Tangential bonding force and $F_{ij}^{bt} = \Sigma -k_t\pi R_B^2\Delta\delta_t$

M_{ij}^t Torques caused by tangential force and also equate $M_{ij}^t = R_i \times F_{ij}^n$

M_{ij}^r Torques caused by rolling friction and $M_{ij}^r = -\mu_r R_i|F_{ij}^n|\widehat{\omega}_{rel}$

M_{ij}^{bn} Torques caused by normal bonding force and $M_{ij}^{bn} = \Sigma -\frac{1}{4}k_t\pi R_B^4\Delta\theta_n$

M_{ij}^{bt} Torques caused by tangential bonding force and $M_{ij}^{bt} = \Sigma -\frac{1}{4}k_n\pi R_B^4\Delta\theta_t$

C $C = 0.783$

k_n Bond normal stiffness

k_t Bond tangential stiffness

R_B Radius of rod like solid bond

R_i Vector from the particle centre point to the contact point

μ_r Rolling coefficient of friction

$\widehat{\omega}_{rel}$ Vector of relative angular velocity

$\Delta\theta_n$ Normal rotation angle in a time step

$\Delta\theta_t$ Tangential rotation angle in a time step

The Hertz–Mindlin model is predicated on a cohesive contact model with friction (Kelvin–Voigt system) and a viscoelastic sintering model (Maxwell system) (fig.2.32) (Žídek et al., 2021). The cohesive contact model with friction is characterised by the coefficient of friction μ and contact interaction. It comprises a spring and a damper arranged in parallel for both normal and tangential directions (Fig.2.32a). The viscoelastic sintering model is characterised by the elastic force in the spring, F^e, and the damping viscous components, F^V, which are arranged in parallel with the sintering force, F^{sint}, and the external load, F^{ext} (Fig.2.32b).
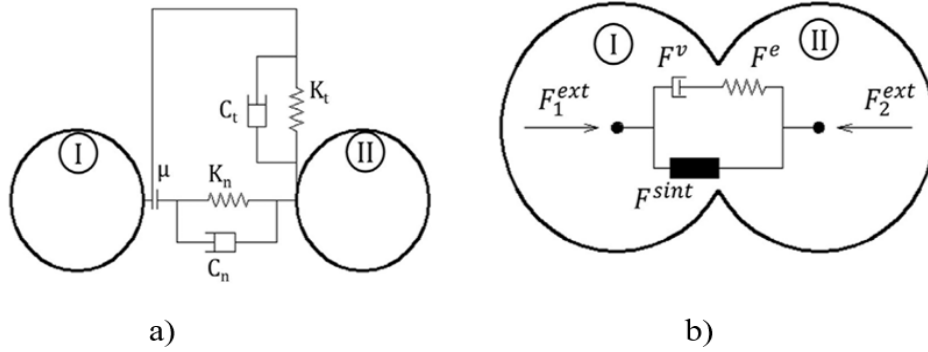

a)   b)

Fig.2.32. Model: a) Cohesive contact, b) Viscoelastic sintering (Žídek et al., 2021).

The Hertz-Mindlin contact model is appropriate for non-cohesive materials, but the JKR and DMT contact models are better applicable to adhesive materials (Zhu et al., 2022). The JKR model is applicable to soft particles, whereas the DMT model is suited for hard particles (Zhu et al., 2022). The cohesive forces acting on fine particles can originate from various factors, including van der Waals forces, electrostatic interactions, static-electric image charges in adjacent conductors, and, in high humidity conditions, surface tension in the menisci of adsorbed water at contact points. The work utilised surface energy to characterise the macroscopic cohesive properties of lunar soil simulant, encompassing both van der Waals forces and additional adhesion forces. The contact and damping forces can be derived as follows (Zhu et al., 2022):

$$F_n^{JKR} = \frac{4E^*}{3R^*}a^3 - 4\sqrt{\pi\gamma E^*}a^{3/2} \tag{2.44}$$

$$\delta_n = \frac{a^2}{R^*} - 4\sqrt{\pi\gamma a/E^*} \tag{2.45}$$

$$F_t^c = K_t\delta_t \tag{2.46}$$

$$F_d^n = 2\sqrt{\frac{5}{8}}\beta\sqrt{K_n m^*}v_n \tag{2.47}$$

$$F_d^t = 2\sqrt{\frac{5}{8}}\beta\sqrt{K_t m^*}v_t \tag{2.48}$$

Where:

a Contact radius

γ Surface energy

Newton's second rule of motion, while resultant moment is calculated (Zhu et al., 2022):

$$F_r = m\ddot{\delta} = F_n^c + F_t^c + F_n^d + F_t^d + mg \tag{2.49}$$

$$M_r = I\ddot{\theta} = R^* \cdot (F_t^c + F_t^d) - \mu_r F_n^c R^* \tag{2.50}$$

2.6.4 Inelastic contact model

The collision is completely inelastic, meaning all energy is instantaneously dissipated upon impact, resulting in the particle's velocity becoming zero (J. Thompson, 2023).

Linear spring-dashpot model: In contrast to the prior elastic contact model, which emphasised energy build up, the inelastic contact model was proposed to represent energy dissipation during plastic deformation between particles (Yeom et al., 2019). The predominant and intuitive framework for inelastic contact models is the linear spring-dashpot (LSD) model introduced by Walton, which is founded on the dashpot model utilised by Cundall and Strack. In the LSD model, the normal contact force is determined using the equation (Yeom et al., 2019):

$$F_n = -K_n \delta_n + \eta_n v_n \tag{2.51}$$

The tangential contact model is computed by employing a linear spring constrained by Coulomb's law of friction through the subsequent equation (Yeom et al., 2019):

$$F_t = \min\{\mu F_n, K_t \int v_t d_t + \eta_t v_t\} \tag{2.52}$$

The integral term, representing the linear spring component, signifies the incremental spring that accumulates energy from tangential motion and simulates elastic deformation owing to contact in the tangential direction (Yeom et al., 2019). The predominant contact models employed are the linear spring dashpot and the Hertz-Mindlin (non-linear) models (Coetzee, 2017). The equation for the linear spring dashpot contact model is given by (Coetzee, 2017):

$$F_c = F_l + F_d \tag{2.53}$$

Where:

F_l Linear spring component

F_d Linear damping component

The linear component can be decomposed into normal and tangential (Coetzee, 2017):

$$F_l^n = k_n \delta_n \tag{2.54}$$

$$F_{l_*}^t = (F_l^t)_o + k_t \Delta \delta_t \tag{2.55}$$

Where:

$(F_l^t)_o$ Shear force at the end of the previous time step

Coulomb-type frictional slip is permitted in the tangential direction, indicating that the previously calculated tangential force is evaluated against the following condition (Coetzee, 2017):

$$F_l^t = \begin{cases} F_{l_*}^t \text{ if } F_{l_*}^t \le \mu F_l^n \\ \mu F_l^n \text{ otherwise} \end{cases} \tag{2.56}$$

Upon collision of particle i with another particle j (or wall j), the contact force consists of two components, and the torques imparted to particle i during the impact (Xu et al., 2018):

$$m_i \frac{dv_i}{dt} = m_i g + \sum_{j=1}^{n_i} (F_{c,n,ij} + F_{c,t,ij}) \tag{2.57}$$

$$m_i \frac{d\omega_i}{dt} = \sum_{j=1}^{n_i} T_{c,ij} \tag{2.58}$$

Cundall and Strack devised the linear spring-dashpot model for calculating the contact force (Xu et al., 2018). The model delineates the two components of the contact force between two particles, i and j, or between a particles i and a wall j, as follows (Xu et al., 2018):

$$F_{c,n,ij} = -k_n \delta_{n,ij} - \eta_n v_{n,ij} \tag{2.59}$$

$$F_{c,t,ij} = -k_t \delta_{t,ij} - \eta_t v_{t,ij} \tag{2.60}$$

Furthermore, Ting and Corkum put forth various equations to determine the damping coefficient based on the known restitution coefficient. Upon fulfilment of the following condition (Xu et al., 2018):

$$|F_{c,t,ij}| > \mu_s |F_{c,n,ij}| \tag{2.61}$$

The tangential contact force is characterised by the Coulomb friction model, and only the tangential contact torque is computed by (Xu et al., 2018):

$$F_{c,t,ij} = -\mu_s |F_{c,n,ij}| \delta_{t,ij} / |\delta_{t,ij}| \tag{2.62}$$

$$T_{c,ij} = r \cdot n \times F_{c,t,ij} \tag{2.63}$$

Hysteretic model: The fundamental principle of the inelastic model is that it employs different spring constants during the loading, unloading, and reloading phases. Consequently, Walton and Braun formulated the linear contact model, known as the hysteretic model, which accounted for plastic deformation (Yeom et al., 2019). The correlation between force and displacement for the hysteretic model is depicted in fig.2.29d. This model use a partially latched spring force-displacement framework in the normal direction, while utilising the Mindlin and Deresiwicz theory approximation for the scenario of a constant normal force in the tangential direction. This model is constrained as it addresses plastic deformation solely in the normal direction. The contact force in the normal direction, based on the loading and unloading stages of the spring constant, is determined using the following equation (Yeom et al., 2019):

$$F_n = \begin{cases} -K_1 \delta_n, \dot{\delta}_n > 0 \\ \text{(loading)} \\ -K_2(\delta_n - \delta_{n0}), \dot{\delta}_n < 0 \\ \text{(unloading)} \end{cases} \tag{2.66}$$

Where:

K_1 Spring constant in the loading stage

K_2 Spring constant in the unloading stage

δ_{n0} Normal displacement when the unloading curve goes to zero (fig.2.31d)

The total normal force is the aggregate of the normal force component and the damping normal force component (Jiménez-Herrera et al., 2018):

$$F_n = -K_n \delta_n + C_n v_n^{\overrightarrow{rel}} \tag{2.67}$$

$$K_n \delta_n = - \begin{cases} K_1 \delta_n \text{ for loading } \left(K_1 \delta_n < K_2(\delta_n - \delta_0)\right) \\ -K_2(\delta_n - \delta_0) \text{ for unloading /reloading } (\delta_n > \delta_0), K_1 = 5R^* \min(Y^1, Y^2) \\ 0 \text{ for unloading } (\delta_n \leq \delta_0) \end{cases}$$

$$\tag{2.68}$$

Where:

Y^1 Yield strength of material one participant in the contact

Y^2 Yield strength of material two participant in the contact

δ_0 Residual overlap

The total tangential force is constrained by Coulomb's law of friction, resulting in (Jiménez-Herrera et al., 2018):

$$F_t = \min\left\{\mu_s F_n, K_t \delta_t + C_t \overrightarrow{v_t^{rel}}\right\} \tag{2.69}$$

Owing to the analogous mechanical properties of lunar soil simulant and lunar soil, the former has been employed as a substitute for conducting tests and simulations (Zhu et al., 2022). The characteristics of the lunar soil simulant were calibrated utilising the DEM to ensure precise simulation of the interactions between the rover wheel and the lunar soil simulant. Table 2.9 presents the calibrated DEM parameters utilised for the angle of repose (AoR) validation test, with the AoR findings illustrated in fig. 2.33.

Table 2.9. Material parameters obtained from experiments and literature (Zhu et al., 2022).

Parameter	Value
The particle diameter of lunar soil simulant [mm]	0.02–1
Bulk density of lunar soil simulant [kg/m^3]	1360
Young's modulus of lunar soil simulant [MPa]	10-75
Poisson's ratio of lunar soil simulant	0.2–0.31
Density of steel [kg/m^3]	7850
Young's modulus of steel [GPa]	184.9
Poisson's ratio of steel	0.293–0.305
Inner restitution coefficient of lunar soil simulant	0.3–0.9
Inner static friction coefficient of lunar soil simulant	0.2–0.7
Inner rolling friction coefficient of lunar soil simulant	0.0–0.5
Lunar soil simulant-steel coefficient of restitution	0.3–0.9
Lunar soil simulant-steel static friction coefficient	0.2–0.7
Lunar soil simulant-steel rolling friction coefficient	0.0–0.5
Surface energy for lunar soil simulant [J/m^2]	0.02–0.1
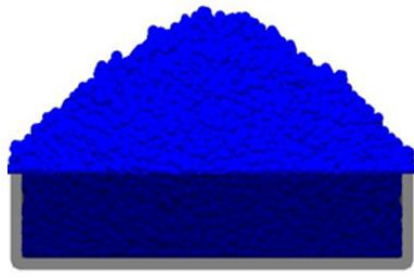
a) Simulation result   b) Experiment results

Fig.2.33. Comparison of the AoR between simulation and experiments (Zhu et al., 2022).

Calibration exercises aim to reconcile idealisation with reality by juxtaposing experimental outcomes with simulations performed across a meticulously selected parameter space. The Hertz-Mindlin contact model and rolling friction are employed in most DEM simulations. In 1971, Johnson-Kendall-Roberts (JKR) devised a model that expands upon the Hertz model by incorporating the influence of tensile pressures at the peripheries of the contact region to elucidate cohesive behaviour (Ajmal et al., 2020).

The angle-of-repose test is a standardised procedure employed to assess the bulk characteristics of simulated particles. A sensitivity study was performed on all significant parameters, including static friction, rolling friction, restitution coefficient, roundness, particle size distribution, and the quantity of ballast particles (Aela et al., 2022). When a particle is in a stable equilibrium on an incline, as depicted in fig.2.34 all forces acting onto the particle are in equilibrium.
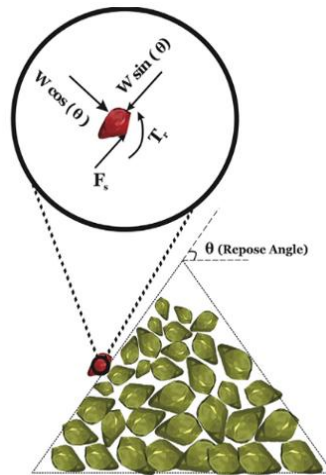

Fig.2.34. Shows contact forces exerted on particles at the slope (Aela et al., 2022).

As illustrated in fig.2.35, subsequent to filling the cylinder with approximately 160 ballast aggregates, the cylinder was elevated to facilitate the flow of the sample and its subsequent stabilisation.
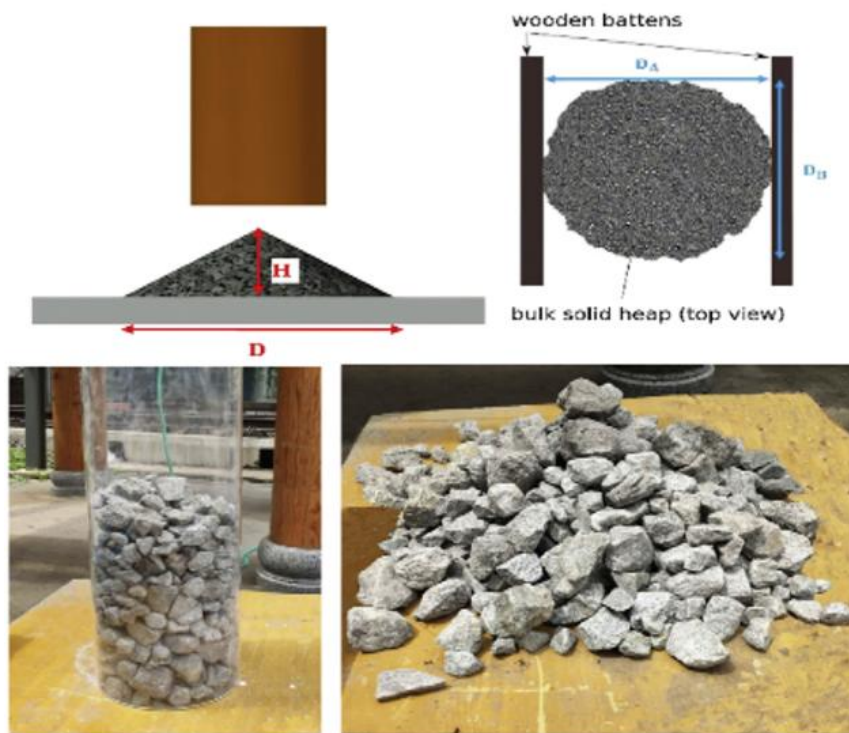
Fig.2.35. Photos of the angle of repose test (Aela et al., 2022).

Table.2.10 indicates that DEM modelling attempts persisted until the discrepancy between the AOR of the experiment and the simulation fell below 5%.

Table 2.10.Trials for the Calibration of DEM Models (Aela et al., 2022).

Variables		θ_1	θ_2	θ_{avg}	Shape
μ_s	μ_r				
0.75	0.2	40.22	40.88	40.55	
0.75	0.08	34.11	35.22	34.66	
0.9	0.1	39.40	39.71	39.55	
0.8	0.1	36.74	36.23	36.48	
0.85	0.15	38.42	37.78	38.1	

The "Rocky DEM" software use the wear coefficient (k value) as a parameter representing the volume/shear work ratio, which is contingent upon the qualities of the tested material. The specific morphology of particles (polyhedron, custom form, etc.) does not necessitate the use of the rolling resistance (RR) coefficient in Rocky DEM programme. The friction coefficient for non-spherical particles is the sum dynamic friction (DF) of the friction coefficients between rubber-sand and steel-sand. In the DEM simulation, it is infeasible to alter the bulk material parameters (density, Young's modulus, Poisson's ratio) as this would alter the soil properties (Katinas et al., 2021). Fig.2.36a) illustrates the meshing of samples and rubber-rimmed components using tetrahedral elements in the finite element method (FEM), while sand particles are represented by the DEM. The volume wear loss is realised through the inward displacement of triangulated surface vertices (Fig. 2.36c).

a) 3D abrasive wear simulation contains disc, pin and sand particles.

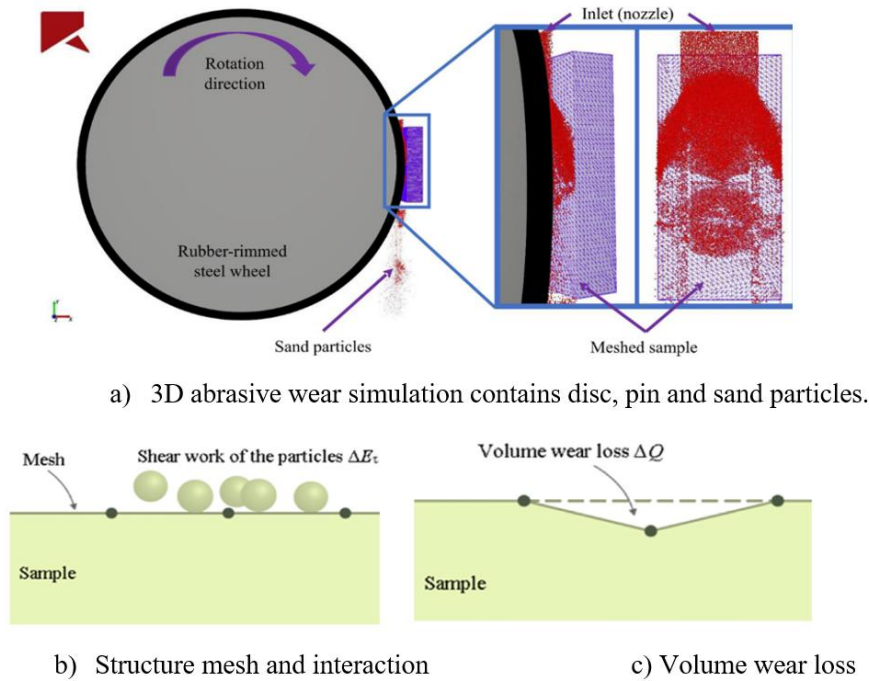b) Structure mesh and interaction   c) Volume wear loss

Fig.2.36. Abrasive wear by "Rocky DEM" (Katinas et al., 2021).

Abrasive wear resulting from the processing of solid particles is a significant cause of economic losses in the mining sector. The Archard wear model (Archard and Hirst, 1956) was integrated into the Rocky DEM software (Grasser et al., 2024). Archard's wear model is frequently utilised to analyse and replicate the abrasive wear of ductile materials. The wear volume exhibits a linear correlation with both the sliding force and the sliding distance between two surfaces. Diagram illustrating the interaction between an abrasive particle and the wear surface (Fig. 2.37).
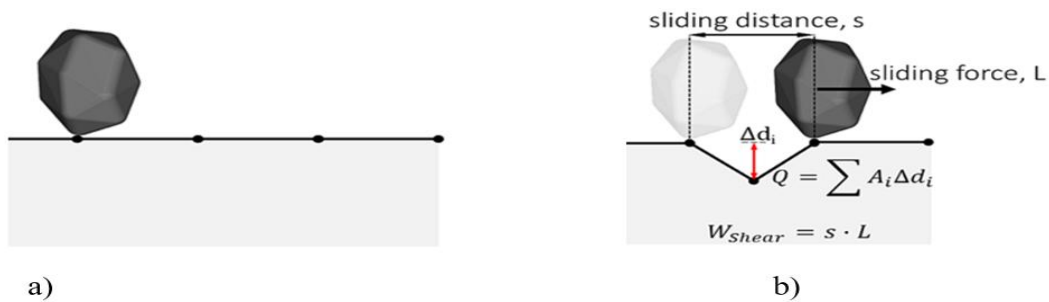

Fig.2.37. a) Prior to the contact, b) subsequent to the contact (Grasser et al., 2024).

The triangle size was 0.17 mm (shown in Fig.2.38 (d)-(f)) for both components of the composites, specifically the matrix and the inserts, as well as the monolithic specimens across all model configurations. To achieve a high-resolution wear topography, the triangle size was reduced to be smaller than the abrasive particles (Grasser et al., 2024). The reduced mesh size was unfeasible owing to computational limitations. Fig.2.39. Illustrates the distribution of cumulative passing percentages of abrasive particles relative to sieve size.
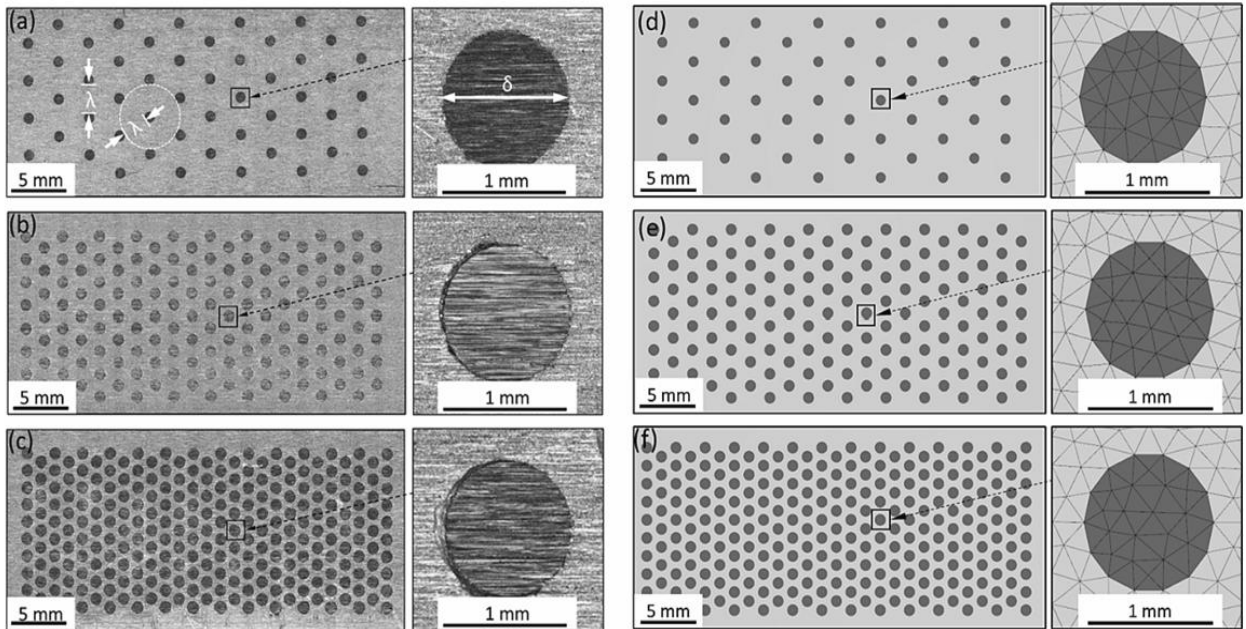
Fig.2.38. Experimented of (a) C8, (b) C23, and (c) C40, and simulated of (d) C8, (e) C23, and (f) C40.(Grasser et al., 2024).
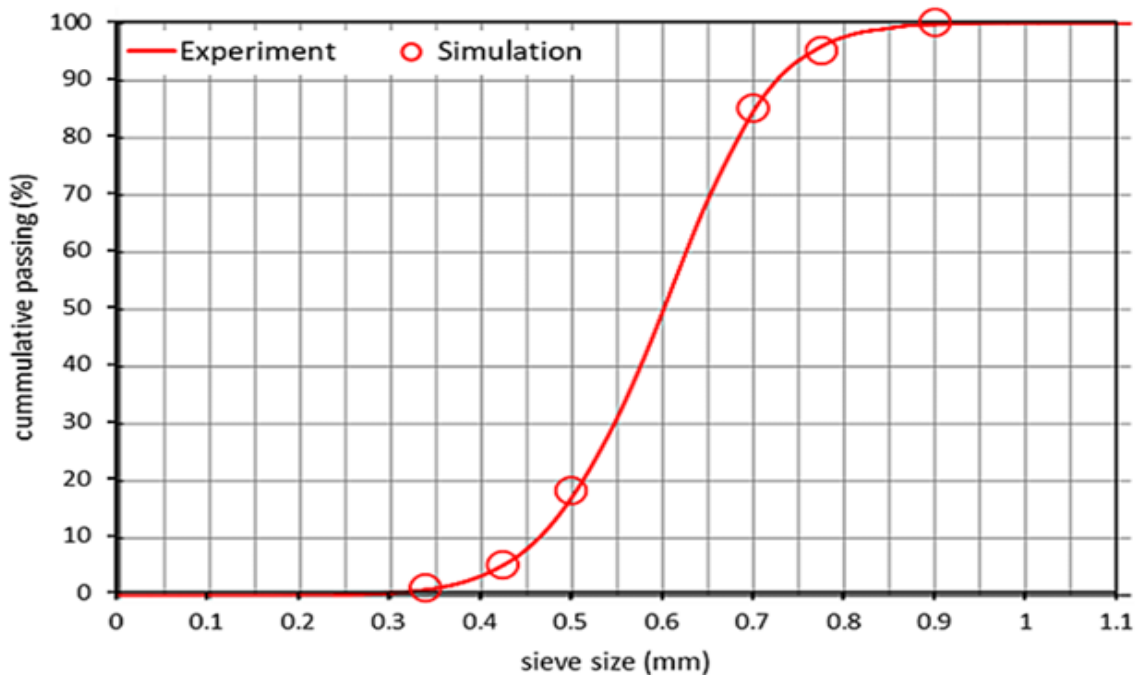

Fig.2.39. Illustrates of experimental and simulation (Grasser et al., 2024).

The DEM has been utilised to simulate abrasive wear on steel plates interacting with bulk substances. Employing a numerical method for wear prediction facilitates the reduction of

experimental prototype expenses while optimising equipment longevity (Perazzo et al., 2019). Fig.2.40. a) Particle in contact with the surface A_i of the mesh element, b) Displacement of the mesh element, c) Side view of the interconnection between nodes, and d) Top view of the wear representation. Fig.2.41 depiction of wear patterns produced in containing abrasive particles.
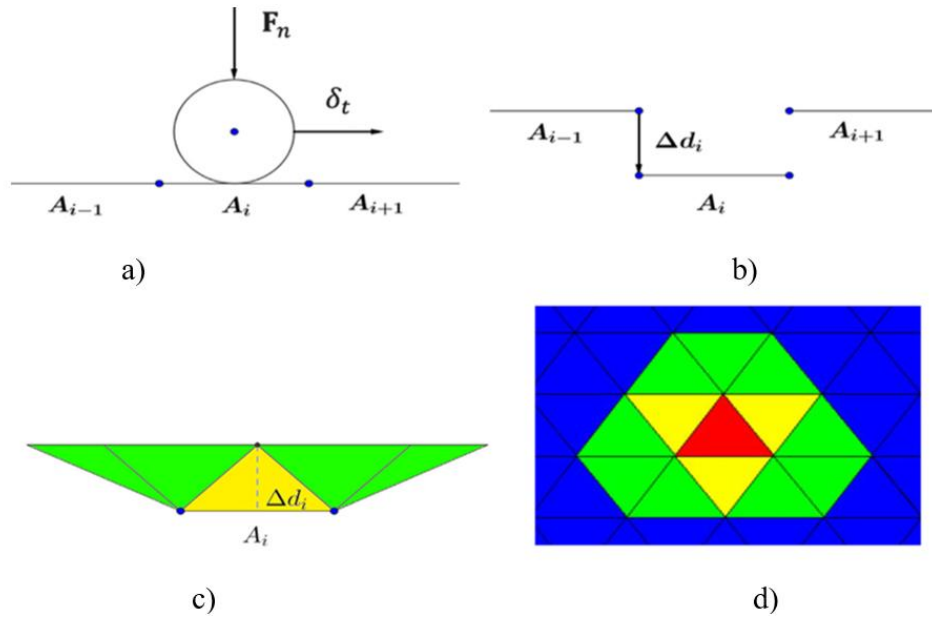

a)   b)

c)   d)

Fig.2.40. Representation of wear on a surface (Perazzo et al., 2019).

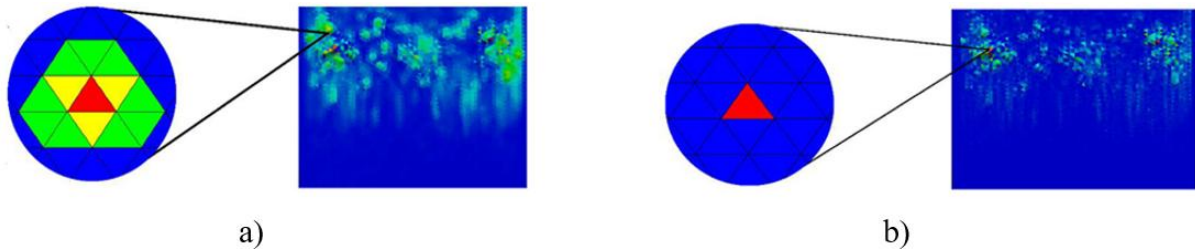a)   b)

Fig.2.41. Depiction of wear: a) detail of the region shaded by the depth of wear d_i, and b) detail of the area indicated by the impact I_i (Perazzo et al., 2019).

2.7   Summary of literature review

This chapter has presented an overview of abrasion wear processes and their relevance in sealing systems and rotating shafts. Abrasive particles can enter the sealing interface, leading to wear, leakage, and reduced component lifetime. On Earth, several technical solutions have been developed to reduce such problems, including advanced sealing designs, surface coatings, and filtration systems.

In extra-terrestrial environments, such as on Mars and the Moon, dust poses even greater challenges. The fine regolith particles are highly abrasive, electrostatically charged, and can infiltrate small gaps. Technical solutions need to ensure high dust resistance in extreme temperature and vacuum conditions. Sealing systems for planetary rovers and instruments must be carefully designed to operate reliably under these harsh conditions.

To better understand and simulate these issues, Discrete Element Method (DEM) modelling is widely used. DEM is a numerical technique that models the movement and interaction of individual particles. It is useful for predicting how regolith behaves and how it causes wear in mechanical systems.

Several studies have applied DEM to simulate lunar and Martian soil. However, most models use simplified particle shapes and material parameters. The literature shows that DEM modelling of lunar regolith is still in an early stage. There is a clear lack of DEM models that are based on real measurement data of lunar soil, such as actual particle size, shape, density, and mechanical properties. This limits the accuracy of current simulations and highlights the need for further experimental research to support model development, as I targeted in the research tasks (1.1.) Table 2.11 gives an overview of the historical progress of the research topic.

Table 2.11. Historical progress of the topic.

	Historical times	XX. century	Early XXI. century	2010s – 2020s	Up-to mid of 2020s
Abrasion detection	+	+			
Tribology – wear mechanism definitions		+			
Analytical wear models		+			
Numerical models		+	+	+	
Wear DEM models		+	+	+	+
Regolith experimental tests		+	+	+	+
Real measurement validated model results					Actual research

In the highlight of the above written, I selected the seal and rotating shaft materials and models based on the ESA 4000136800/21/NL/CBi research program that I took part. My goal was to study abrasion failure using a material sample taken from a lip seal. I tested this sample with selected lunar regolith as the abrasive medium, rubbing against a stainless-steel surface under laboratory conditions. The tests were carried out using a simple pin-on-disc tribotester. This setup is suitable for making relative comparisons under fixed conditions and for examining key features of the tribological system, such as changes in friction, wear behaviour, grain embedding, and surface roughness. From the on-line wear curves obtained in the tests—and following the models of Rabinowitz and Hutchings—I use the characteristic wear trends to validate my DEM models. Once the DEM models are validated, I can use them to run sensitivity tests within the seal/shaft/lunar regolith tribological system.

3. MATERIALS AND METHODS

3.1 Materials used for experiments

3.1.1 Rotary shaft material (stainless steel)

Cr and Ni alloy versions of steel were tested for abrasive purposes in ground and space conditions, mentioned in the public literatures (Bark et al., 2023), (Naser & Chehab, 2018), and (Roberts & Eiden, 2013).and former ESMATS papers (B. Arkwright, P. Buchele, 1999; Delgado & Handschuh, 2010; Dougherty, 2003; Galary, 2018; Grandy et al., 2019; Jandura, 2010; Kanji & Buratynsky, 2019; Lamotte et al., 2000; McClendon, 2011; Ng & Yung, 2010; Provedo et al., 2017) as shaft material. The following commercial steel grade was involved to the project as a shaft material due to mainly their austenitic structure, thus, low temperature applicability: 316 L (ASTM) or 1.4404 (EN). Table 3.1. Indicates the compositions among other stainless steel (SS) types. At (Outokumpu, 2020) further properties are available.

Table 3.1. Review of stainless-steel grades including the used 1.4404 (Outokumpu, 2020).

Outokumpu steel name	International steel no.		Typical composition, %							National steel designations, superseded by EN			
	EN	ASTM	C	N	Cr	Ni	Mo	Others	BS	DIN	NF	SS
4401	1.4401	316	0.04	–	17.2	10.2	2.1	–	316S31	1.4401	Z7 CND 17-11-022	2347
4404	1.4404	316L	0.02	–	17.2	10.1	2.1	–	316S11	1.4404	Z3 CND 17-11-02	2348
4436	1.4436	316	0.04	–	16.9	10.7	2.6	–	316S33	1.4436	Z7 CND 18-12-03	2343
4432	1.4432	316L	0.02	–	16.9	10.7	2.6	–	316S13	–	Z3 CND 17-12-03	2353
4406	1.4406	316LN	0.02	0.14	17.2	10.3	2.1	–	316S61	1.4406	Z3 CND 17-11 Az	–
4429	1.4429	S31653	0.02	0.14	17.3	12.5	2.6	–	316S63	1.4429	Z3 CND 17-12 Az	2375
4571	1.4571	316Ti	0.04	–	16.8	10.9	2.1	Ti	320S31	1.4571	Z6 CNDT 17-12	2350
4435	1.4435	316L	0.02	–	17.3	12.6	2.6	–	316S13	1.4435	Z3 CND 18-14-03	2353
4301	1.4301	304	0.04	–	18.1	8.3	–	–	304S31	1.4301	Z7 CN 18-09	2333
904L	1.4539	904L	0.01	–	20	25	4.3	1.5 Cu	904S13	1.4539	Z2 NCDU 25-20	2562
254 SMO®	1.4547	S31254	0.01	0.20	20	18	6.1	Cu	–	1.4547	–	2378
LDX 2101®	1.4162	S32101	0.03	0.22	21.5	1.5	0.3	5 Mn	–	–	–	–
2304	1.4362	S32304	0.02	0.10	23	4.8	0.3	–	–	1.4362	Z3 CN 23-04 Az	2327
2205	1.4462	S32205*	0.02	0.17	22	5.7	3.1	–	318S13	1.4462	Z3 CND 22-05 Az	2377

3.1.2 Lip seal material

According to the ESA project – as a reference sealing solution - a pure spring-loaded PTFE version (Table 3.2) was selected.

Table 3.2. Selected lip seals.

	Type	Material	Profile
Role: reference solution	Ro1-AS	natural PTFE	AS

For pin-on-disc laboratory tests (PoD) 8x8x8 mm cut PTFE cubes were applied. The natural PTFE semi-finished rods for further cutting were purchased from Quattroplast Ltd. Hungary, as Docaflon commercial grade. Materials datasheets are available:(Quattroplast, 2021).

3.1.3 Abrasive simulants

According to the project tasks and literature findings, two Lunar (LHS1 and LMS1) simulants were selected for the abrasion tests. The following are presented: LHS1: Lunar Highland Simulant (Table 3.3) and LMS1: Lunar Mare Simulant (Table 3.4).
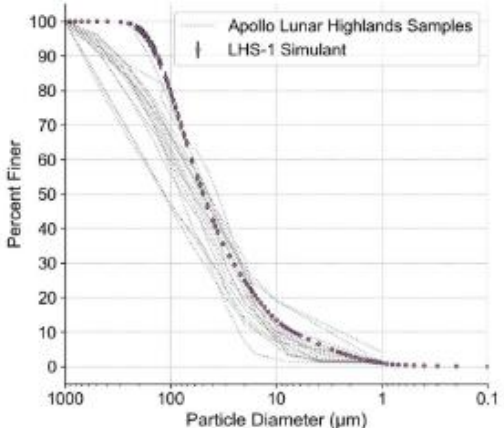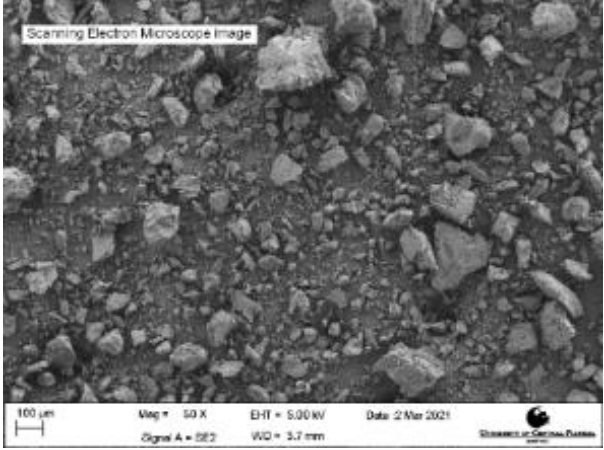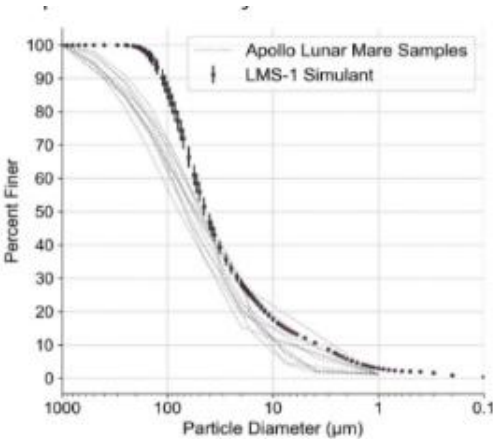
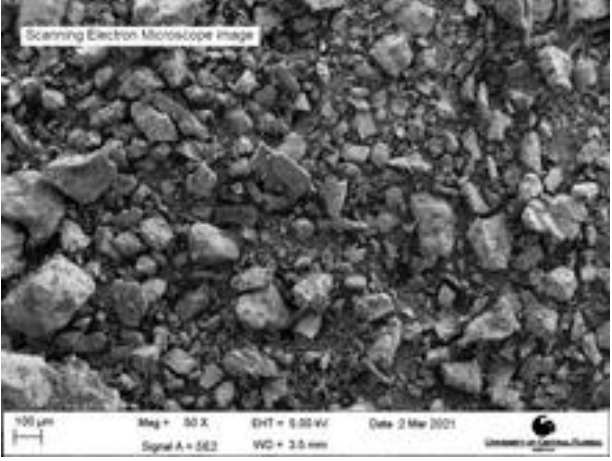Table 3.3. LHS1 simulant (exolithsimulants, 2020).

Producer: Exolith Lab https://exolithsimulants.com/	Country: USA	Reference material: Lunar highland average	https://exolithsimulants.com/collections/regolith-simulants/products/lhs-1-lunar-highlands-simulant
Composition:		Physical properties:	
74.4% Anorthosite (Greenspar)	0.3% Olivine	Bulk density: 1.30 g/cm³	Particle shape: Sub-angular to angular
24.7% Glass-rich basalt	0.2% Pyroxene		
0.4% Ilmenite			

Table 3.4. LMS1 simulant (exolithsimulants, 2020).

Producer: Exolith Lab https://exolithsimulants.com/	Country: USA	Reference material: Lunar Mare average	https://exolithsimulants.com/collections/regolith-simulants/products/lms-1-lunar-mare-simulant
Composition:		Physical properties:	
32.8% Pyroxene	11.1% Olivine	Bulk density: 1.56 g/cm^3	Particle shape: sub-rounded to sub-angular
32.0% Glass-rich basalt	4.3% Ilmenite		
19.8% Anorthosite			

3.1.4 Experimental abrasive pin-on-disc (PoD) system

Table 3.5. Summarized of test system features and configurations.

Parameters	Description		
Pin material	natural PTFE (Ln)	lip seal material	cut 8 x 8 x 8 mm
Rotating disc material	Stainless steel (SS)	1.4404 (SS)	Ø100 x 12 mm
Sliding speed (v)	0.1 m/s		
Normal load	PTFE pin/SS contact	0.2 MPa	
Ambient temperature	22 – 24 ℃		
Relative humidity (RH)	40 – 50%		
Start	In clean contact		
Sliding path	Covered with abrasive simulants		
Types of regolith applied	LHS1	LMS1	

The working abrasive PoD can be seen on Fig. 3.1.
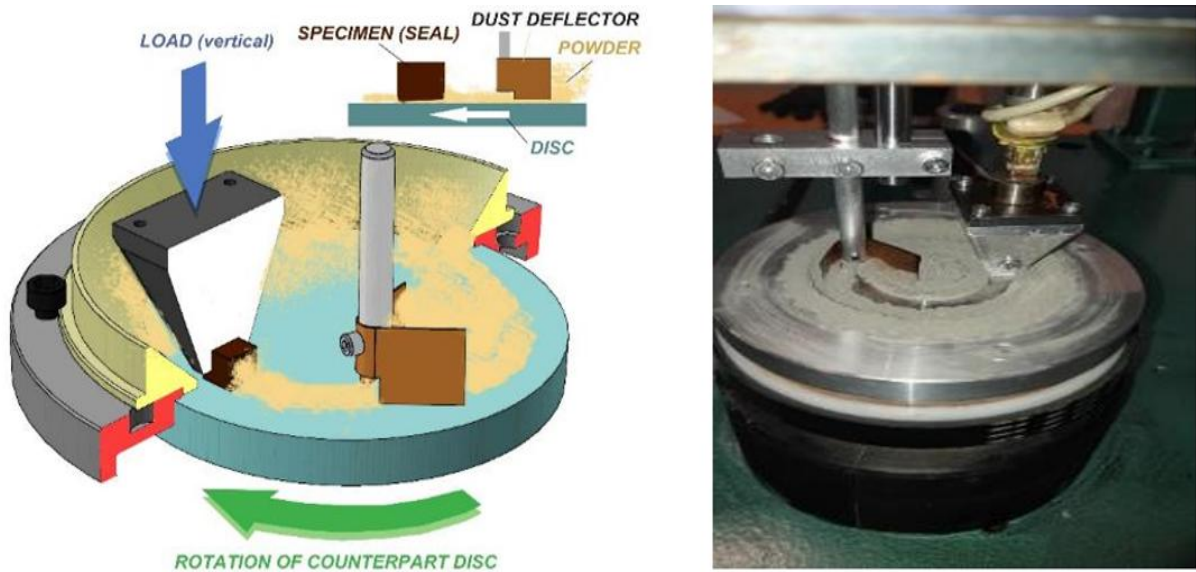
a) Schematic diagram of real machine   b) Photo of real machine

Fig.3.1. Pin-on-disc (PoD) abrasive system layout (Kalácska et al., 2024).

The rotating discs were composed of the introduced stainless steel, forming frictional pairs with pin components machined from natural PTFE. The combinations was subjected to testing under two different types of regolith. Each layout (sub-system) has 4 repeated runs (4 different sliding distance or Run time) with fresh pins on fresh metal disc surface.
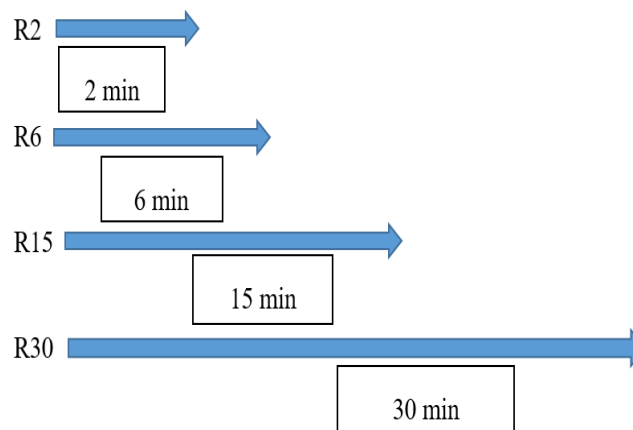

Fig.3.2. Describe four repeated runs.

The test records and data processing consistently used the following marking system, such as: Ln-SS-LHS1: Natural lip seal – stainless steel disc – LHS1 regolith; Ln-SS-LMS1: Natural lip seal – stainless steel disc – LMS1 regolith

3.1.5 Test procedure

The measurements can be divided into three main groups: pre-test measurements, on-line measurements, and post-test series measurements (Table 3.6.)

Table 3.6. Measured features.

Pre- test measurements	
Activity	Instruments
Weight measurement of samples (disc and pin)	Type of balance: HC5003VG
Measuring of surface roughness in 2D (disc)	Type of surface roughness tester: Mitutoyo SJ-201P
Surface photos with microscope, with 50 x magnification about the surfaces for visualization purposes	Type of microscope: Dino lite
Measuring of 2D and 3D topography, (disc and pin)	Data capture with Keyence VR 5200 3D optical microscope (white light interferometer)
SEM analyses, images in various magnifications about the surfaces (disc, pin)	Type of microscope: Zeiss EVo 40 and JEOL JSM-IT700HR
On-line measurements	
Friction force (for calculation of friction coefficient)	A pin-on-disc tester equipped with a Spider 8 data acquisition system.
Wear (vertical displacement of pin's holder head)	A pin-on-disc tester equipped with a Spider 8 data acquisition system.
Post-test measurements	
Weight measurement of samples (disc and pin)	Type of balance: HC5003VG
Surface photos with microscope, with 50x magnification about the surfaces for visualization purposes	Type of microscope: Dino lite
Measuring of 2D and 3D topography, (disc and pin) Dp calculation	Data capture with Keyence VR 5200 3D optical microscope (white light interferometer)
SEM analyses, images in various magnifications about the surfaces (disc, pin)	Type of microscope: Zeiss EVo 40 and JEOL JSM-IT700HR
EDX analyses of regolith particles embedded in sliding surfaces.	Type of EDS device: X-Act (Oxford Instruments) 10 mm^2, type of software: Aztec

The large database produced required detailed data processing and analysis, the methods of which were as follows: Calculation of weight loss for the test samples. Determination of changes in 2D and 3D roughness parameters. Visual evaluation of microscopic photos (50x magnification). Visual evaluation of SEM photos (500-2000x magnification). Elemental analyses of embedded regolith particles. Process analyses of on-line friction and wear curves. Calculation of Dp (degree of penetration) and determination of abrasive micro-mechanisms.

Development of a DEM model for the pin-on-disc system layout, with model settings and results demonstrated for MGS1 simulant in the Ln-SS contact.

3.1.6 Preparation of the test samples

Ultrasonic cleaning: The disc and polymer pin samples were cleaned using an ultrasonic cleaner (Fig.3.3 a). The type of cleaner used was Proclean 10.0MS. The cleaning liquid consisted of EM-300 Metallreiniger and osmosis-filtered water at a concentration of 1%. The disc was made of stainless steel (grade 1.4404). The polymer pin was composed of natural PTFE. Cleaning was carried out for 10 minutes at room temperature, without heating. After ultrasonic cleaning, the samples were rinsed with commercially available distilled water.
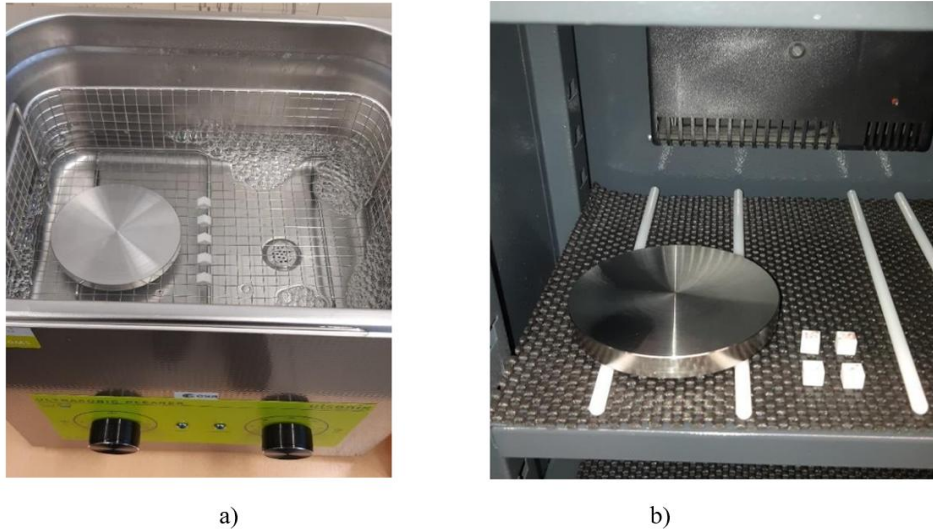

a)   b)

Fig.3.3. Represents: a) Ultrasonic cleaner, b) Drying chamber.

Drying of samples: Following cleaning, the disc and polymer blocks dried in a drying cabinet fig.3.3 b). The cabinet used was of type DRY30EA. The disc remained stainless steel 1.4404, identified as sample "1". The polymer pin material was natural PTFE. Drying was performed for 24 hours at a temperature between 22–24 °C and relative humidity (RH) of 30–50%.
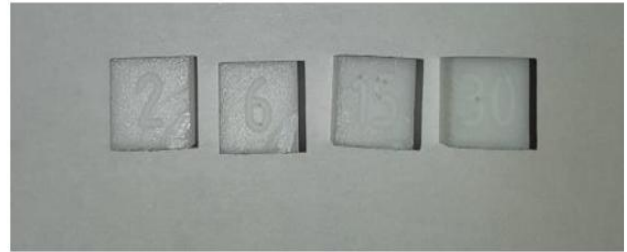
Weight measurement of samples: The weight of the disc and polymer blocks was measured using a precision balance (Fig. 3.4 a). Prior to measurement, identification numbers were milled onto the top surface of the polymer pins (Fig. 3.4 b) to indicate running times. The balance used was of type HC5003VG. Measurements were conducted at room temperature (22–24 °C) and relative humidity of 30–50%. A milling machine was used to engrave the ID numbers on the polymer pins.

Table 3.7. Explanation of running time or identification numbers.

No.	Descriptions	
No.2	2 minutes	R2
No.6	6 minutes	R6
No.15	15 minutes	R15
No.30	30 minutes	R30

Fig.3.4. Shows: a) Weight measurement b) Identified pin samples.

Surface roughness measurement: The surface roughness of the samples was assessed using a Mitutoyo SJ-201P surface roughness tester. The tester was operated via Mitutoyo software, with preselected settings configured according to the desired measurement parameters. The roughness of the stainless steel disc (material: 1.4404) was measured on both sides. Measurements were conducted at room temperature (22–24 °C), with ambient relative humidity maintained between 30–50%. After measurement, the software automatically generated a report file. Proper naming and saving of the report file were verified.

Table 3.8 shows the pre-test roughness of the discs used for LHS1 and LMS1 regoliths.

Table 3.8. Pre-test 2D surface parameters of the disc [µm].

	Disc no.1. for LHS1 tests		Disc no.2. for LMS1 tests	
	"Top" side	"Back" side	"Top" side	"Back" side
Ra	0.6	0.87	0.68	1.06
Ry	4.49	5.37	5.04	6.13
Rz	4.49	5.37	5.04	6.13
Rq	0.74	1.04	0.85	1.26

Surface imaging with microscope: To document the surface condition visually, microscopic photographs were taken at 50x magnification using a Dino-Lite digital microscope. The images served visualization purposes. The imaging was carried out at room temperature and 30–50% relative humidity. Care was taken to avoid contact with the working surfaces during handling. Before testing, images were captured of both the top and back sides of the stainless-steel discs, as well as the corresponding pin samples (R2, R6, R15, R30) for documentation (e.g. Fig.3.5). In fig.3.5a). Disc: surface finished by fine turning in a spiral pattern, thus the sliding model follows the real shaft-sealing contact, and no contamination detected (Fig.3.5a). Pin: clean and even surface, finished by milling (Fig.3.5b).
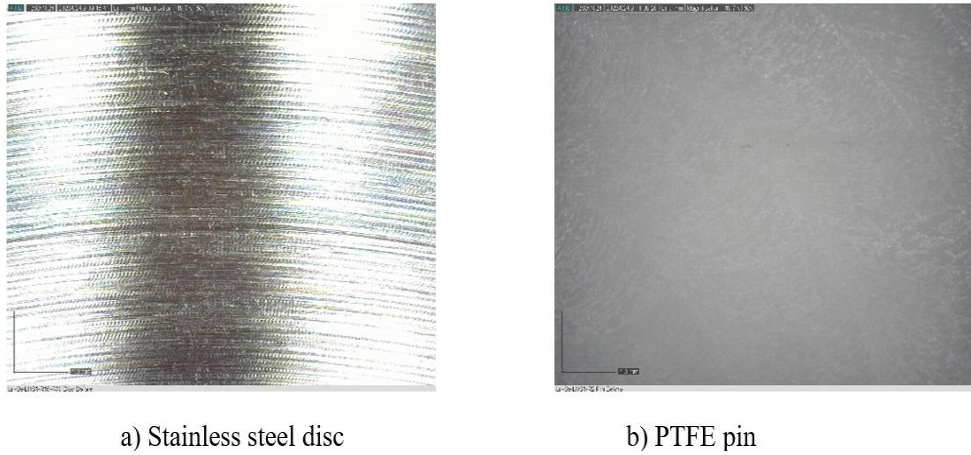

a) Stainless steel disc   b) PTFE pin

Fig.3.5. Pre-test condition.

3.2   Discrete Element Model

The Discrete Element Method (DEM) is a computational method that models the motion and interaction of granular materials. DEM was initially presented in two-dimensional (2D) format in 1979 by Cundall and Strack (J. A. Thompson et al., 2022). Since that time, DEM has been advanced by several researchers into a three-dimensional (3D) modelling technique.
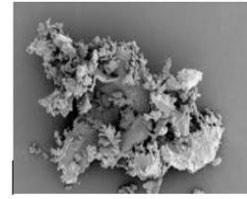
3.2.1   Granular materials

Granular material consists of discrete grains or particles (J. A. Thompson et al., 2022). These discrete particles may include coffee beans, peanuts, medicinal tablets, microscopic dust, or any intermediate substance. Granular materials are present in several natural occurrences, including rock stacks, gravel pile, and fine powders (Campello, 2018). Granular materials are prevalent in several human uses, ranging from piles of nuts and beans and mounds of sand to dense aggregates of significant importance in the pharmaceutical, chemical, food, and microelectronics sectors (Campello, 2018).

a) Coffee beans   b) Medicinal tablets   c) Microscopic dust

d) Rock stacks   e) Gravel piles   f) Fine powders

Fig.3.6. Depicts: Various granular materials (a, b, and c) and different particle size maybe same substance.

Charles-Augustin de Coulomb was among the initial scholars to examine granular materials comprehensively, as he articulated the rules of sliding friction concerning granular substances (J. A. Thompson et al., 2022).

Materials are often classified into two categories: continuous and discontinuous. Continuum mechanics examines several materials, including water, metals, rubbers, ceramics and etc. They all possess a singular essential characteristic. Their bulk is a singular entity, enabling the states of stress and strain to fluctuate continually within the material (J. A. Thompson et al., 2022).

Discontinuous or granular materials kind of material contrasts with the continuous materials, consisting of solids that are divided into discrete bulk, typically exhibiting diverse sizes, shapes, and qualities (J. A. Thompson et al., 2022).

Granular materials differ from solid and fluid materials in numerous respects (Campello, 2018). One of the most interesting features is that, depending upon the external forces applied, they may exhibit properties identical to solids, fluids, or even something entirely different solid or liquid, and frequently in a counter-intuitive manner (Campello, 2018). A primary distinction is that forces cannot transmit through a granular material without continuous excitation.

Studies indicate that particle morphology, size distribution, and bulk density substantially influence the mechanical properties of granular media (Zhu et al., 2022).

Brown and Richards categorise granular materials into three primary classifications (Campello, 2018):

- Powders: granular substances with particle sizes less than 100 μm.

- Granular solids: materials composed of grains with sizes ranging from 100 μm to 3 mm.

- Broken solids: granular substances with particles exceeding 3 mm in size.

At the molecular level, it is essential to address intermolecular forces, including Van der Waals forces and Brownian motion (J. A. Thompson et al., 2022).

Acquiring DEM characteristics between materials, such as coefficients of static and rolling friction among particles as well as between particles and equipment, is challenging by experimental methods (Zhu et al., 2022). Consequently, in numerous research, simulation parameters were established by virtual calibration or by angle of repose (AoR).

3.2.2 *Experimental angle of repose tests for both lunar highlands simulant (LHS-1) and lunar mare simulant (LMS-1)*

To experimentally measure the angle of repose, I utilised solely a hollow cylinder and a suitable simulant powder. In the experiment indicated in fig.3.7, an actual lifting hollow cylinder and a lunar soil simulant and lunar mare simulant were employed.

a) Hollow cylinder   b) Lunar highlands simulant (LHS-1)   c) Lunar mare simulant (LMS-1)

Fig.3.7. Indicated: equipment and lunar simulants powders.

Real LHS-1 powder was photographed utilising the newest camera following a downpour flow from lifting a hollow cylinder. Reference lines and angles were drawn on the images using the drawing programme Inkscape (Nakashima et al., 2011), and the coordinates of point B and the edge points A, C, and D were calculated as represented in fig.3.8. I measured the angles of the experiment on both the left and right sides from the bottom between the adjacent line and the inclined line.
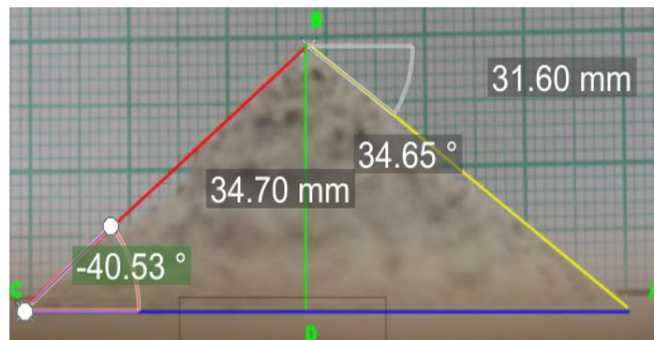

Fig.3.8. Assessing the angle of repose at the bottom of the powder heap (AOR$_{bottom}$) utilising Inkscape software.

Table 3.9. Indicate the analysis of the angle of repose at the base (AOR$_{bottom}$) for five experimental trials to calculate the mean angle.

	Angle of repose analysis in five experiment									
	Experiment 1		Experiment 2		Experiment 3		Experiment 4		Experiment 5	
Side	Left	Right	Left	Right	Left	Right	Left	Right	Left	Right
Angle (°)	46.79	42.30	40.53	34.65	39.40	46.33	36.52	37.16	37.75	39.29
average	$\alpha_1 = \dfrac{46.79 + 42.30}{2}$		$\alpha_2 = \dfrac{40.53 + 34.65}{2}$		$\alpha_3 = \dfrac{39.40 + 46.33}{2}$		$\alpha_4 = \dfrac{36.52 + 37.16}{2}$		$\alpha_5 = \dfrac{37.75 + 39.29}{2}$	
value (°)	$\alpha_1 = 44.54$		$\alpha_2 = 37.59$		$\alpha_3 = 42.865$		$\alpha_4 = 36.84$		$\alpha_5 = 38.62$	
average angle (°)	$\alpha_{ave} = \dfrac{(\alpha_1 + \alpha_2 + \alpha_3 + \alpha_4 + \alpha_5)}{5} = \dfrac{(44.54 + 37.59 + 42.865 + 36.84 + 38.62)}{5} = 40.091$									

All these symbols denote that Average angle of repose (α_{ave}): experimental one (α_1), experimental two (α_2), experimental three (α_3), experimental four (α_4), and experimental five (α_5).

3.2.3 Angle of repose determined by the discrete element method and calibration procedure for LHS-1

The physical and mechanical attributes utilised as input parameters for this study are shown in Table 3.10. Table 3.11 presents a compilation of the calculated surface energy values alongside the input coefficients of restitution and friction ranges from existing literature. Table 3.12 provides the Rocky DEM modelling and experimental results for inlet parameters. Rocky DEM software used to determine the contact characteristics of LHS-1, stainless steel, and natural PTFE in this study.

Table 3.10. Physical and Mechanical properties of materials.

Material properties	Lunar highland simulant (LHS-1)	Stainless steel (SS)	Nature PTFE (Pn)
Bulk density (g/cm^3)	1.30 (Dotson et al., 2024)	-	-
Density (g/cm^3)	1.60 (Quinteros et al., 2024)	7.95 (Kumar et al., 2020)	2.1 (Liu et al., 2019)
Young's modulus (GPa)	35 (Hou et al., 2019)	200 (Zolotarevskiy et al., 2022)	1.2(Liu et al., 2019)
Poisson's ratio	0.25 (Hou et al., 2019)	0.3 (Zolotarevskiy et al., 2022)	0.4 (Liu et al., 2019)

Table 3.11. Surface energy, coefficient of restitution and friction of materials.

Material interaction properties	Stainless steel	Nature PTFE	Lunar Highland Simulant (LHS-1)	Hollow cylinder
Static friction	0.2–0.7 (Zhu et al., 2022)	0.01-0.09 (Xiong et al., 2015)	0.45-0.998 (Dotson et al., 2024)	0 (Campello, 2018)
Dynamic friction	0.0–0.5 (Zhu et al., 2022)	0.0-0.05 (Xiong et al., 2015)	0.0- 0.7 (Dotson et al., 2024)	0 (Campello, 2018)
Restitution coefficient	0.3–0.9 (Zhu et al., 2022)	0.3-0.9 (Žídek et al., 2021)	0.3-0.9 (Zhu et al., 2022)	0 (Campello, 2018)
Surface energy for lunar regolith simulant [mJ/m^2]			0.01–0.1	

Table 3.12. Rocky DEM modelling and experiments in relation to inlet parameters.

Input parameters	values
Upward cylinder lifting velocity (m/s)	0.008-0.1 (Roessler & Katterfeld, 2019)
Gravity (m/s^2)	9.81
Pressure	Air pressure
Temperature	Room temperature

To determine the angle of repose using the discrete element approach in Rocky DEM programme, I must first select a suitable contact model. The chosen contact model is performed not only to compute the angle of repose but also to assess three body abrasive wear analysis. I shall explain the chosen contact model in detail in section 3.2.4 below.

3.2.4   Contact models

The discrete element contains two primary components: powders and structures, which interact with one another. In my dissertation, the particles (powders) are distinct and are attributed the characteristics of a certain simulant substance. The structures, including natural PTFE and stainless steel, with which powders can interact, serve as walls.

In section 2.6 of the literature review, I provide a detailed explanation of several contact models. Studies predominantly employed the linear spring dashpot model and the Hertz-Mindlin model. I choose the Hertz-Mindlin + JKR model for my dissertation. Researchers excluded this model due to computational duration and particle dimensions. Most studies now focus on mesoscopic and macroscopic particles due to limitations in computational capacity. However, I conduct micro-scale particle analysis.

The majority of researchers employed spherical (regular) particle shapes, others exploited irregular particle shapes, and a minority adopted polyhedral particle shapes, which encompass both regular and irregular forms. I selected polyhedral particle shapes for my dissertation.

In this dissertation, I choose the soft particle model, wherein applying of forces creates overlap. This is illustrated in the 2D instance, Fig. 3.9, for a) polyhedral particle i and polyhedral particle j interaction, and b) polyhedral particle i and the wall interaction. In addition to these, fig. 3.10 illustrates all forces acting on the particles or walls during interaction, including spring forces (F_s), and damping forces (F_d) present in both the normal direction (n) and the tangential direction (t). The Force of Johnson-Kendall-Roberts (F_{jkr}) is applied in the normal direction. Meanwhile, the friction forces (F_f) may be static friction or sliding friction is applied tangential direction. There is no 2D polyhedral shape; I imagined a 2D polyhedral form in order to clarify the idea.

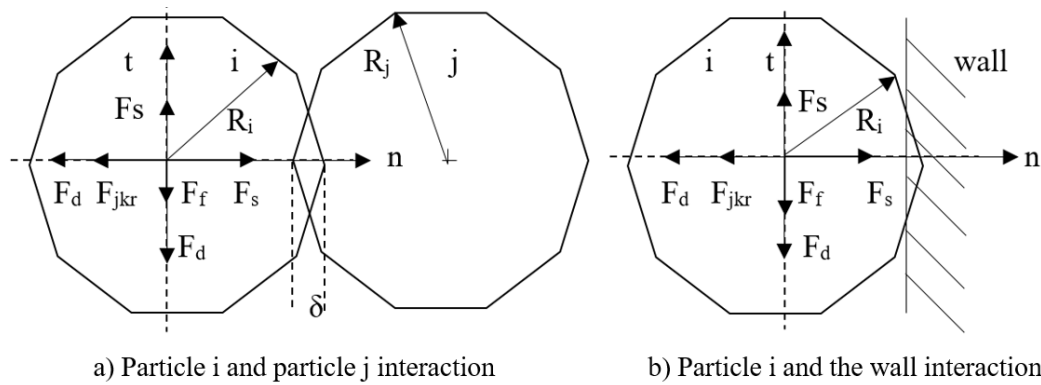a) Particle i and particle j interaction   b) Particle i and the wall interaction

Fig.3.9. Illustrates all forces acting particle or wall, and their directions.

Fig 3.10. Demonstrates the spring force, damping force, and slider friction force employing imaginary symbols in both the normal and tangential directions, incorporating the adhesive force (F_{jkr}) in the normal direction and static friction force in the tangential direction for both a) particle-to-particle, and b) particle-to-wall interactions.

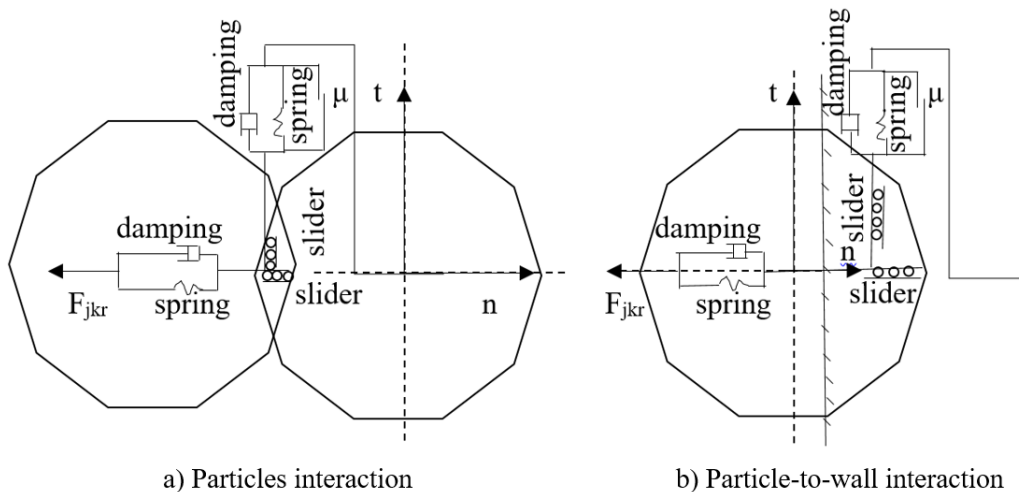a) Particles interaction   b) Particle-to-wall interaction

Fig.3.10. Demonstration of imaginary symbols in Hertz-Mindlin + JKR contact model.

In Fig.3.9, the overlapping contact area between particles or between a particle and a wall is depicted as circular, with the radius of the overlapping circular contact area determined as follows:

$$\delta_n = \frac{a^2}{R^*} - 4\sqrt{\pi\gamma a/E^*} \tag{3.1}$$

The polyhedral particle exhibits numerous overlapping areas during interactions between particles or between the particle and the wall due to its shape, as shown in fig 3.11 below. As a result, the overlapped contact radius has been established as follows:

$$\delta_{n,j} = \frac{a_j^2}{R^*} - 4\sqrt{\pi\gamma a_j/E^*} \tag{3.2}$$
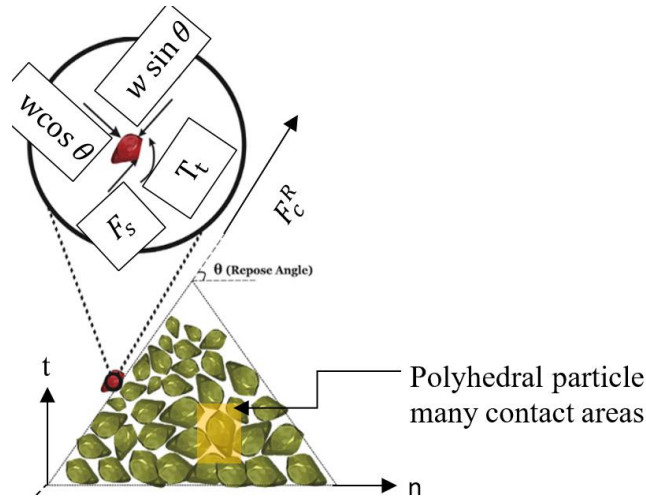
Where:

    j Number of contact point, j = 1,2 ...

Fig.3.11. Demonstrate the polyhedral particle exhibiting several contact surfaces with other polyhedral particles and the wall.

The Hertz-Mindlin + JKR contact models express the summation of contact forces in the normal direction as follows:

$$F_c^n = F_{n,s} - F_{n,d} - F_{n,jkr} \tag{3.3}$$

Where:

    $F_{n,s}$ Normal contact force of Hertzian spring, $F_{n,s} = \frac{4E^*a^3}{3R^*}$

    $F_{n,d}$ Normal contact force of Hertzian dashpot, $F_{n,d} = \frac{2\sqrt{5}lne\sqrt{m^*E^*R^*}^{1/4}}{\sqrt{3ln_e^2+3\pi^2}}\dot{\delta}_n\delta_n^{1/4}$

    $F_{n,jkr}$ Normal contact force of adhesive use JKR model, $F_{n,jkr} = \sqrt{8\pi\gamma E^*a^3}$

The Hertz-Mindlin + JKR contact models describe the whole summation of contact forces in the normal direction when used on polyhedral particle:

$$F_{tc}^n = k_s \sum_{j=1}^m a_j^3 - k_d \sum_{j=1}^m \delta_{n,j}^{1/4} - k_{jkr} \sum_{j=1}^m a_j^{3/2} \tag{3.4}$$

Where:

$$k_s = \frac{4E^*}{3R^*}$$

$$k_d = \frac{2lne\sqrt{m^*E^*}R^{*1/4}}{\sqrt{3ln_e^2 + 3\pi^2}}\dot{\delta}_n$$

$$k_{jkr} = \sqrt{8\pi\gamma E^*}$$

m Total number of contact points

The identical overlap or contact surface area holds to the entire system; hence, Equation 3.4 will be simplified:

$$F_{Totc}^n = mk_s a^3 - mk_d\delta_n^{1/4} - mk_{jkr}a^{3/2} \qquad (3.5)$$

Where:

F_{Totc}^n Total normal contact force

The Hertz-Mindlin + JKR contact models describe the summation of tangential contact forces outlined below:

$$F_c^t = F_{t,s} - F_{t,d} - F_{t,f} \qquad (3.6)$$

Where:

$F_{t,s}$ Tangential contact force of Hertzian spring

$F_{t,d}$ Tangential contact force of Hertzian dashpot

$F_{t,f}$ Friction force in tangential direction

Equation 3.6 can be reformulated within the Mindlin-Deresiewicz model for tangential force:

$$F_{Totc}^t = -\mu F_{Totc}^n\left(1 - \zeta^{\frac{3}{2}}\right)\frac{\delta_t}{|\delta_t|} + \eta_t\sqrt{\frac{6\mu m^* F_{Totc}^n}{\delta_{t,max}}}\zeta^{\frac{1}{4}}\dot{\delta}_t \qquad (3.7)$$

Where:

F_{Totc}^t Total tangential contact force

δ_t Tangential overlap between particles (Yang et al., 2024), $\delta_t = \left[\frac{9\pi\gamma R^{*2}}{2E^*} \times \left(\frac{3}{4} - \frac{1}{\sqrt{2}}\right)\right]^{\frac{1}{3}}$

δ_n Normal overlap between same particles

$\zeta = 1 - \frac{min(|\delta_t|, \delta_{t,max})}{\delta_{t,max}}$

$\eta_t = -\frac{lne}{\sqrt{ln_e^2 + \pi^2}}$

μ Coefficient of friction and $\mu = \begin{cases} \mu_s \text{ if no sliding takes place at the contact} \\ \mu_d \text{ if sliding does take place at the contact} \end{cases}$

μ_s Static friction coefficient

μ_d Dynamic friction coefficient

$\delta_{t,max}$ Maximum relative tangential displacement, $\delta_{t,max} = \mu\left(\frac{1-\nu_1}{2-\nu_1} + \frac{1-\nu_2}{2-\nu_2}\right)^{-1}\delta_n$

Resultant contact force is determined by the following formula:

$$F_c^R = F_{Totc}^n + F_{Totc}^t \tag{3.8}$$

Magnitude of the resultant contact force is calculated:

$$F_c^R = \sqrt{(F_{Totc}^n)^2 + (F_{Totc}^t)^2} \tag{3.9}$$

Where:

F_c^R Resultant contact force

Newton's second law of motion states that at any given time t, the equations governing the translational and rotational motion of particles are articulated as follows:

$$m\frac{dv}{dt} = \sum_{j=1}^{m}(F_{n,s} + F_{n,d} + F_{n,jkr} + F_{t,s} + F_{t,d} + F_{t,f}) + mg \tag{3.10}$$

$$m\frac{d\omega}{dt} = \sum_{j=1}^{m}(T_t) \tag{3.11}$$

Where:

T_t Torque from tangential forces and $T_t = R_n^* \times (F_{t,s} + F_{t,d} + F_{t,f})$

R_n^* Equivalent radius between particles or particle to wall in the normal direction

To ascertain the time step for equations 3.10 and 3.11, two methodologies exist in computational models: implicit and explicit time stepping strategies. Implicit refers to static analysis, while explicit pertains to dynamic analysis. I pick explicit procedures because my dissertation focuses on abrasive wear.

The critical time step Δt^{crit} was determined using the equation put out by Thornton and Randall (Ai et al., 2011):

$$\Delta t^{crit} = \frac{\pi r_{min}}{0.163v + 0.8766}\sqrt{\frac{\rho}{G}} \tag{3.12}$$

Where:

Δt^{crit} Critical time step

r_{min} Minimum particle radius

ρ Density of particle

G Shear modulus of particle

v Poisson's ratio

A time step approximately 10% of the critical time step Δt^{crit} of the system was utilised in all calculations unless otherwise specified (Ai et al., 2011):

$$\Delta t = 0.1\Delta t^{crit} \tag{3.13}$$

Where:

Δt Time step

My dissertation largely focuses on the interactions between the particle and the structural elements. Therefore, I will briefly explain the interaction or overlap between particle and structure.

Voronoi tessellation was utilised to model material microstructure and produce rough surfaces (Singh et al., 2019). Grain morphology seen experimentally was utilised to predict material

microstructure through Voronoi tessellations. Voronoi grains were subsequently discretized with constant strain triangular finite elements (Singh et al., 2019). Surface roughness was produced by utilising the tessellation technique and employing the Ra level derived from surface profilometry measurements.
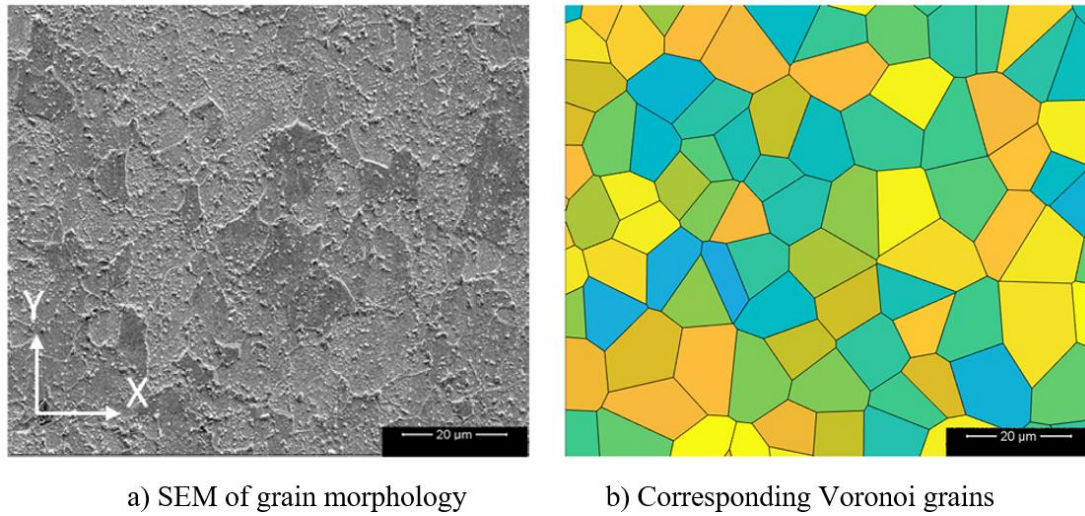

| a) SEM of grain morphology | b) Corresponding Voronoi grains |

Fig.3.12. Depicting: a) SEM image grain morphology, and b) Voronoi grains created numerically (Singh et al., 2019).

To generate a Voronoi tessellation, seed points are randomly allocated within a domain, then the area is partitioned into cells surrounding each point (Leonard et al., 2013).
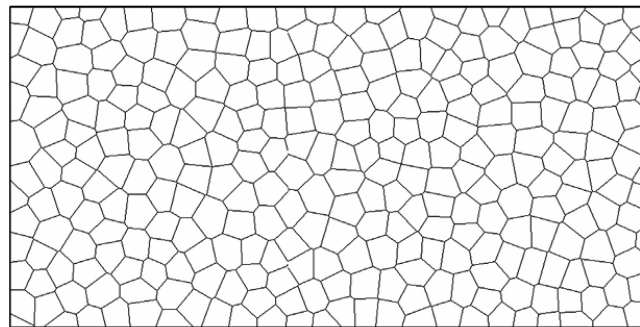
Fig.3.13. Voronoi mesh without colour (Leonard et al., 2013).

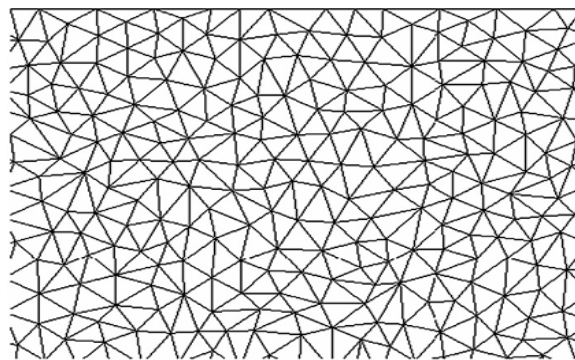The Voronoi mesh within a domain can be discretized utilising Delaunay triangular Mesh.

Fig.3.14. Delaunay triangular mesh (Leonard et al., 2013).

Consequently, specific attention must be directed towards the interaction between the mesh elements and the particles. The overlap between particle and triangular element is calculated (J. Thompson, 2023):

$$\delta = d_{p,e} - r \qquad (3.14)$$

Where:

$d_{p,e}$ Distance between the particle and the element

r Particle radius

For a structural element, the overlap value is subsequently doubled to establish an effective overlap, d, for the collision (J. Thompson, 2023). This renders the collision analogous to a single particle striking an unmoveable particle of identical dimensions, which is utilised for the force calculation as previously demonstrated in Equation 3.1 (J. Thompson, 2023).

3.3 Abrasion wear model in DEM

The initial wear model appropriate for application in the Discrete Element Method is Archard's abrasion model, as presented in Equation 3.15.

$$V = KW\,L/H \qquad (3.15)$$

A crucial variable in this equation is the sliding distance value, L. This amount (the distance a surface traverses along another) necessitates understanding the final state of the system, specifically at the conclusion of the current time step. In a simulation scenario, the distance is not predetermined; thus, a projected sliding distance is computed for each time step. This is accomplished utilising the resultant velocity, v_R, in relation to the affected element and the time step value, Δt.

Given that all other variables will be known to the simulation, Archard's equation can be expressed as described in Equation 3.16.

$$V = k\,\frac{F_c^R\,v_R\,\Delta t}{H} \qquad (3.16)$$

Where:

v_R Resultant velocity, $v_R = \sqrt{\dot{\delta}_t^2 + \dot{\delta}_n^2} = \sqrt{v_t^2 + v_n^2}$

4. RESULTS AND DISCUSSION

4.1 Pin-on-disc abrasive measurements with LHS1 regolith

This chapter details the experimental results of a tribological investigation conducted on a stainless steel (SS) and natural Polytetrafluoroethylene (PTFE) material pair. The study simulates the abrasive environment created by LHS1, a lunar regolith simulant, to understand its impact on these materials. Such analysis is crucial for the design and longevity of mechanical components used in space exploration missions, particularly for applications involving contact with regolith. A modified pin-on-disc tribometer (chapter 4.1.4) was utilized to analyse friction, wear, and surface transformations under controlled laboratory conditions. The primary objective was to characterize the wear mechanisms on both the steel disc and the PTFE pin. To achieve this, a suite of advanced microscopic and spectroscopic techniques was employed, including Scanning Electron Microscopy (SEM), Energy Dispersive X-ray (EDX) analysis, and 3D surface topography. This comprehensive approach provides a detailed understanding of the tribological behaviour of this material pairing in a simulated extra-terrestrial environment.

4.1.1 Friction and wear behaviour

The tribological behaviour of the system was characterized by analysing the coefficient of friction and the vertical displacement of the pin ("wear" curves). Both sets of data showed excellent reproducibility across the four test durations (R2, R6, R15, and R30), as seen in Fig. 4.1., and 4.2. Fig. 4.1 displays the coefficient of friction graphs reflecting the interaction among Ln-SS-LHS1 materials at a sliding speed (v) of 0.1 m/s and a normal pressure (p) of 0.2 MPa.
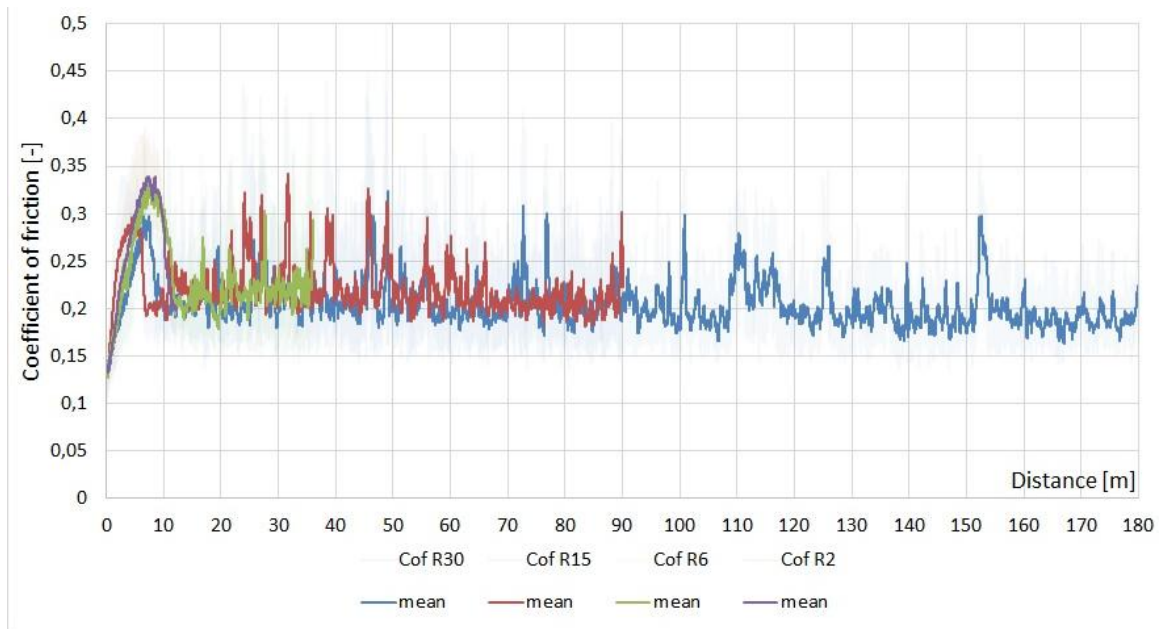

Fig.4.1. Summary of friction results (Ln-SS-LHS1-R2-R6-R15-R30).

The coefficient of friction is an abrasive friction number characteristic of an open three-body abrasive mechanism. The tests began with a distinct run-in phase over the first 8-10 meters of sliding, where the pure PTFE/steel adhesive contact resulted in a peak friction coefficient of approximately 0.35. After this initial phase, the LHS1 regolith particles entered the contact zone. This marked a transition from adhesion-dominated friction to a lower, more stable sliding

resistance (~0.2) governed by a Berthier-Eleőd three-body abrasion mechanism. This mechanism involves particles becoming embedded in the softer PTFE surface, rolling between the surfaces, adhering to each other, and occasionally breaking up or congesting to form larger blocks. This dynamic balance was evidenced by recurring friction peaks every 10 meters of sliding. A strong sound effect was also noted during the abrasive sliding process in all four test series. Fig. 4.2 depicts the wear curves or displacement (D_P) in millimetres (mm) resulting from the interaction of Ln-SS-LHS1 materials under a sliding speed (v) of 0.1 m/s and a normal pressure (p) of 0.2 MPa.
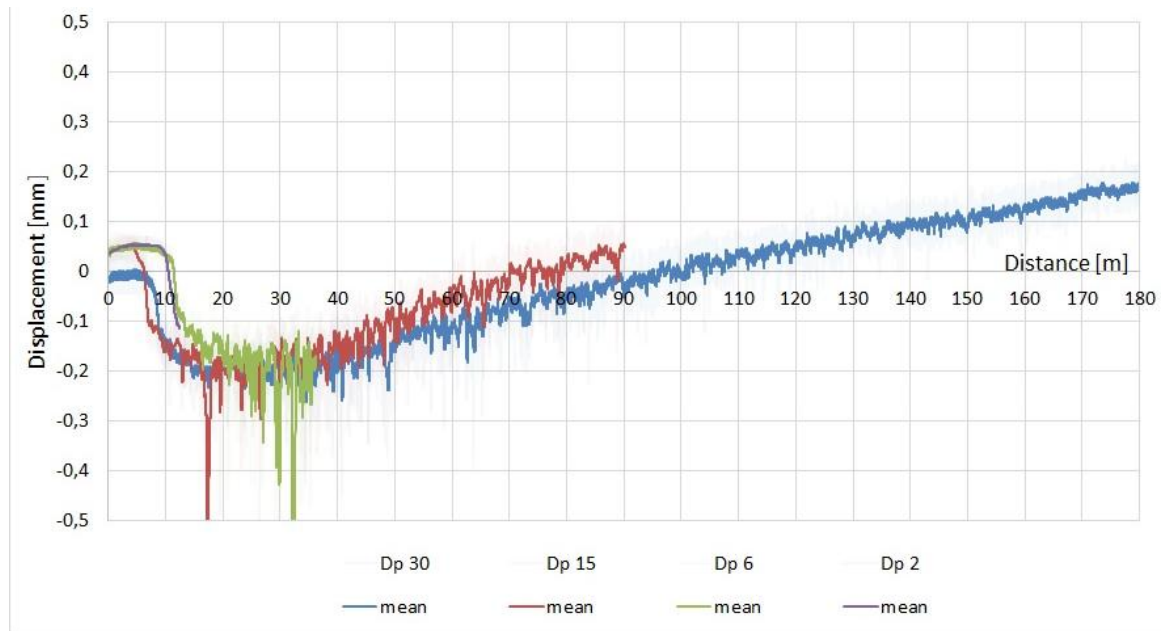

Fig.4.2. "Wear" curves showing the vertical displacement of the pin holder.

The vertical displacement curves provide further insight into the three-body dynamic. After the initial 8-10 meters of adhesive sliding, the ingress of regolith into the contact zone physically lifted the pin holder, resulting in a negative wear reading between 10 and 50 meters of sliding. Extreme peaks, with displacement down to -0.5 mm, indicate the accumulation of larger particle agglomerates in the contact zone. After approximately 50-60 meters, the system stabilized, and the continuous micro-cutting of the PTFE pin by the regolith grains led to a more classic, linear abrasive wear trend. The total vertical displacement, which is a combined result of deformation, wear, particle dynamics, and thermal expansion, reached up to 0.1 mm.

The trend of weight measurements of the pins gave the same trend (Table 4.1):

Table 4.1. Weight change of the pins.

R	R2	R6	R15	R30
Δm of PTFE pins [g]*	0.011	0.009	-0.002	-0.016

4.1.2   Surface characterization

Post-test analysis using microscopy and spectroscopy was performed to correlate the friction and wear data with physical changes on the surfaces of the disc and pin. SEM analysis was
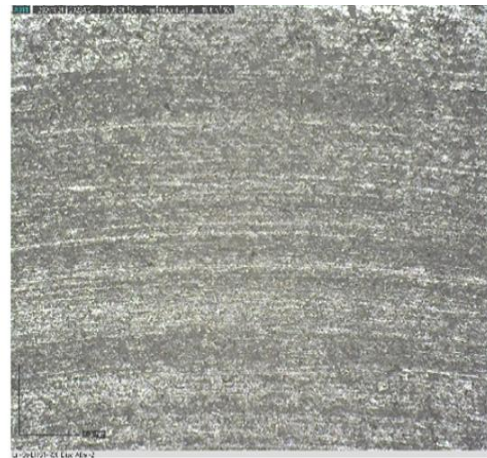
conducted using Zeiss EVo 40 and JEOL JSM-IT700HR microscopes, while EDX was performed with an X-Act (Oxford Instruments) device. To prevent electrical charging, the PTFE samples were coated with a thin gold film via sputtering before analysis.

Disc surface analysis: Macroscopic and microscopic examination revealed a clear progression of wear on the stainless-steel disc (Fig.4.3 – 4.4).

- R2 Run: The initial stage of abrasive wear was observed. The original micro-geometry of the metal surface began to show damage, with the first signs of particle embedment and adhered polymer as describe in fig.4.3a) SEM images confirmed that while original polishing grooves were still visible, the surface was damaged by scratches and inclusions from embedded particles.

- R6 Run: Damage on the wear track became more uneven, suggesting a transition from the running-in phase to a steady-state abrasive wear, with some areas showing locally increased damage. The density of these damaged areas increased, and it was noted that the majority of embedded particles were smaller than the D10 size of the LHS1 powder.

- R15 Run: The proportion of the damaged surface grew, forming distinct parallel bands that were evenly distributed around the circular wear track. The density of damage continued to increase with the abrasion time.

- R30 Run: Surface damage intensified further. The parallel bands observed in the R15 run became wider, although the entire contact area was still not completely covered by embedded particles and adhered PTFE as show in fig.4.3b and 4.4 a-d). SEM images showed an increase in the number of bumps on the surface.
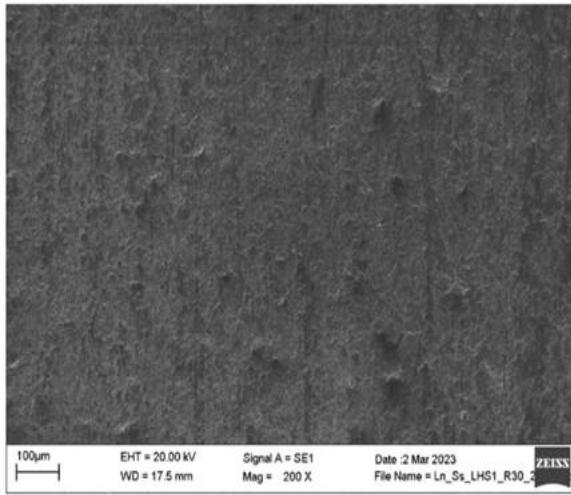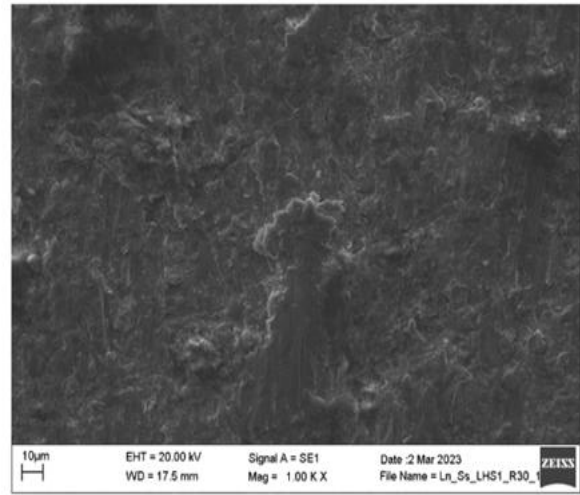

a) Ln-SS-LHS1-R2 disc (top side, 50x)   b) Ln-SS-LHS1-R30 disc (bottom side, 50x)
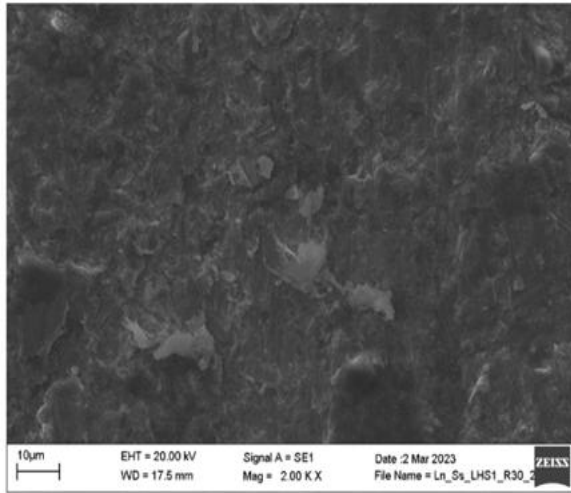
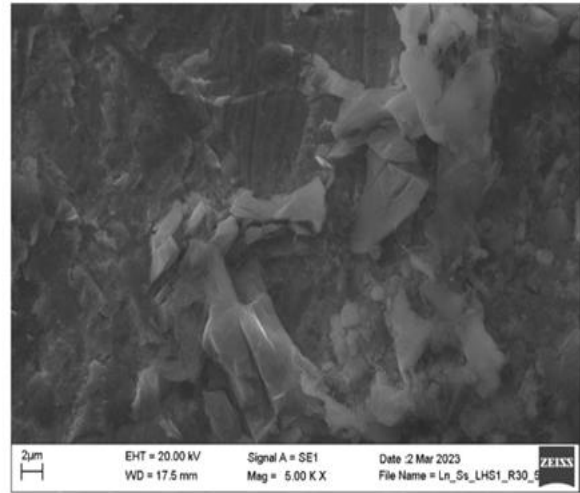Fig.4.3. Top-surface of the worn disc.

a) 200X

b) 1000X

c) 2000X

d) 5000X

Fig.4.4. SEM image of the R30 worn disc surface at high different magnification, showing increased damage density and embedded particles.

Elemental analysis (EDX) of the worn disc tracks confirmed that the proportion of mineral phases from the regolith increased with test duration (Table 4.2).

Table 4.2. Elemental composition (weight %, beside Fe) of mineral phases on the worn disc surfaces (average values of 4 repetitions from 4 different locations of the wear track). LHS1.

R	Al	Si	Ca	Ti	K	Na
R2	2.23	2.27	0.12	0.08	0.07	0.04
R6	5.78	6.56	0.46	0.08	0.11	0.13
R15	12.81	13.29	1.10	0.17	0.07	0.32
R30	15.50	15.35	1.31	0.20	0.07	0.42

Further analysis of individual embedded particles revealed they were primarily calcium silicates with varying amounts of Na, K, Al, Fe, and Mg. Larger embedded particles tended to be calcium-aluminium-silicates, while smaller particles also contained sodium and magnesium. Additionally, Fluorine, originating from the abraded PTFE pin, was found to extensively cover the entire area, with higher concentrations at the locations of the embedded particles.

Pin surface analysis: The PTFE pin surfaces also showed progressive wear. The surface became completely covered with abrasive dust during the tests (Fig.4.5).

- R2 Pin: LHS1 regolith particles began to stick to and embed in the soft PTFE surface as shown in fig.4.5a). Large particles (>40 µm) were easily observed after just 2 minutes of abrasion.

- R6 Pin: In addition to embedded particles, deeper grooves began to appear, typically at the outer radius of the sliding zone.

- R15 Pin: A clear micro-cutting effect emerged, visible in bands across the surface.

- R30 Pin: The wear evolved into deeper, abrasive groove bands formed between the areas of embedded regolith particles. cut abrasive groove bands between embedded regolith particles.

With continued abrasion, smaller particles became more prevalent on the surface. It is theorized that larger particles either intruded into the steel counter face or were crushed into smaller pieces, though the latter is considered less likely given that the PTFE is much softer than the LHS1 particles.

a) Ln-SS- LHS1-R2 Pin   b) Ln-SS- LHS1-R30 Pin

Fig.4.5. Microscopic image (50x) of abrasive grooves and embedded particles of LHS1.

4.1.3   3D Surface topography analysis

To quantify the surface changes, 3D surface topography was investigated using a Keyence VR 5200 optical microscope. Both the disc and pin samples were cleaned with pressurized air, which left embedded and strongly adhered particles in place for the analysis.

Disc counter face topography: Analysis of the disc's wear tracks confirmed the findings from microscopy. Optical and 3D height maps showed discolored red spots, identified as embedded lunar soil particles, within the abraded grooves. The number of these embedded particles increased with the test duration. Furthermore, "particle-filled ridges" were observed along the
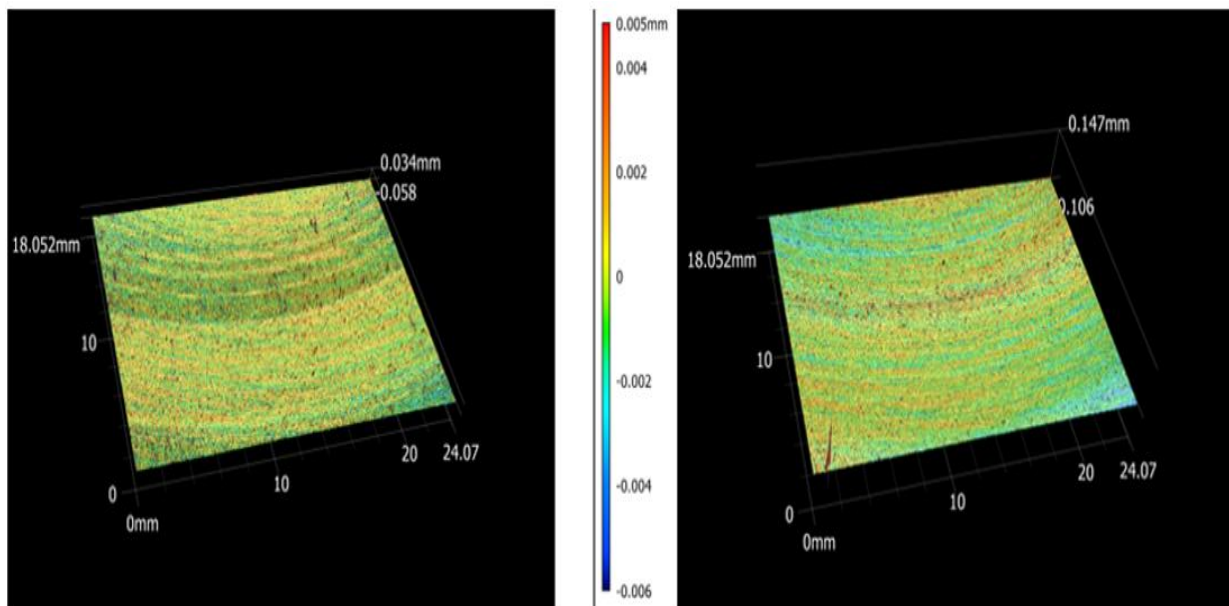
wear tracks, becoming more common on the outer radius (R6 and R30), which experienced a higher contact velocity (Fig.4.6 – 4.7).
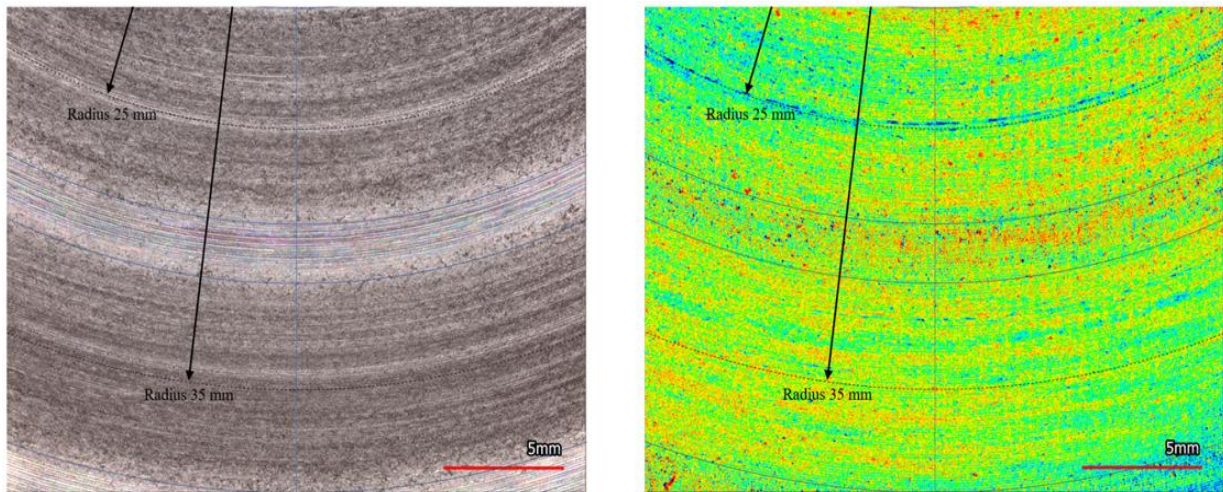
a) Discolored spots in the wear track   b) Colored spots in the wear track

Fig.4.6. Optical image (10x) and height map of R15 (radius 25mm) and R30 (radius 35mm) of disc.

a) R2-R6   b) R15-R30

Fig.4.7. 3D height map of test run wear tracks of disc.

To characterize the wear mechanism, the Degree of Penetration (Dp) was calculated using equation 2.8. The results were as follows in table 4.3.

Table 4.3. Degree of penetration (Dp) values of disc surface.

R	R2	R6	R15	R30
Dp	0.052	0.047	0.046	0.043

A Dp value below 0.1 is indicative of a dominant micro-ploughing abrasion mechanism, where material is plastically deformed and pushed into ridges alongside grooves rather than being removed. The data suggests this was the primary mechanism on the steel disc for all tests. The slight decrease in Dp with increasing test duration may reflect a "softening" effect as simulant particles fill the grooves, effectively smoothing the surface. The slightly higher Dp on the smaller radius (R2 and R15) suggests greater stress-torsion due to the track's curvature.

Polymer pin topography: On the PTFE pin, the wear mechanism was more complex. With increasing test time, the abrasion grooves became more uniform. The surface initially smoothened but then reached a saturation point around the R6-R15 runs, after which slight roughening occurred during the R30 run. This long-term roughening is attributed to the influence of embedded particles. (Fig.4.8.)
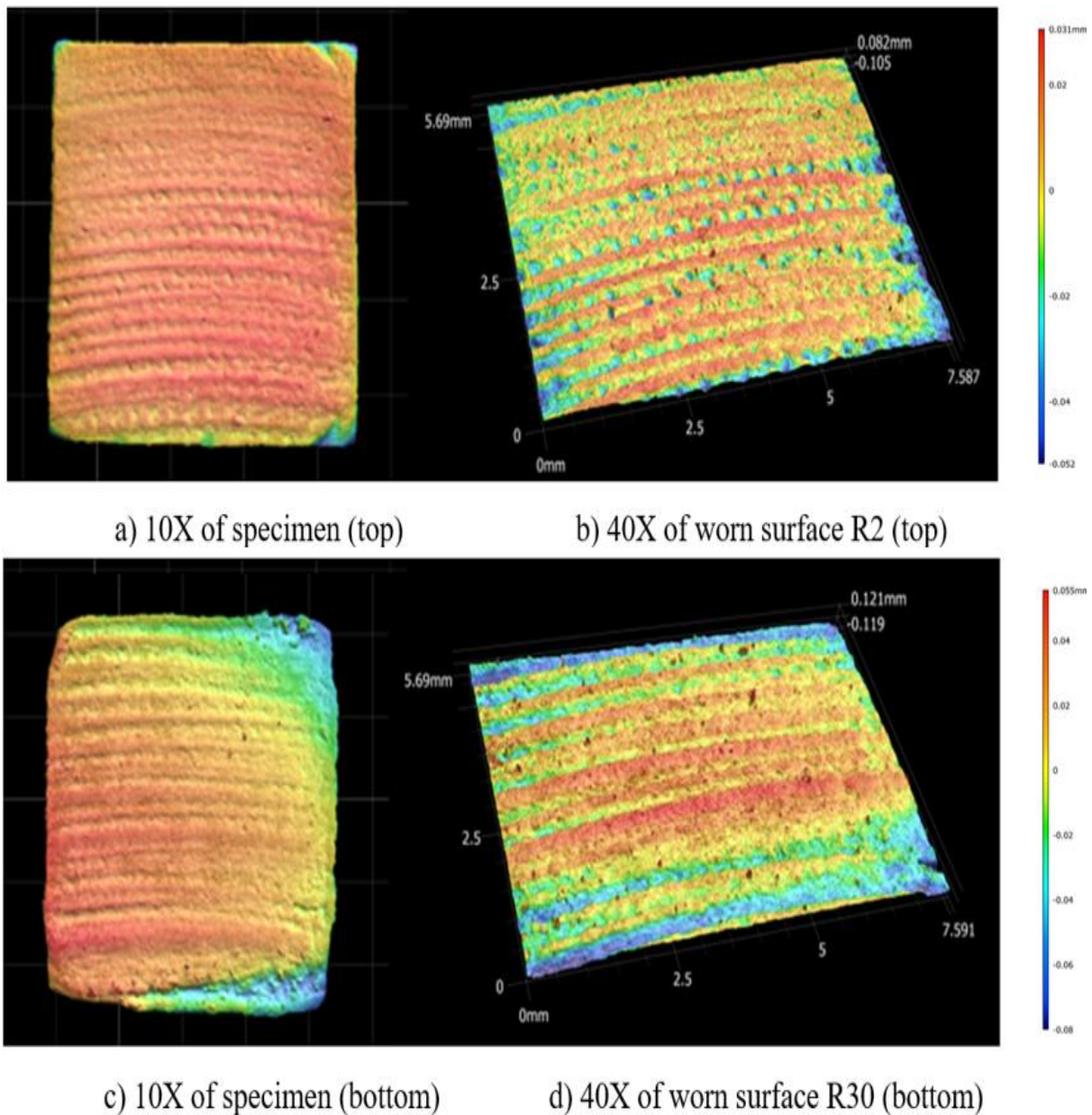

Fig.4.8. 3D image of specimen and worn surfaces of the PTFE pin.

76

The Dp values for the pin surface were significantly higher than for the disc surface:

Table 4.4. Degree of penetration (Dp) values of pin surface.

R	R2	R6	R15	R30
Dp	0.227	0.221	0.244	0.197

These values indicate a mixed-mode wear mechanism. The surface was plastically transformed via micro-ploughing (evidenced by distorted surfaces and ridges), while material was simultaneously removed via micro-cutting as the pin slid over the hard regolith particles. The Dp trend suggests that as the sliding distance increases, micro-cutting and material removal become more significant contributors to the overall wear process.

4.1.4   Conclusion (LHS1)

This tribological investigation provides comprehensive insights into the wear behaviour of a stainless steel/PTFE pair in the presence of LHS1 lunar regolith simulant. The study successfully characterized a complex three-body abrasive sliding mechanism that evolves from an initial adhesive-dominated phase. This mechanism is defined by the dynamic interaction of the LHS1 regolith particles, which embed, roll, and agglomerate within the contact zone.

Microscopic and spectroscopic analyses confirmed this process. On the stainless-steel disc, the dominant wear mechanism was identified as micro-ploughing, where regolith particles embed into the surface and cause plastic deformation, with the severity increasing over time. Elemental analysis verified the progressive accumulation of LHS1 constituents on the worn disc surfaces.

On the softer PTFE pin, a mixed wear mechanism of micro-ploughing and micro-cutting was observed. Initially, regolith particles embed into the polymer, but with continued sliding, these hard particles act as cutting tools, leading to the formation of deep abrasive grooves and significant material removal.

The Degree of Penetration (Dp) proved to be a valuable quantitative metric for identifying these distinct wear mechanisms on the two materials. These findings—particularly the characterization of the three-body dynamic and the identification of material-specific wear modes—are critical for predicting the performance and ensuring the longevity of mechanical systems operating in the abrasive, regolith-rich environments of Moon.

4.2   Pin-on-disc abrasive measurements with LMS1 regolith

This subchapter similarly to 4.1, introduces the results of the experiments carried out with LMS1 lunar regolith (lunar mare simulant).

4.2.1   Friction and wear analysis

The coefficient of friction (Fig.4.9) was calculated as an abrasive friction number characteristic of an open three-body abrasive sliding mechanism. The friction graphs, plotted with a moving average of 60 data points, showed reproducibility across the four durations (R2, R6, R15, R30). Fig.4.9 provides the friction coefficient graphs demonstrating the interaction of Ln-SS-LMS1 materials at a sliding velocity (v) of 0.1 m/s and a normal pressure (p) of 0.2 MPa.
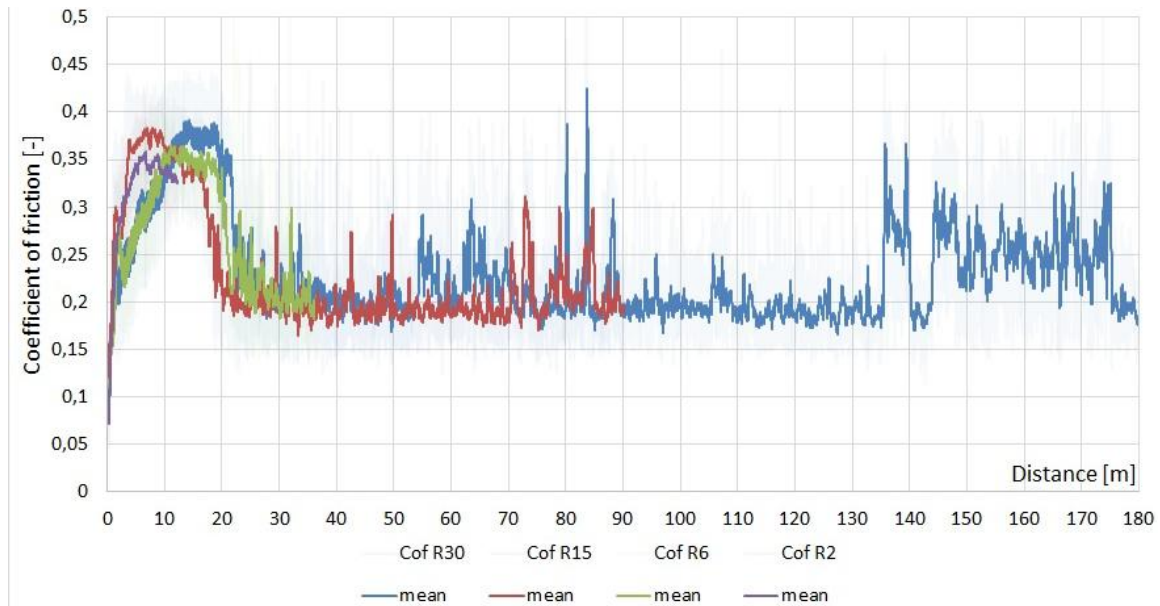
Fig.4.9. Summary of friction results (Ln-SS-LMS1-R2-R6-R15-R30).

In the initial 8-10 meters of the friction process, a run-in phase of pure PTFE/steel adhesive connection was observed, reaching a maximum friction of approximately 0.4. After 8-10 meters, LMS1 regolith particles entered the contact zone, leading to a transition from adhesive resistance to a lower sliding resistance due to grain rolling after 9-11 meters. This transitioned into the operation of Berthier-Eleőd 3-body abrasion, characterized by a dynamic zone balance. Salient friction peaks returned approximately every 10 meters, indicating the mechanism of the contact zone where particles were partially embedded in the softer PTFE surface, adhered to each other, rolled on the surface, broke up, and sometimes became congested. Simultaneously, abrasive scratches and grain embedment appeared on the steel surface. The process was characterized by a stabilized abrasive sliding resistance around 0.2-0.3, showing an almost constant or slightly decreasing trend.

The "wear" curves, representing the vertical displacement of the pin holder, were also plotted with a moving average of 60 data points and showed reproducibility (Fig. 4.10). Fig. 4.10. Demonstrates the wear curves or displacement (DP) in millimetres (mm) resulting from the interaction of Ln-SS-LMS1 materials at a sliding speed (v) of 0.1 m/s and a normal pressure (p) of 0.2 MPa.
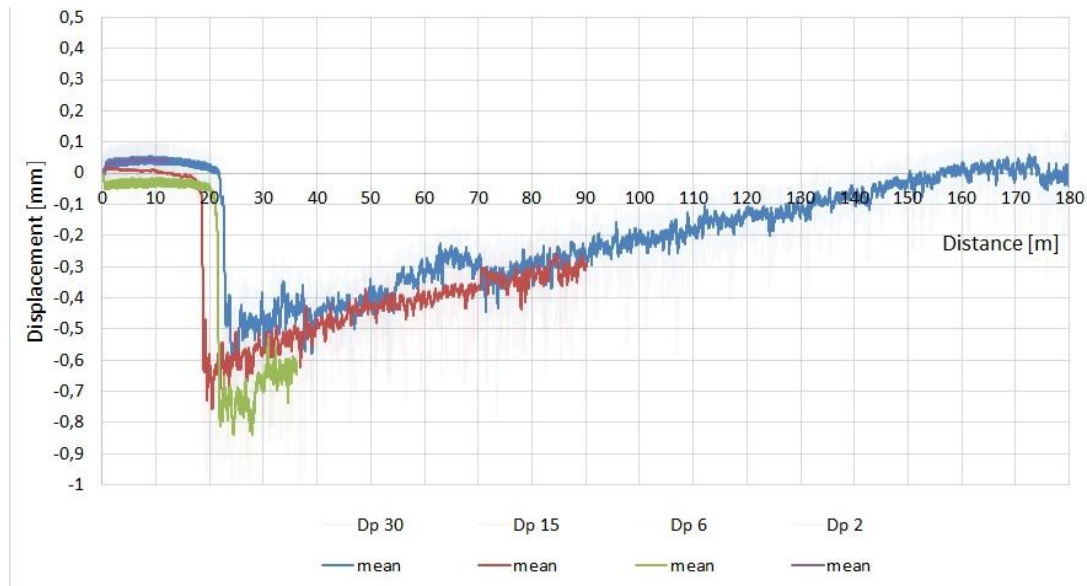
Fig.4.10. "Wear" curves showing the vertical displacement of the pin holder.

After 8-10 meters of adhesive sliding, the LMS1 regolith entering the contact zone raised the pin holder head, resulting in negative wear in the sliding range of 10-50 meters. Extreme peak values (down to -0.7 mm) indicated the effect of the accumulation of larger particles. As a result of the dynamic three-body zone described in the case of friction, the movement of grains and flakes was clearly perceived by the local peaks of the curves. The continuous cutting and micro-cutting of the PTFE pin test specimens by grain movement, characteristic of the contact zone dynamics, resulted in abrasive wear, which followed a classic linear abrasive wear trend after 30-40 meters of sliding. Up to 0.15 mm of wear (vertical displacement of the specimen holder, resulting from deformation, wear, particle dynamics, and thermal expansion) was observed in the test system. The trend of weight measurements of the pins gave the same trend (Table 4.5):

Table 4. 5. Weight change of the pins.

R	R2	R6	R15	R30
Δm of PTFE pins [g]*	0.006	0.011	0.001	-0.030

4.2.2 Microscopic and spectroscopic analysis

Scanning Electron Microscopy (SEM) and Energy Dispersive X-ray (EDX) analyses were conducted to investigate the surface morphology and elemental composition of the worn disc and pin samples. A Zeiss EVo 40 and JEOL JSM-IT700HR microscope were used for SEM. Before analysis, PTFE samples were coated with a thin gold film via sputtering to prevent electric charging. An X-Act (Oxford Instruments) 10 mm^2 EDS device with Aztec software was used for EDX.

Disc surface analysis: Microscopic results (50x magnification) of the disc top-side showed distinct features for R2 (Fig.4.11.) and R6 wear tracks.

• R2 Disc (top side, 50x): Indicated the initial stage of abrasive wear, with minimal damage to the metal micro-geometry and only submicron dust particles. Original grooves were

almost untouched. initial stage of abrasive wear, the metal micro-geometry begins to be damaged, the first signs of particle embedment and polymer adhesion appear.

- R6 Disc (top side, 50x): Showed signs of abrasive damage, with some original grooves still visible but covered by a layer of dust particles.

The back-side of the disc (R15, R30 – Fig.4.11) also exhibited specific wear patterns.

- R15 Disc (bottom side, 50x): Within the width of the wear track, the proportion of the damaged surface increased, with original grooves no longer visible, replaced by embedded particles and micro-cutting marks.

- R30 Disc (bottom side, 50x): Showed significant surface damage, with widespread embedded particles and deep micro-cutting grooves. increasing surface damage (cutting effect of particles stuck on the PTFE pin), the parallel bands are getting wider but still not the whole contact area is covered by embedded particles and adhered PTFE.

a) Ln-SS- LMS1-R2 disc (top)   b) Ln-SS- LMS1-R30 disc (bottom)

Fig.4.11. Top-surface of the worn disc sides of magnification of 50x.

SEM images of the disc worn surface in various magnifications further elucidated the wear mechanisms (Fig.4.12).

- R2 Disc: Original grooves were still visible, but abrasive dust ruined the surface by creating scratches and inclusions from embedded particles.

- R6 Disc: The density of damaged parts increased with abrasion time. Most embedded particles were smaller than the D10 size of the LMS1 abrasive powder.

- R15 Disc: The density of damaged parts continued to increase, with many embedded particles and clear signs of micro-ploughing and micro-cutting.

- R30 Disc: Increased density of damaged parts and a higher number of bumps were observed, indicating significant particle embedment and surface roughening.
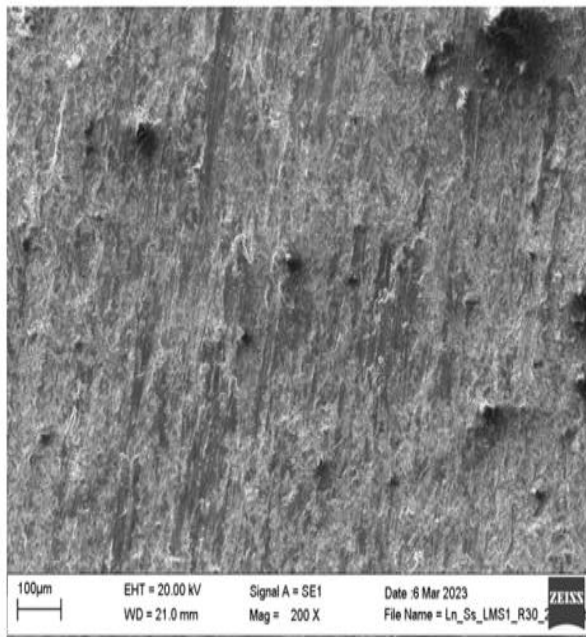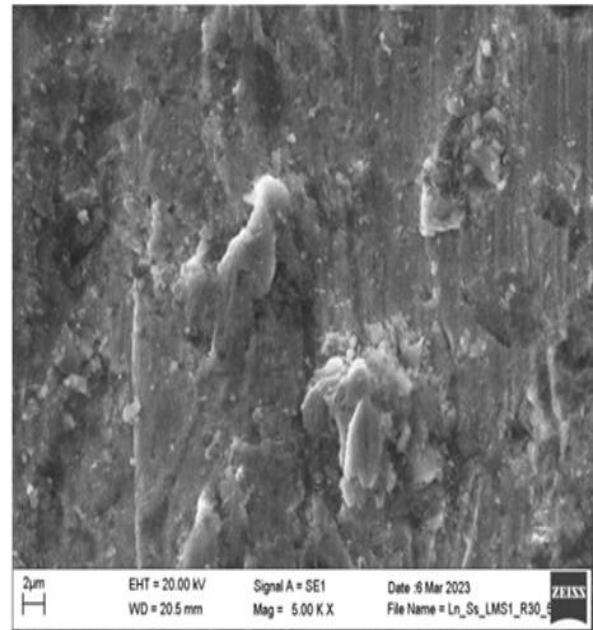
a) 200X   b) 5000X

Fig.4.12. SEM images of worn disc by LMS1 in various magnification (R30).

Elemental analysis (EDX) of the worn disc parts (Table 4.6.) revealed an increasing proportion of the mineral phase stuck into the worn paths was obvious.

Table 4.6. Elemental composition (weight %, beside Fe) of mineral phases on the worn disc surfaces (average values of 4 repetitions from 4 different locations of the wear track) LMS1.

R	Al	Si	Ca	Ti	K	Na
R2		0.43	0.04	0.04	0.06	0.02
R6	1.97	3.58	0.225	0.30	0.09	0.13
R15	4.38	7.19	0.53	0.78	0.08	0.29
R30	4.81	7.68	0.58	0.83	0.10	0.32

SEM images for elemental analysis of selected particles on the worn disc showed abundant dust particles covering the disc material. The elemental composition of particles embedded in the disc matrix indicated they were primarily calcium silicates with varying content of Na, K, Al, Fe, and Mg. Specifically, olivine, ilmenite, basalt, and anorthite were identified. Fluorine from the abrasion of the PTFE pin extensively covered the entire area and accumulated at the spots of the embedded ceramic particles.

Pin surface analysis: Microscopic results (50x magnification) of natural PTFE pin worn surfaces provided insights into the wear evolution (Fig.4.13.).

- R2 Pin: Regolith particles started to stick into the PTFE surface, covering it. But partially they are loosen.

81

- R6 Pin: Beside the embedded particles, a thicker and more uniform layer of regolith particles covered the surface.

- R15 Pin: Micro-cutting effects appeared in bands, with embedded particles becoming more dense.

- R30 Pin: Deep cut abrasive groove bands were observed between densely embedded regolith particles, forming a consistent layer. Thick layer from fine grain particles covers evenly the whole surface.

a) Ln-SS- LMS1-R2 PTFE pin   b) Ln-SS- LMS1-R30 PTFE pin

Fig.4.13. Microscopic image (50x) of the abrasive grooves and embedded particles of LMS1.

SEM images of the surface of abrasive pins during wear tests showed that the pin surface was completely covered with the used abrasive dust. After 2 minutes of abrasion (R2), large (>40 µm) particles were easily observed on the surface. With continued abrasion, particles below that size became more prevalent. Larger particles either intruded into the steel matrix or crushed into smaller ones, although this latter seemed to have a smaller chance as the lower hardness of PTFE than LMS1 powder particles.

4.2.3   3D surface topography analysis

3D surface topography investigations were performed using a Keyence VR 5200 3D optical microscope (white light interferometer). Prior to analysis, both counter face discs and polymer pin samples were cleaned with pressurized air, ensuring that embedded and stuck particles remained.

Disc counter face analysis: For the counter face analysis, a low magnification 10X lens with high resolution surface capture setting was used, covering an 18.065 x 24.087 mm scanned area in 8 pre-defined locations on the disc (4 on each side), enabling 4 measurements from each wear track. The disc was rotated 90° after each scan to enable "parallel wear tracks" with projected light beams.

Optical images and height maps of R2 (radius 25mm), R6 (radius 35mm), R15 (radius 25mm), and R30 (radius 35mm) wear tracks were analysed (Fig.4.14.-4.15.).
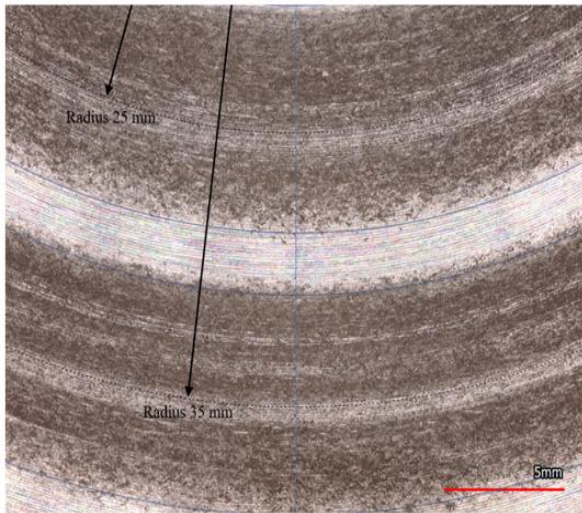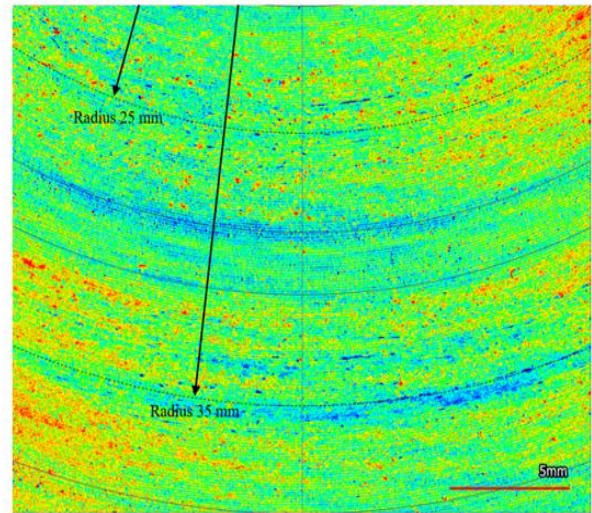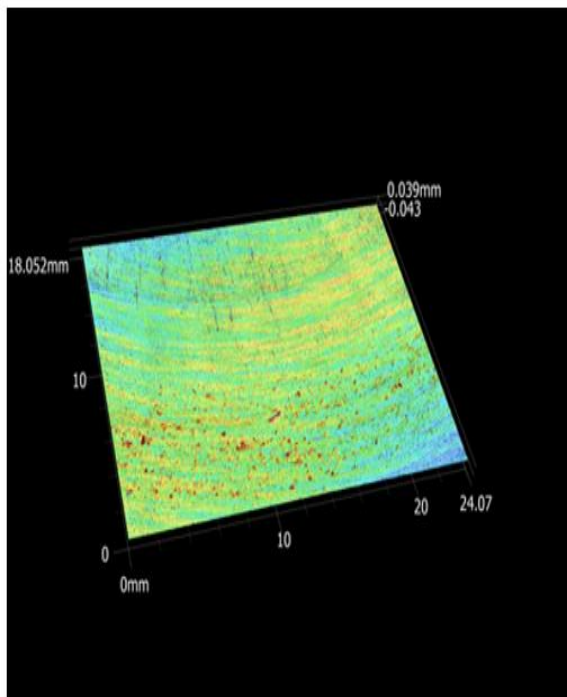
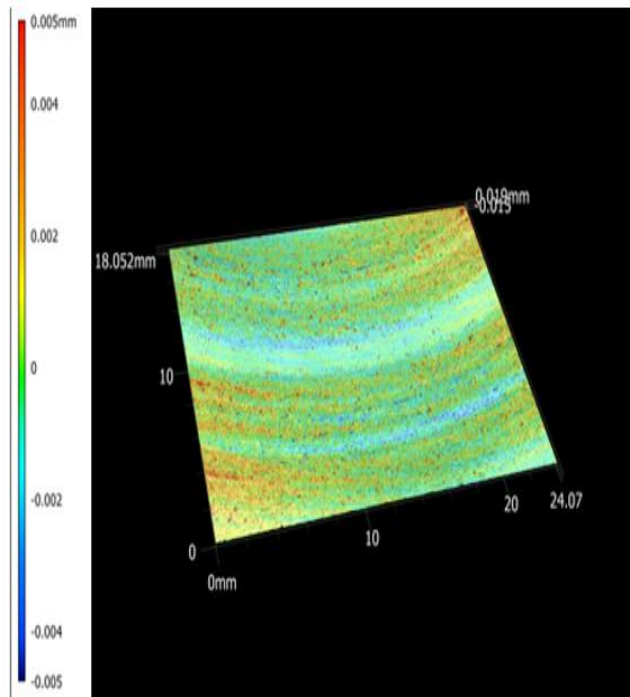a) Discolored spots in the wear track   b) Colored spots in the wear track

Fig.4.14. Optical image (10x) and height map of R15 (radius 25mm) and R30 (radius 35mm) by LMS1.

a) R2-R6   b) R15-R30

Fig.4.15. 3D height map of test run wear tracks by LMS1.

After setting the measurement reference plane, optical images were analyzed for wear damage, including transfer layer formation and particle embedding. Discolored spots in the wear track indicated lunar soil particles embedded in the abraded grooves. With increasing test run length, more embedded particles were present. Formed "particle-filled ridges" along the wear track were more common towards the bigger radius (higher velocity surface contact). 3D height maps confirmed these findings, with the same height scale set for comparison.

2D roughness results were obtained to calculate the Degree of penetration (Dp), which characterizes wear micro-mechanisms and indicates wear severity. The mean Dp of all grooves present on the worn surface was calculated using Rz and Rsm, corresponding to groove depth and width. Dp is calculated using equation 2.8. The results were as follows in table 4.7.

Table 4.7. Degree of penetration (Dp) values of disc surface.

R	R2	R6	R15	R30
Dp	0.044	0.041	0.038	0.024

A Dp value less than 0.1 indicates a dominant micro-ploughing abrasion wear micro-mechanism on the disc surface with plastic deformation of the material and formation of ridges along the abrasion grooves. This data may indicate the softening effect of the embedded regolith. As the simulant particles fill up the wear grooves the Dp is measured to be lower. Wear tests performed on a smaller radius resulted in slightly higher Dp, indicating more stress-torsion of the surface due to the track curvature.

3D surface roughness data extraction was performed from an area of 7x7 mm with a 0.8 cut off (λ) value and Gaussian filter according to ISO 25178 standard. The area roughness measurement results were in line with the multiple-line roughness measurements, with a slight proportional (+10%) increase due to the fact that the evaluation is not restricted to one direction. The decrease in roughness could further indicate the presence of regolith simulant particles filling up the wear grooves and thus smoothening the roughness. However, the embedded particles could also act as roughness peaks (ridges) and could contribute to an overall roughened surface.

Polymer pin analysis: For polymer pin analysis, a high magnification 40X lens with high resolution surface capture setting covered a 5.69 x 7.587 mm scanned area in the centre of the 8x8 mm pin surface, while a low magnification 10X lens with high resolution surface capture setting covered an 18.065 x 24.087 mm scanned area to capture overall geometry transformation. Optical and height map investigations of wear damage, surface deformation, and particle embedding showed that increase of test time resulted in more uniform abrasion groove patterns (Fig.4.16). R2 test showed significant plastic deformation, R30 test showed abrasion grooves. Embedded particles were more clearly identified with increase in test run.
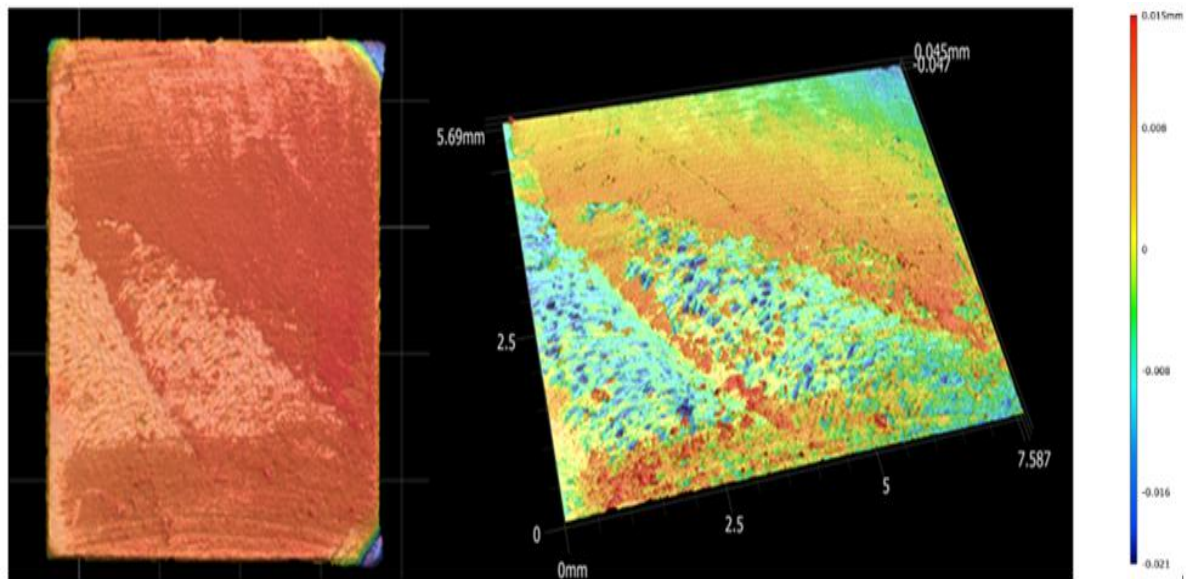
a) 10X of specimen (top side)   b) 40X worn surface of R2 (top side)
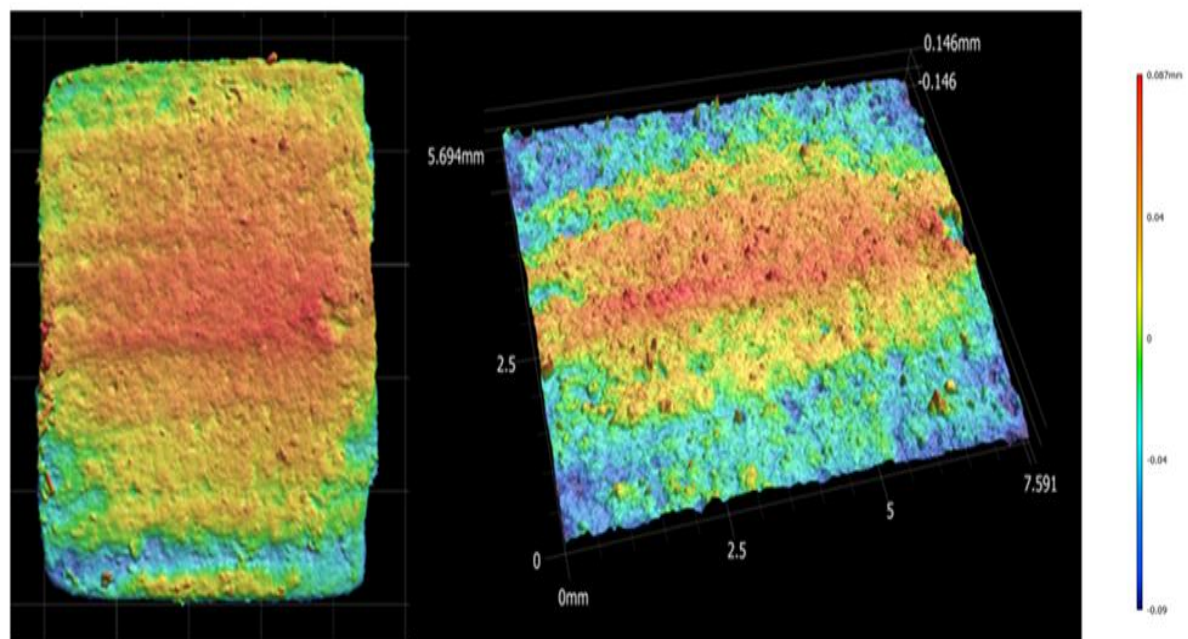
c) 10X of specimen (bottom side)   d) 40X worn surface of R30 (bottom side)

Fig.4.16. 3D image of specimen and worn surface pin.

Multi-line 2D roughness data was extracted from the wear tracks for Dp calculation.

The polymer pin surface smoothened with increased run time, however reached a saturation point around R6-R15 and for R30 a slight roughening occurred. As the material was worn off, the wear tracks were more uniform due to the abrasion, but the embedded particles influenced the roughness on the long run. The data was obtained from the average of 30 lines perpendicular to wear grooves, with an investigated length of 5.69 mm with a 0.8 cut off (λ) value and Gaussian filter according to ISO 25178 standard.

85

Table 4.8. Degree of penetration (Dp) values of pin surface.

R	R2	R6	R15	R30
Dp	0.181	0.372	0.307	0.239

The dominant surface transformation of the counter face was mixed in all tests. The surface was plastically transformed through micro-ploughing (distorted surfaces, ridges), while material was removed through micro-cutting due to the slide over hard regolith particles. As the sliding distance increased, the Dp indicates more micro-cutting and material removal. The area roughness measurement results were in line with the multiple-line roughness measurements. The slight proportional (+10%) increase was due to the fact that the evaluation was not restricted to one direction (perpendicular to the formed grooves).

4.2.4   Conclusion (LMS1 regolith)

The tribological investigation provided comprehensive insights into the wear behavior of stainless steel and PTFE specifically in the presence of LMS1 lunar regolith simulant. The friction and wear curves demonstrated a distinct run-in phase followed by a three-body abrasive sliding mechanism, characterized by particle embedment and rolling unique to the LMS1 regolith interaction. Microscopic analyses confirmed the progression of wear, from initial surface damage and particle adhesion on the disc to micro-cutting and deep groove formation on the PTFE pin, with direct evidence of LMS1 particle involvement. Elemental analysis highlighted the accumulation of LMS1 regolith constituents on the worn surfaces. 3D surface topography further characterized the micro-ploughing as the dominant wear mechanism on the disc and a mixed micro-ploughing and micro-cutting mechanism on the PTFE pin, with the Degree of penetration (Dp) serving as a valuable indicator of wear severity and mechanism, all within the context of LMS1 abrasion. These findings are crucial for predicting the longevity and performance of mechanical components in extra-terrestrial environments, specifically when exposed to LMS1 regolith.

4.3   Comparative analysis of the results with LHS1 and LMS1 regolith simulants

This section provides a comparative analysis of the tribological behaviour of the stainless steel/PTFE material pair when subjected to two different regolith simulants: LHS1 (lunar highland) and LMS1 (lunar mare). The comparison focuses on the friction and wear characteristics, as well as the resulting surface transformations, to highlight the similarities and distinct differences in the abrasive nature of these two materials.

4.3.1.   Friction and wear behaviour

The friction and wear data, captured in real-time, provide a macroscopic view of the system's dynamic response to each simulant. While the overall patterns show similarities rooted in the shared three-body abrasion process, key quantitative differences reveal the varied severity of the two simulants.

Coefficient of friction (CoF)

Both the LHS1 and LMS1 systems exhibit a comparable friction evolution, which begins with a distinct run-in phase over the first 8-10 meters of sliding. During this phase, the initial

PTFE/steel adhesive contact results in a sharp increase in friction. However, the peak friction reached is slightly higher for the LMS1 system, at approximately 0.4, compared to about 0.35 for the LHS1 system. Following this adhesive phase, the ingress of regolith particles into the contact zone transitions the system to a Berthier-Eleőd three-body abrasion mechanism in both cases. This is characterized by particles embedding, rolling, and agglomerating. A notable divergence appears in the stabilized friction regime that follows.

1. LHS1: The system settles to a lower and more stable coefficient of friction of approximately 0.2. The friction curve, while showing dynamic peaks, remains relatively consistent around this mean value for the duration of the tests.

2. LMS1: The system maintains a higher and more variable CoF, fluctuating between 0.2 and 0.3. This suggests a more aggressive or less stable interaction between the LMS1 particles and the tribological surfaces.

Vertical displacement of pin holder (Wear): The vertical displacement curves, which represent a combination of wear, particle dynamics, and deformation, also show analogous initial behaviour. For both simulants, the entry of regolith into the contact zone after 8-10 meters physically lifts the pin holder, resulting in a negative displacement reading. However, the magnitude of this effect and the subsequent wear are significantly different:

• Pin lift (negative wear): The pin lift is more pronounced in the LMS1 test. While the LHS1 system shows peak negative displacements down to -0.5 mm due to particle agglomeration, the LMS1 system registers extreme peaks as low as -0.7 mm, indicating the formation of larger or more resistant particle blockages.

• Abrasive Wear: After the initial dynamic phase, both systems transition to a more linear abrasive wear trend. The total vertical displacement by the end of the longest test (R30) is substantially greater for the LMS1 simulant, reaching up to 0.15 mm, compared to a maximum of 0.1 mm for the LHS1 system. This points to a higher rate of material removal by the LMS1 particles.

4.3.2. Surface analysis and wear mechanisms

Post-test surface analysis confirms the trends observed in the friction and wear data. The wear mechanisms on both the steel disc and the PTFE pin differ in intensity and character between the two simulants.

Stainless-steel disc: On the stainless-steel disc, both simulants induce a micro-ploughing abrasion mechanism, where the material is plastically deformed rather than cut. This is confirmed by the Degree of Penetration (Dp) values, which are well below 0.1 for all tests in both systems.

PTFE pin: The softer PTFE pin experiences a more aggressive mixed-mode wear mechanism of both micro-ploughing and micro-cutting in both scenarios. Hard regolith particles first embed in the polymer and then act as cutting tools. The Dp values, which are higher than those for the disc, quantify this mixed mechanism. The evolution of Dp suggests a difference in the dominant process over time:

• LHS1: The Dp values are 0.227 (R2) and 0.197 (R30). The general trend suggests that after an initial phase, the wear process stabilizes, and the significance of micro-cutting does not escalate dramatically.

- LMS1: The Dp values are 0.181 (R2) and 0.239 (R30), with a peak of 0.372 at the R6 run. This trend, particularly the higher value at R30 compared to R2, indicates that as sliding distance increases, micro-cutting and material removal become more significant contributors to the overall wear process with the LMS1 simulant.

4.3.3. *Summary of comparison*

In summary, while the fundamental three-body tribological processes are similar for both the lunar (LHS1 and LMS1) simulants, the LMS1 simulant consistently demonstrates a more severe abrasive effect on the stainless steel/PTFE system. This is evidenced by a higher coefficient of friction, greater pin displacement and wear, and surface analysis that points to more aggressive micro-cutting on the polymer pin over time. Conversely, the LHS1 simulant shows a greater propensity for its particles to embed in the steel counter face. The key quantitative distinctions are summarized in table 4.9.

Table 4.9. Summary of tribological features with LHS1 and LMS1.

Parameter	LHS1 lunar simulant	LMS1 lunar simulant	Key difference
Peak CoF (Run-in)	~0.35	~0.4	LMS1 is ~14% higher
Stabilized CoF	~0.2 (stable)	0.2- 0.3 (variable)	LMS1 is higher and less stable
Max. negative wear (particle ingress)	-0.5 mm	-0.7 mm	LMS1 causes 40% greater pin lift
Total Displacement (Wear)	up to 0.1 mm	up to 0.15 mm	LMS1 causes 50% more wear
Disc Wear Mechanism	Micro-ploughing	Micro-ploughing	Similar mechanism
Disc Material Transfer (R30)	Al: 15.50%, Si: 15.35%	Al: 4.81%, Si: 7.68%	LHS1 shows 2-3x more embedding
Pin Wear Mechanism	Mixed micro-ploughing/cutting	Mixed micro-ploughing/cutting	LMS1 shows more significant micro-cutting over time

While the density of particles embedded within the surface roughness of the stainless-steel disc was higher for the LHS1 regolith, the overall volume of regolith occupying the contact zone was larger for LMS1. This finding, which is evident in both the online wear curves and a comparison of fig. 4.3 and fig.4.11, highlights the more dominant internal friction and adhesion of LMS1 particles, resulting in a thicker third-body layer.

4.4   Numerical simulations (DEM)

The tribological experiments conducted with lunar regolith simulants against PTFE substrates provided essential empirical evidence for the mechanisms of wear under extra-terrestrial soil conditions. These laboratory investigations established the baseline phenomena of abrasion and material removal, thereby defining the physical reference frame within which numerical modelling efforts must be situated. Yet, while experimental observations capture the direct manifestation of regolith–material interaction, they are inherently constrained to specific test configurations, particle batches, and operational conditions. To enable predictive analyses that extend beyond these controlled scenarios, the discrete element method (DEM) was employed as a complementary tool. DEM simulations offer the unique capability to represent granular assemblies at the particle scale and, through controlled variation of contact parameters, to systematically explore their emergent bulk and wear related behaviour.

The reliability of such simulations, however, depends critically on the careful calibration of input parameters, since quantities such as interparticle friction, adhesion, and coefficient of restitution do not map trivially from laboratory measurements to numerical input values. In this work, calibration was approached in a twofold manner. On the one hand, classical benchmarking procedures (reproducing experimentally determined angles of repose) were carried out to ensure consistency between the simulated assemblies and their physical counterparts. On the other hand, the analysis was extended to derive functional relationships between microscopic parameters and macroscopic observables. In particular, the dependence of repose angle on interparticle friction was quantified by a logistic relation, capturing the nonlinear and saturating nature of this response. Similarly, the role of cohesive interactions was parameterized to account for the enhanced heap stability observed in angular regolith grains.

By establishing these functional correlations, the present study advances beyond a mere case-specific calibration of DEM assemblies. Instead, it provides a transferable framework that enables other researchers to adapt slightly different particle morphologies or simulant batches to calibrated numerical models without repeating the entire procedure from first principles. In this way, the experimental wear investigations and the DEM simulations are integrated into a coherent methodology: the former anchor the study in measurable physical reality, while the latter generalize the results into functional laws that extend predictive capability and facilitate broader application in regolith–material interaction research.

Following the completion of the calibration procedures and the accompanying sensitivity analyses, an additional series of simulations was carried out with the specific objective of reproducing the wear behaviour observed in the pin-on-disc experiments. In this context, the primary aim was to determine the wear coefficient, expressed as the ratio of volumetric material loss to shear work input, for the PTFE specimen in contact with lunar regolith. Due to the considerable computational demands of such simulations, the analysis was restricted to the LHS-1 highland simulant, which is characterized by angular particle morphology and higher abrasivity. A further computational challenge arose from the requirement to employ the real Young's modulus of the lunar particles in order to capture realistic contact stresses during sliding. This modification, while essential for physical fidelity, substantially increased the numerical cost of the simulations. Nevertheless, this extension of the DEM framework provided the necessary link between calibration against bulk granular behaviour and the quantitative modelling of regolith-induced wear, thereby bridging the gap between tribological experiments and numerical prediction.

In adapting the present methodology to other extra-terrestrial soils such as Martian dust, the central principle is that only a limited set of parameters needs to be adjusted, while the overall modelling framework remains unchanged. In the current study, the DEM assemblies were calibrated primarily by matching experimentally measured angles of repose, which were found to depend nonlinearly on interparticle friction and linearly on adhesive surface energy. This procedure ensures that the simplified numerical grains reproduce the bulk stability of real simulants despite their reduced geometric complexity. For any new soil type, the same calibration route should be followed: (i) measure the angle of repose (or another accessible bulk property) of the target material, (ii) identify the combination of friction and adhesion that reproduces this value in the simulations, and (iii) verify consistency by sensitivity tests. In addition to these bulk-level adjustments, the tribological response must also be recalibrated by determining the wear coefficient from pin-on-disc or equivalent tests with the new material. This constant, expressed as the ratio of volumetric material loss to shear work input, serves as the direct bridge between experiments and DEM wear simulations. Once both the bulk calibration and the wear constant are established, the tribological wear simulations can be carried out with the corresponding parameter set, complemented by the appropriate mechanical properties of the dust grains (e.g. Young's modulus, density). In this way, the procedure is transferable: while the present work focused on lunar highland and mare simulants, the same workflow can be applied to Martian regolith or other planetary soils by substituting the experimentally determined repose angle and wear coefficient into the calibration stage and updating the material constants accordingly. This makes the approach broadly applicable, providing predictive capability across different extra-terrestrial environments without requiring a complete redesign of the numerical model.
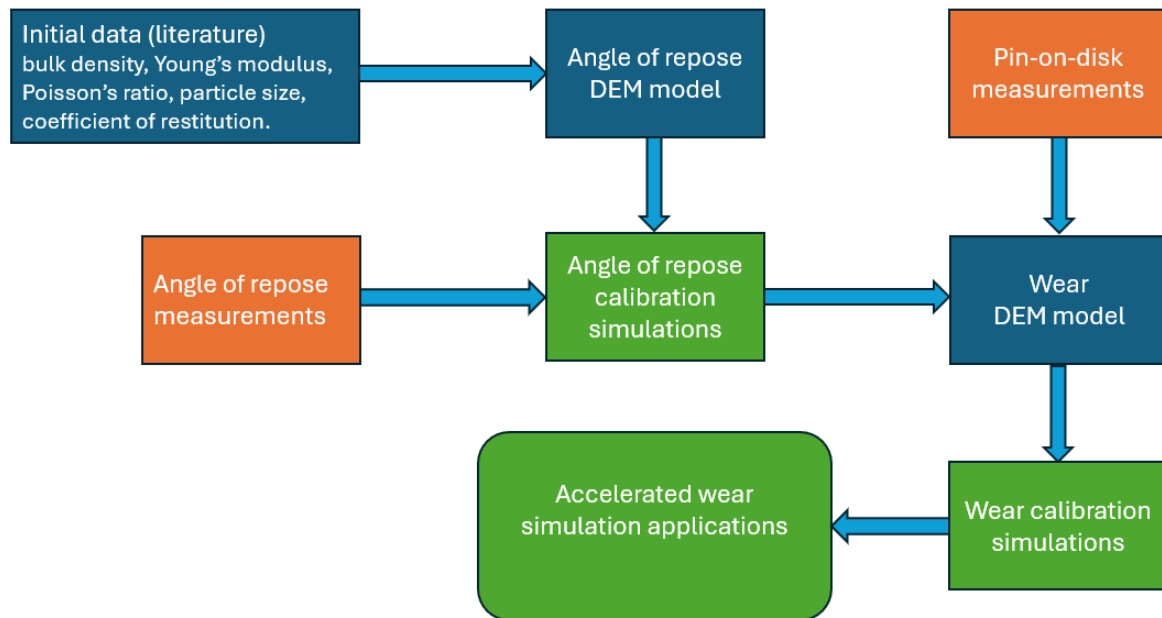

Fig.4.17. Workflow of data sources, calibration, and DEM-based wear modelling.

The schematic diagram (fig.4.17) illustrates the overall methodology of the study. Initial material constants such as density, Young's modulus, Poisson's ratio, particle size, and restitution coefficient were obtained from the literature. Bulk behaviour was characterised

experimentally by angle of repose measurements, while tribological properties were determined by pin-on-disc tests. These data provided the basis for two distinct DEM models: heap formation and wear simulations. Through calibration against the experimental measurements, the key micromechanical parameters (friction and adhesion) as well as the wear coefficient were determined. Once established, this calibrated framework enabled the application of accelerated wear simulations to explore a wide range of geometric and kinematic configurations, thereby reducing the need for costly and time-consuming experimental campaigns.

Once a reliable accelerated wear model has been established through the calibration of both bulk behaviour and wear coefficients, the framework can be extended far beyond the specific pin-on-disc configuration. Within the same calibrated material system, DEM simulations can be employed to investigate a wide range of geometrical layouts, loading regimes, and kinematic configurations. In this predictive role, the model makes it possible to identify potentially critical wear scenarios at an early stage, thereby highlighting the most severe operating conditions before any physical testing is performed. Such pre-screening significantly reduces the number of costly and time-consuming experimental campaigns that need to be conducted, while still ensuring that the retained tests focus on the most relevant and challenging cases. In this way, the accelerated DEM wear model not only deepens our understanding of regolith-induced abrasion but also provides a practical tool for streamlining the design and validation process of space hardware components exposed to dusty extra-terrestrial environments.

4.4.1. Angle of repose measurements

The angle of repose was determined experimentally for both lunar mare and lunar highland simulants by allowing the granular material to form a free-standing heap under gravity after controlled release. The resulting conical piles were evaluated by image-based geometric analysis, yielding reproducible slope angles that reflect the combined influence of particle morphology, surface roughness, and interparticle friction. The measured values show distinct differences between the two simulants: the mare soil, characterized by smoother and more equidimensional grains, exhibited a lower repose angle, while the highland simulant, with its more angular and irregular particles, formed significantly steeper heaps. These results not only provide essential calibration targets for the DEM simulations but also highlight the sensitivity of macroscopic heap stability to microstructural properties of lunar regolith.

The angle of repose of the lunar regolith simulants was determined using a cylindrical lift test. A vertical steel cylinder with an internal diameter of 20 mm and a height of 30 mm was used as the confinement device. The cylinder was first placed on a flat horizontal plate and filled with the granular material to its full height (Fig.4.18). After the filling process, the cylinder was slowly lifted vertically at a controlled rate, allowing the particles to collapse freely under gravity and form a self-supporting conical heap on the base plate. Once the particles reached a stable configuration, the geometry of the pile was characterized by measuring both the maximum pile height and the average base diameter. The static angle of repose was then calculated from these dimensions using the geometric relation $\tan \theta = \frac{h}{r}$, where h is the pile height and r is the mean base radius of the heap. This procedure ensured reproducibility and minimized dynamic effects associated with pouring methods, thereby yielding consistent values of the static repose angle for both the mare and highland simulants (Fig. 4.19).
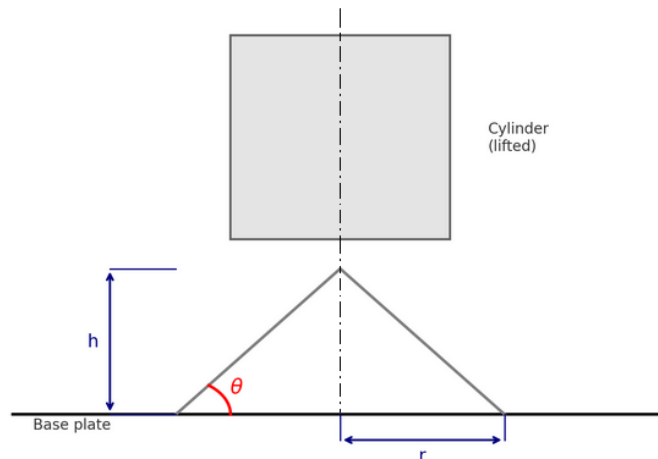
Fig.4.18. Angle of repose test schematics

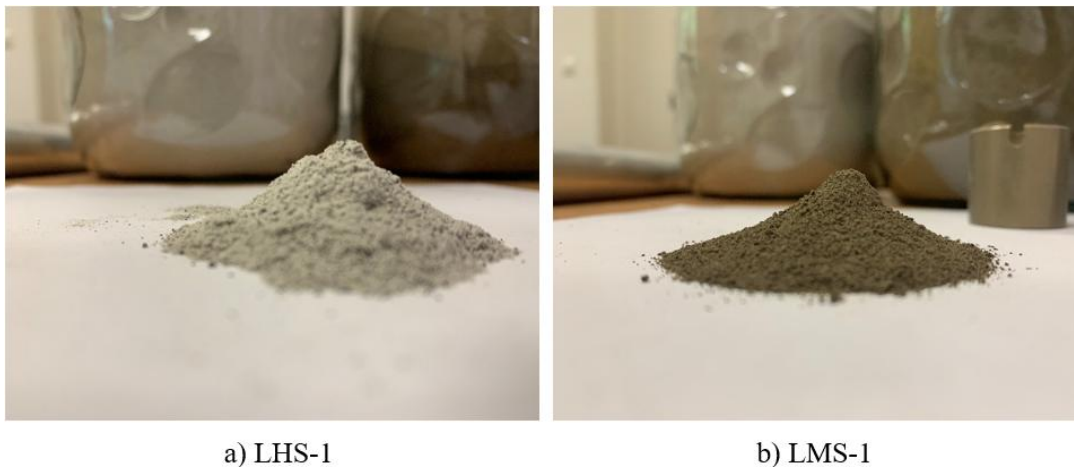a) LHS-1   b) LMS-1

Fig.4.19. Angle of repose test example photos

The angle of repose measurements revealed clear differences between the two investigated simulants (Table 4.10).

Table 4.10. Measured angle of repose values and their average [°].

Measurement	LHS-1	LMS-1
1	33.69	29.95
2	36.38	30.37
3	32.74	28.21
4	33.21	27.84
5	34.15	28.21
Average	34,03±1.41	28.92±1.16

For the highland simulant (LHS-1), the average static repose angle was 34° with a dispersion of 1.4°, while the mare simulant (LMS-1) exhibited a significantly lower value of 29° with a

dispersion of 1.2°. These results confirm the expected influence of particle morphology: the more angular and irregular highland grains promote stronger mechanical interlocking and steeper heap formation, whereas the comparatively smoother mare particles yield shallower slopes.

4.4.2. Angle of repose test numerical model

The simulation was conducted using a discrete element method (DEM) to model the formation of a granular heap after vertical confinement removal. The particle material was defined by a bulk density of $1300 \, kg/m^3$ and a true material density of $2166.67 \, kg/m^3$. To ensure computational efficiency, the Young's modulus was set to 1 MPa and the Poisson's ratio to 0.25. The particles interacted via a linear contact model with friction, restitution, and cohesion.

The interparticle coefficient of restitution was fixed at 0.5. The static interparticle friction coefficient was varied systematically across simulations to investigate its effect on the final heap geometry, while the dynamic friction was always set to 90% of the static value. A very low cohesive energy density of $1 \, 10^{-7} \, J/m^2$ was applied to minimize cohesive effects; its influence has been analysed separately in a later phase of the research.

The particles were polyhedral in shape, defined by 10 vertices per grain. Their morphology was characterized by a vertical aspect ratio of 1.5, and horizontal aspect ratio of 0.75, yielding elongated prismatic forms (Fig.4.20). The equivalent spherical particle diameter was $7.5 \times 10^{-5} \, m$. Particles were initialized with random orientations and spatial distributions.
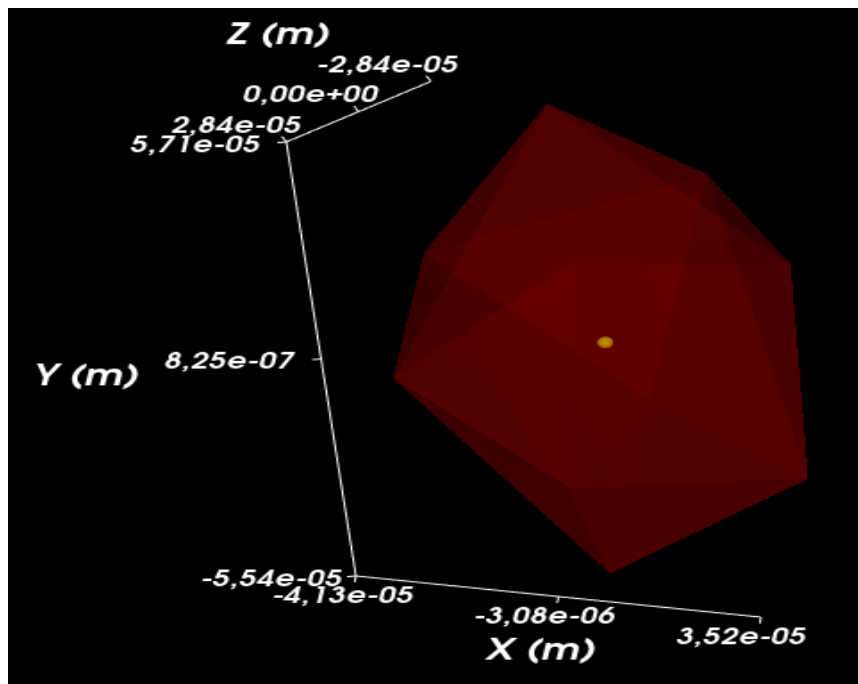

Fig.4.20. Polyhedral particle shape

Contact interactions with the bottom plate were assigned a static and dynamic friction coefficient of 0.5, and a coefficient of restitution of 0.5. The cylindrical container wall was assumed to be made of frictionless steel, with a restitution coefficient of 0.3.

The simulation consisted of six main stages. Initialization: A large bottom plate was defined at the base. A vertical cylinder was built around the plate to serve as a confining container (Fig. 4.21).
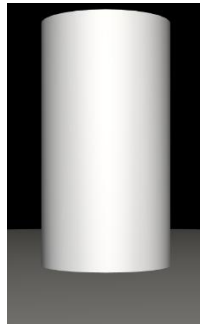

Fig.4.21. Cylindrical wall

Particle Insertion: Particles were randomly generated and inserted into the cylindrical domain in a gravitational field (Fig. 4.22).
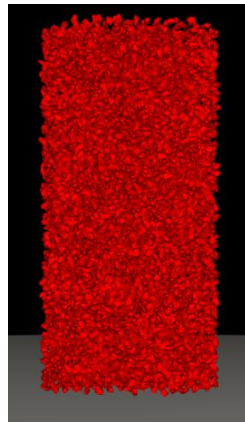

Fig.4.22. Random particle fill, the cylinder geometry is omitted here

Settling: The system was allowed to evolve under gravity until the particles fully settled into a mechanically stable packing (Fig. 4.23).
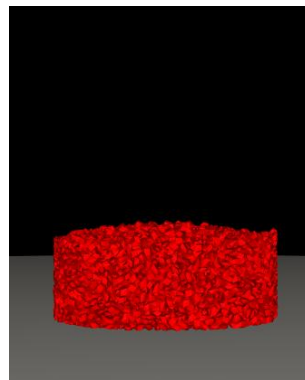

Fig.4.23. Gravitational sedimentation in the cylinder (the cylinder is omitted here)

Wall Removal: The cylindrical wall was slowly elevated (Fig.4.24), allowing the particles to collapse and form a natural heap. Particles that fell beyond the base plate were removed from the simulation domain.

Fig.4.24. Elevating the cylindrical wall

Final Heap: The resulting conical pile was visualized and exported for geometric analysis (Fig.4.25).
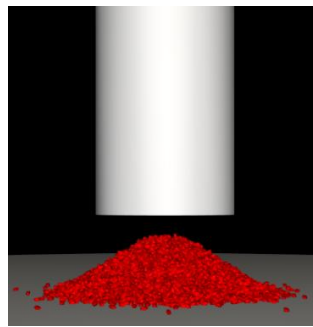

Fig.4.25. Final shape of particle heap, after cylinder full elevation.

This process enabled a reproducible formation of granular heaps from identical initial conditions while allowing the influence of the interparticle static friction to be isolated and evaluated.

The angle of repose was computed by a custom post-processing script that performed radial profiling in cylindrical coordinates. The base plate was divided into 20 equal sectors (Fig. 4.26). In each sector, the highest particle elevation was detected.
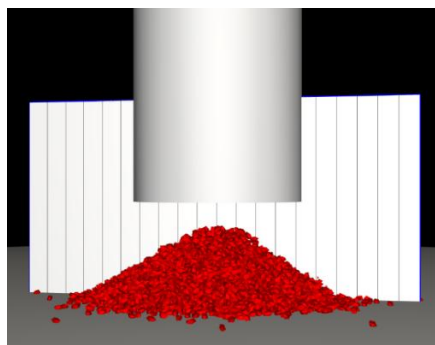

Fig.4.26. Sectors defined for statistical analysis

The sectors were rotating around the centre of the bottom plate, allowing to analyse the whole 3D structure of the heap, finding the average of the maximal vertical coordinates. These maximal height values were plotted as a function of radial distance to produce a height–radius envelope of the heap.

A conical angle was then fitted to the resulting profile by linear regression of either: the outermost lower slope region (yielding φ_{bottom}), or the upper portion near the apex (yielding φ_{top}). I used the results from the lower slope analysis φ_{bottom} (Fig. 4.27).
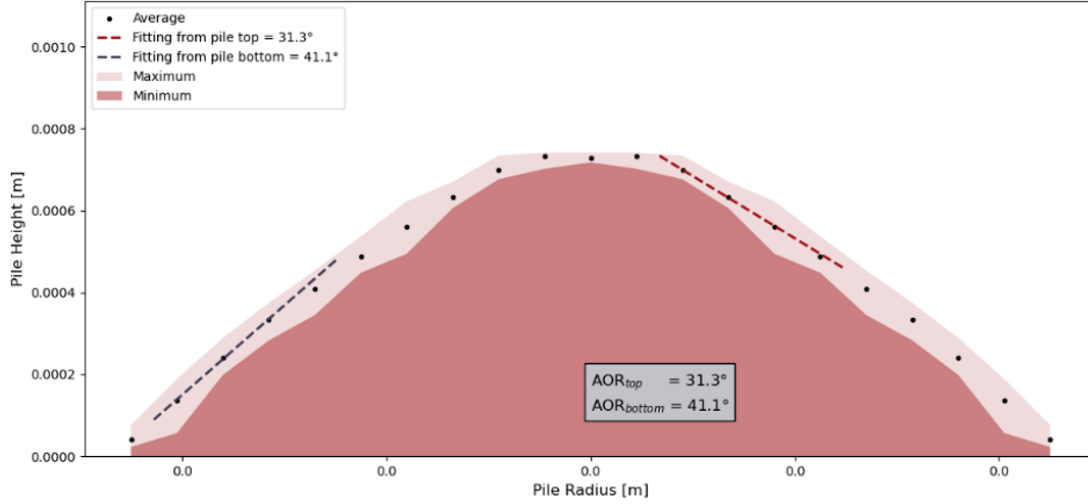

Fig.4.27. Angle of repose test result example

An example result is shown in Fig. 4.27, where the two regression slopes yielded angles of $31.3°$ (top) and $41.1°$ (bottom), respectively. The shaded envelope represents the local minimum and maximum points in each sector.

This method allows robust statistical estimation of the heap geometry, accounting for surface roughness and asymmetry. It was applied consistently across all simulations to determine the angle of repose as a function of interparticle friction.

To move beyond case-specific calibration and toward a predictive framework, particular emphasis was placed on identifying functional relationships between the angle of repose and the underlying micromechanical parameters of the assembly. Two parameters were selected as primary drivers: the static interparticle friction coefficient and the adhesive surface energy density. Friction was varied across a wide range to capture the transition from nearly frictionless flow to strongly interlocked packings, while adhesion was introduced as an effective surrogate for the angularity and electrostatic interactions of lunar dust. For each parameter sweep, the resulting heap geometries were statistically evaluated, and candidate mathematical forms were tested to describe the observed trends. The analysis revealed that the repose angle increases with friction in a nonlinear saturating manner, well captured by a logistic expression, while the dependence on adhesive energy is essentially linear within the studied range. These complementary functional forms provide not only accurate interpolation within the present data but also a transferable basis for calibrating DEM models with different particle morphologies or simulant batches, thereby extending the practical utility of the present findings.

The simulated angle of repose of granular assemblies was systematically analysed as a function of the interparticle static friction coefficient. The results demonstrated that the relationship is nonlinear and exhibits a saturating behaviour, which is well approximated by a logistic function of the form (Fig. 4.28):

$$\varphi(\mu_0) = \frac{L}{1+e^{-k(\mu_0-\mu_i)}} + \varphi_0 \tag{4.1}$$

96

This expression captures the essential mechanical behavior of granular materials,

Where:

$\varphi(\mu_0)$ Angle of repose

μ_0 Interparticle static friction coefficient

$L = 41,22°$ Maximal increase in angle attributable to frictional effects

$k = 6.11$ Characterizes the sensitivity of the angle to changes in friction

$\mu_i = 0.12$ Inflection point indicating the most responsive friction range

$\varphi_0 = 1.88°$ Base angle of repose in the hypothetical limit of zero friction

$$\varphi(\mu) = \frac{41.22}{1 + e^{-6.11(\mu - 0.12)}} + 1.88$$
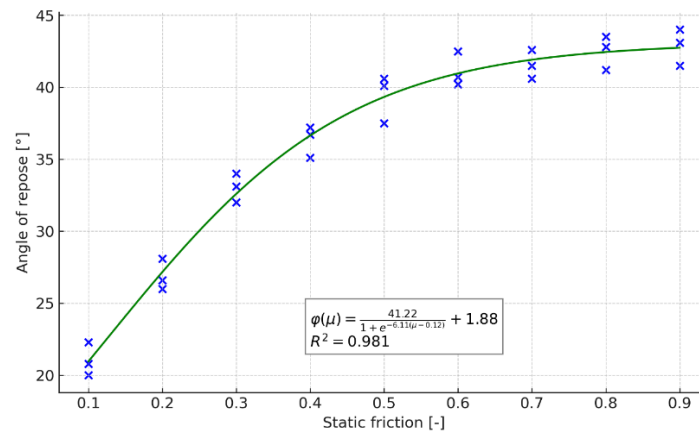$$R^2 = 0.981$$

Fig.4.28. Angle of repose as a function of the interparticle static friction coefficient.

From a physical standpoint, the logistic shape reflects the following mechanisms:

- At low friction levels ($\mu_0 \ll \mu_i$), the granular material is highly mobile, and small increases in friction lead to sharp increases in the angle of repose.

- Near the inflection point ($\mu_0 \approx \mu_i$), the system is most sensitive, corresponding to the regime where particle rearrangements and geometric interlocking start to significantly influence macroscopic stability.

- At high friction levels ($\mu_0 \gg \mu_i$), further increases in friction result in diminishing gains in the angle of repose, as the system approaches a geometric or structural stability limit governed by particle shape, packing density, and force chain architecture.

The high coefficient of determination ($R^2 = 0.981$) confirms the logistic model's suitability and indicates that friction alone can explain the majority of variance in the observed repose angles under the present simulation conditions.

This result suggests that the friction–repose angle relationship is governed not by a linear or purely empirical correlation, but by an emergent response of the granular system that reflects underlying micromechanical transitions and stability constraints. As such, the logistic model offers both predictive accuracy and physical interpretability, making it a robust choice for modelling granular repose behaviour in DEM simulations and constitutive modelling.

In the context of lunar regolith modelling, understanding the interplay between particle morphology and interparticle forces is crucial for reproducing the mechanical behaviour

observed in actual lunar soil. Due to the technical limitations of DEM shape representation, the simulated particles — although non-spherical — are not as angular and complex as real lunar dust grains, which often exhibit highly irregular, fragment-like geometries.

To compensate for this geometric simplification and capture the mechanical interlocking observed in lunar regolith, interparticle adhesion was introduced as an effective surrogate mechanism. By tuning the adhesive surface energy, I aimed to mimic the effects of angular entanglement and contact-level attraction that occur naturally in the actual regolith.

In this sensitivity analysis, the static friction coefficient was fixed at 0.1 — representing a low-friction baseline — while the adhesive surface energy was varied in the range of 0.01 to 0.1 mJ/m². All other particle and material properties remained unchanged. The resulting heap formations were analysed using the same statistical evaluation method described earlier.
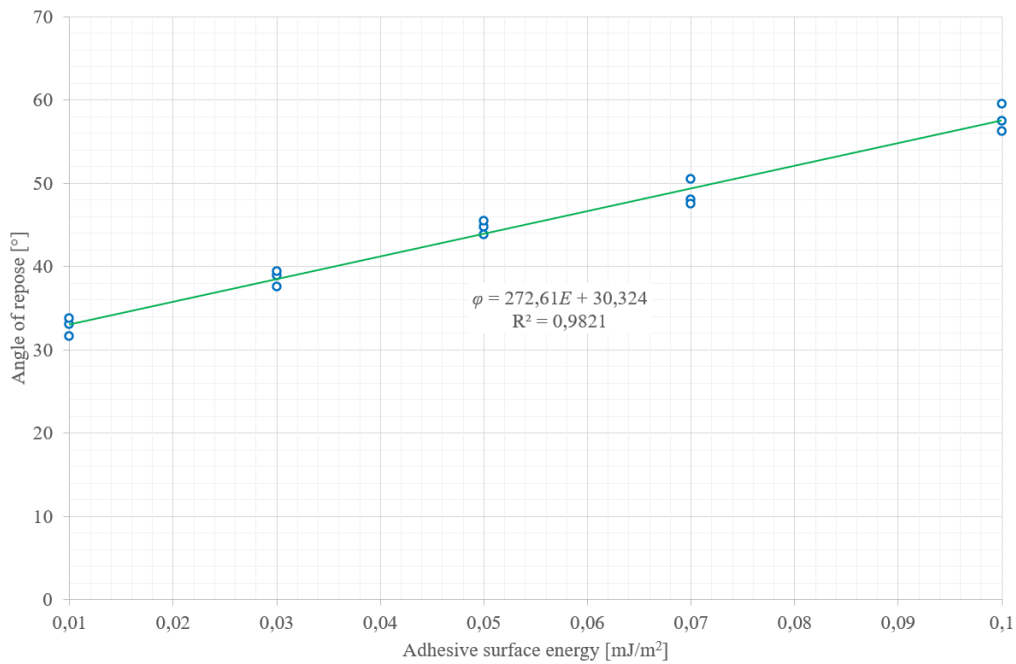

Fig.4.29. Angle of repose as a function of adhesive surface energy

The results, illustrated in the figure above, show a clear linear correlation between the adhesive energy and the angle of repose (Fig. 4.29):

$$\varphi = 272.61 \cdot E + 30.32 \quad (R^2 = 0.9821) \tag{4.2}$$

Where:

φ Angle of repose

E Adhesive surface energy

$R^2 = 0.9821$ High coefficient of determination

This trend confirms that surface-level adhesion can significantly increase bulk heap stability in systems where interparticle friction alone is insufficient. The enhanced angle of repose is attributed to the increased contact persistence and attractive force across particle boundaries, effectively simulating entanglement and inhibiting particle slippage along the pile surface.

From a lunar soil modelling perspective, this behaviour aligns with empirical observations: lunar regolith exhibits unusually high cohesion and steep natural slopes, owing to the combined

98

effects of extreme angularity, electrostatic interactions, and vacuum-sintered contact surfaces. While my model does not resolve these phenomena directly, the use of adjustable adhesive energy offers a practical and computationally tractable surrogate for incorporating these effects into DEM simulations.

This finding also reinforces the importance of cohesive interactions in shaping the macroscopic behaviour of lunar regoliths and suggests that tunable adhesion can serve as a key parameter in replicating realistic repose angles in granular space exploration studies.

4.4.3. Wear simulations

To bridge the calibrated bulk behaviour of the regolith simulants with the tribological wear measurements, a dedicated set of DEM simulations was performed to reproduce the pin-on-disc tests. To reduce the otherwise prohibitive computational demand, only a representative slice of the pin was modelled, while maintaining its characteristic contact area and material properties. This approach allowed me to capture the essential wear mechanisms without fully resolving the entire pin geometry (Fig. 4.30). The slice approach reduces computational demand while preserving representative contact conditions. Frictionless side walls were used to prevent the particles from leaving the simulation domain laterally. In the fig.4.30, only the rear wall is shown; an identical wall was also placed on the opposite side of the pin, but it was omitted from the visualization so as not to obscure the main features. The use of these walls was necessary because the application of periodic boundaries caused numerical instabilities in the wear model.
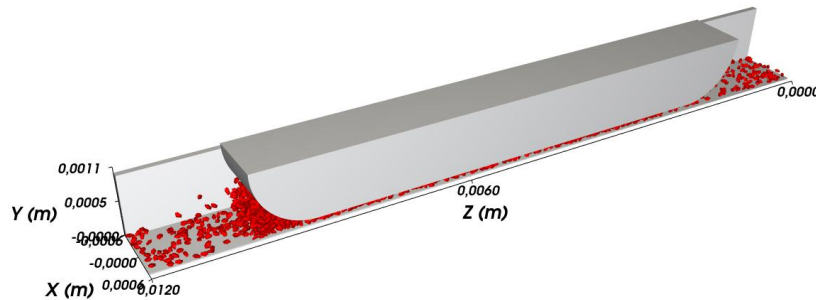

Fig.4.30. Simplified DEM model of the pin slice in contact with LHS-1 regolith particles.

The following material and interaction parameters were used in the wear simulations:

- Pin slice properties: triangular surface element size 9.67×10^{-5} m; mass 0.025 kg; calibrated wear coefficient 1.3×10^{-12} m^3/J.

- Pin material: density 2.1 g/cm³; Young's modulus 1.2 GPa; Poisson's ratio 0.4.

- Particle properties: bulk density 1300 kg/m³; Young's modulus 35 MPa; Poisson's ratio 0.25.

- Particle–particle interactions: static and dynamic friction 0.1; adhesive surface energy 0.028 mJ/m²; restitution coefficient 0.3.

- Particle–pin interactions: static and dynamic friction 0.5; adhesive surface energy 1×10^{-5} J/m²; restitution coefficient 0.3.

Based on the calibration results of the angle of repose, it was observed that different combinations of friction coefficient and adhesive surface energy can yield the same repose angle. Experimental observations further indicated that the simulant powder occasionally formed agglomerates and adhered to the surface of the pin. To account for this phenomenon in the numerical model, I adopted the approach of representing the regolith with a relatively low friction coefficient combined with an appropriately chosen adhesive surface energy.

To allow the pin to respond realistically to contact loading, vertical free body translation was enabled. To suppress excessive vibrations while maintaining realistic dynamics, a linear dashpot with a damping constant of 100 Ns/m was applied. Through this methodology, the DEM framework was extended from reproducing bulk heap behaviour to capturing tribological material removal, thereby establishing a direct numerical counterpart to the pin-on-disc wear experiments.

During the simulations, the vertical downward force and displacement of the pin were recorded as a function of accumulated sliding work. The force signal (Fig. 4.31) shows an initial transient during the onset of contact, followed by fluctuations around a stabilized mean value $F_y = 1,5\ N$ resulting the same pressure $p = 0,2$ MPa as it was applied during the measurements. After an initial transient phase, the load fluctuates around a stable mean value.
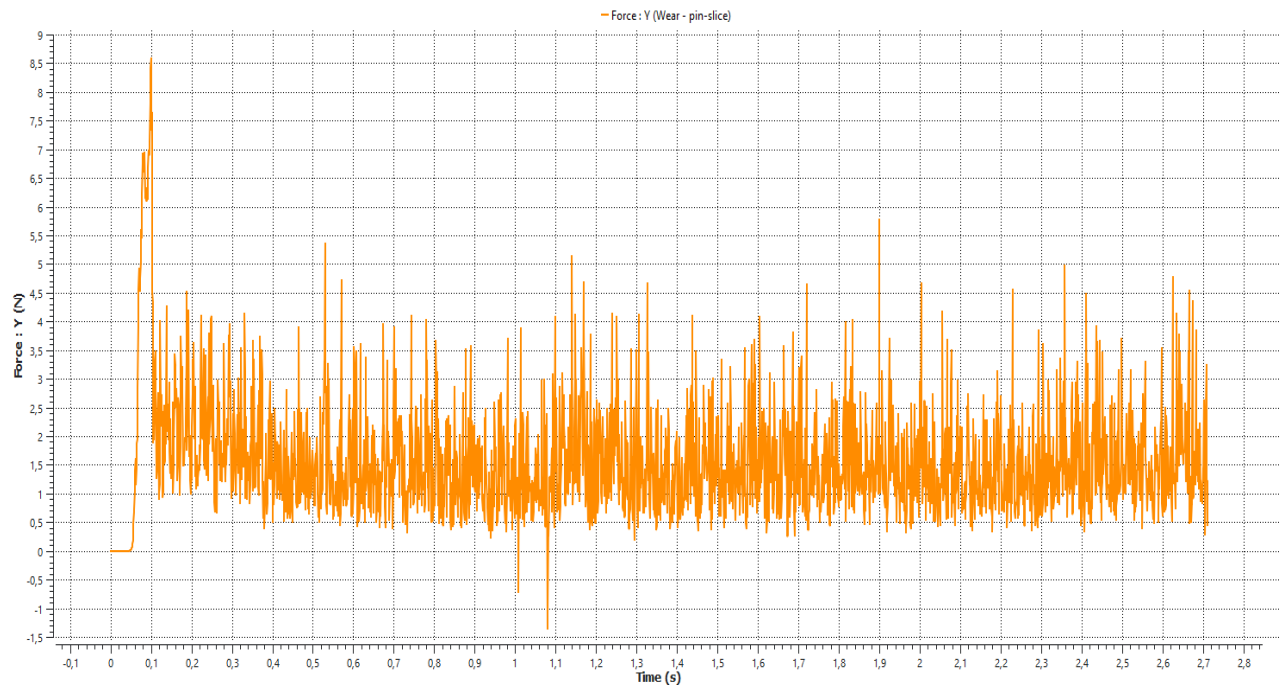

Fig.4.31. Vertical force acting on the pin slice as a function of time.

The corresponding vertical velocity response (Fig.4.32) confirms the presence of initial oscillations, which were subsequently damped by the applied 100 Ns/m dashpot. The initial oscillations are damped by the applied dashpot, ensuring stable simulation conditions.
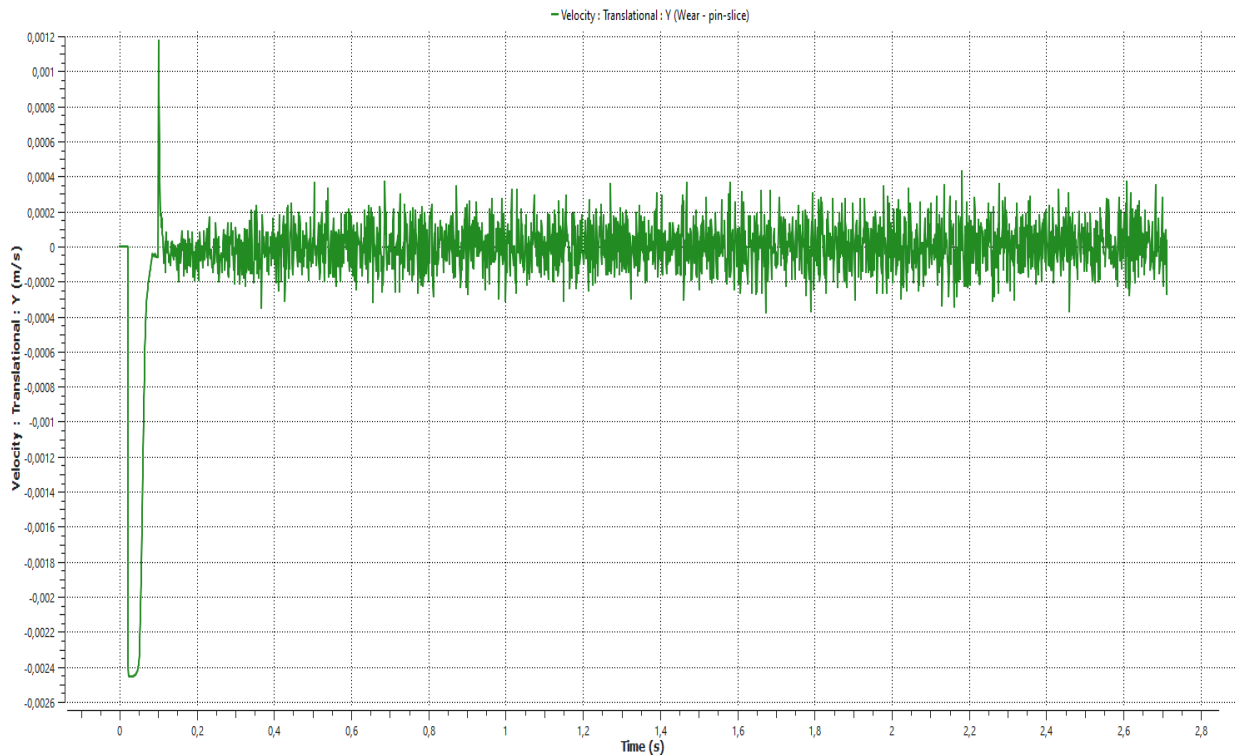
Fig.4.32.Vertical translational velocity of the pin slice.

After this stabilization phase, the displacement signal was interpreted as the effective wear penetration of the specimen. For simplicity, it was assumed that the wear was uniformly distributed over the surface of the original pin, and under this assumption the measured displacement was converted into a volumetric material loss for the complete specimen.

The simulation framework also allowed direct determination of volume loss: the worn geometry of the pin slice was exported, and its volume change was evaluated using Meshmixer software. A parametric procedure was then applied to identify the wear coefficient. The coefficient was systematically varied in the simulations until the predicted volumetric loss for 1m wear displacement ($2,5 \cdot 10^{-3}$ mm) matched that observed experimentally. This calibration yielded a wear coefficient $k = 1.688 \cdot 10^{-3}$ mm^3/J expressed as the ratio of volume loss to accumulated shear work, thereby linking microscopic tribological processes to macroscopic material degradation.

As demonstrated in Fig.4.33, the systematic calibration procedure revealed that, across several orders of magnitude, the wear coefficient and the corresponding worn-out material thickness exhibit a clear linear correlation. The results demonstrate a linear relationship across several orders of magnitude (R^2=0.9998), confirming the robustness of the calibration procedure and enabling the potential use of accelerated wear modelling approaches. This proportionality not only confirms the consistency of the wear model but also provides a practical advantage: it enables reliable interpolation of wear behaviour in cases where further calibration procedures are required. Moreover, the observed linearity offers the possibility of applying accelerated wear modelling methodologies, since simulations conducted with "real-life" material and interaction parameters are computationally highly demanding.
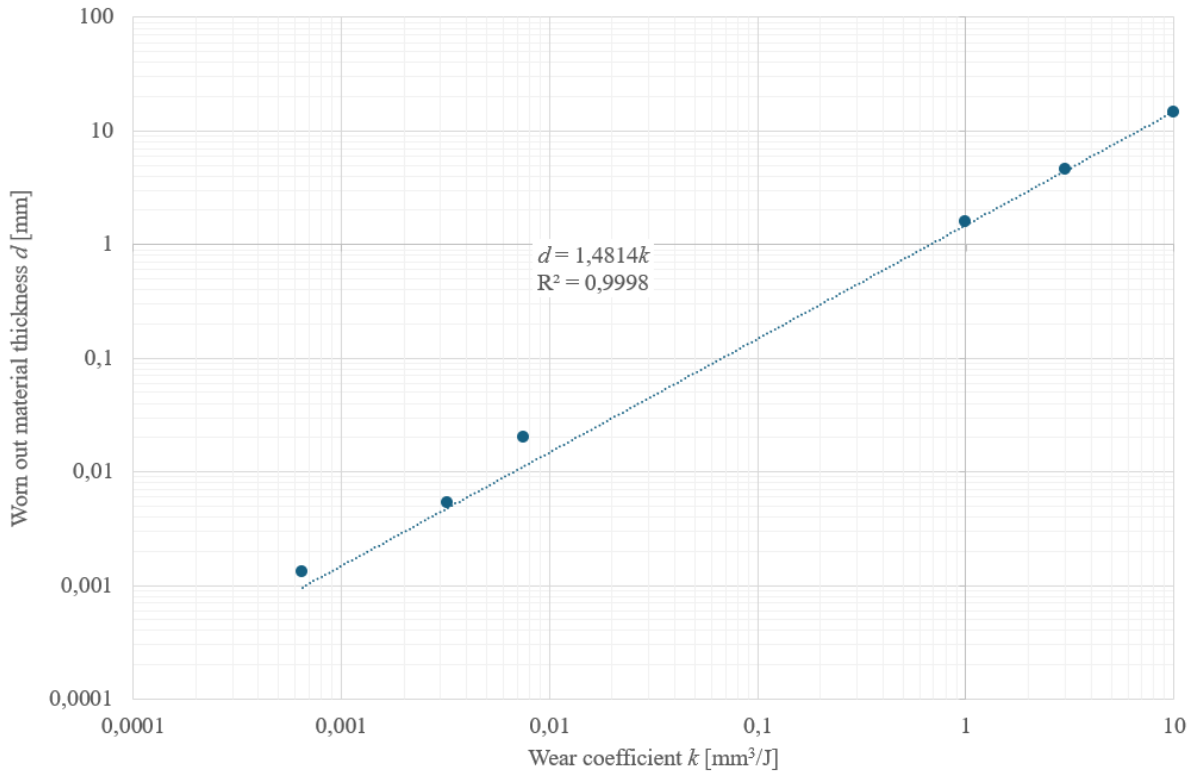
101

Fig.4.33. Correlation between the wear coefficient k and the worn-out material thickness d

The wear simulations calibrated with the LHS-1 highland regolith simulant established a robust scaling law between the wear coefficient and the worn-out material thickness. Across four orders of magnitude, the relationship is strictly linear, as expressed by the regression equation:

$$d = 1.4814k \tag{4.3}$$

Where:

d Worn-out material thickness

R^2 Coefficient of determination, $R^2 = 0.9998$

k Wear coefficient

This correlation confirms that the volumetric wear of the pin can be reliably predicted from the applied wear coefficient and vice versa.

From a methodological standpoint, this result provides two important advantages. First, it ensures that DEM-based wear models can be calibrated directly to experimental measurements with high confidence. Second, the established proportionality enables the use of accelerated wear modelling techniques: by artificially increasing the wear coefficient in simulations and subsequently rescaling the results using the regression law, computationally expensive simulations with real mechanical parameters can be effectively bypassed. Given the significant cost of resolving wear processes with the true Young's modulus of regolith particles, this scaling relation represents a novel and practically valuable scientific result, extending the predictive capability of DEM wear modelling in the context of extra-terrestrial soil interactions.

5. NEW SCIENTIFIC RESULTS

1. With my experimental measurements, I confirmed that both the LHS1 and LMS1 lunar regolith simulants induce a third-body abrasive wear mechanism for the stainless steel and PTFE pairing. This process is characterized by particle embedment and dynamic friction processes (steady state) after the running-in phase. Through on-line measurements and detailed post-test analyses (SEM, EDX, 3D surface topography), the study confirmed that both simulants induce third-body abrasive wear, but their distinct compositions result in significant differences in friction and wear kinetics and a linear wear trend developed, consistent with the Rabinowicz and Hutchings wear-model. The LMS1 particles, entering the contact zone after a longer sliding path, formed a 200-250% thicker regolith layer between the PTFE and stainless steel (Ss) surfaces. The resulting steady-state wear phase is also linear, but steeper compared to the LHS1.

2. Based on my experiments, analysing the Dp (Degree of Penetration) values, I highlighted that the LHS1 and LMS1 regoliths induce different abrasive micro-mechanisms. On the stainless steel (Ss) disc, I observed low Dp values for both regoliths (LHS1: 0.043-0.052; LMS1: 0.024-0.044), which indicates the dominance of micro-ploughing. This suggests that the particles partially embed into the steel's micro-geometry, plastically deforming the steel and reducing the surface roughness. In contrast, on the PTFE pin, the Dp values are higher and show a significant difference. For the LHS1, the Dp values (0.197-0.244) indicate a mixed wear mechanism where micro-ploughing and micro-cutting are in balance. However, the LMS1 regolith, due to its higher ilmenite and pyroxene content, causes more aggressive micro-cutting—in line with the wear curve—which is supported by the exceptionally high Dp value (R6: 0.372). This phenomenon can be traced back to the more intensive material removal caused by the harder LMS1 particles. Through the Dp metric, I proved that the different mineral compositions of the regoliths fundamentally influence the nature of the abrasive mechanisms on both hard and softer surfaces.

3. From DEM modelling, I established functional relationship between interparticle friction and the angle of repose. The relationship between the angle of repose (φ) and the interparticle static friction coefficient (μ_0) was found to follow a logistic-type saturation law of the general form

$$\varphi(\mu_0) = \frac{L}{1 + e^{-k(\mu_0 - \mu_i)}} + \varphi_0 \, .$$

For the simulated polyhedral lunar regolith assembly, the fitted parameters were: $L = 41{,}22°$ maximal increase in angle attributable to frictional effects, $k = 6.11$ the sensitivity of the angle to changes in friction, $\mu_i = 0.12$ inflection point indicating the most responsive friction range, $\varphi_0 = 1.88°$ base angle of repose in the hypothetical limit of zero friction. The model accurately describes the data over the range $0 \leq \mu \leq 0.8$ with a coefficient of determination $R^2 = 0.981$. This functional form captures the transition from highly mobile, low-friction particle systems to geometrically constrained, high-friction packings and provides a physically interpretable constitutive law for regolith heap stability.

4. Using DEM I set the dependence of the angle of repose on adhesive surface energy. At a constant friction level, the angle of repose (φ) increases linearly with the adhesive surface energy (E), expressed generally as

$$\varphi = a \cdot E + b$$

Where: $a = 272.61 \, \frac{\text{degree}}{\text{mJ}}$, $b = 30.32°$, yielding an excellent correlation with $R^2 = 0.9821$ over the range $0.01 \leq E \leq 0.1 \, \frac{\text{mJ}}{\text{m}^2}$. This result demonstrates that adhesion effectively reproduces the enhanced bulk stability typical of cohesive and angular regoliths, providing a practical surrogate parameterization for electrostatic and vacuum-sintered interparticle bonding effects in DEM simulations.

5. I concluded the relation between wear coefficient and worn material thickness for LHS-1 simulant. The DEM-based wear calibration performed with the LHS-1 lunar highland simulant revealed a linear scaling law between the wear coefficient (k) and the resulting worn-out material thickness (d) of the general form

$$d = c \, k.$$

The regression analysis yielded $c = 1.4814 \, \text{Jmm}^{-2}$ with a coefficient of determination $R^2 = 0.9998$, valid within the range $10^{-13} \leq k \leq 10^{-9} \text{m}^3\text{J}^{-1}$. This linearity confirms the direct proportionality between the wear coefficient and the total material loss, enabling the use of accelerated wear simulations where artificially increased k values can be employed and rescaled through the established relation. The result provides a transferable quantitative tool for predicting regolith-induced wear on polymeric materials under lunar surface conditions.

In conclusion, the combined experimental and numerical investigations have provided a comprehensive understanding of the tribological behaviour and bulk mechanical response of lunar regolith simulants, linking micromechanical processes to macroscopic system performance. The experimental results demonstrated that the mineral composition and microstructure of the LHS-1 and LMS-1 simulants fundamentally determine their frictional, wear, and abrasive mechanisms. The complementary DEM simulations extended these findings by establishing functional relationships between the governing material and interaction parameters—interparticle friction, adhesive surface energy, and wear coefficient—and the resulting macroscopic responses, namely the angle of repose and the volumetric material loss. Together, these results form a coherent and quantitatively validated framework that not only elucidates the physical mechanisms of regolith-induced wear but also provides transferable constitutive and scaling laws for future modelling efforts. The integration of calibrated DEM models with experimental observations thus represents a significant methodological advancement toward predictive simulation of extra-terrestrial soil–material interactions under realistic operating conditions.

6. CONCLUSIONS AND PROPOSALS

My study provided a comprehensive tribological evaluation of stainless steel (1.4404) and natural PTFE contact pairs exposed to two lunar regolith simulants (LHS1 and LMS1), supported by extensive microscopy, 3D topography, elemental analysis, and DEM-based numerical modelling. The experimental results revealed that both simulants produce a characteristic three-body abrasive mechanism, initiated after an adhesive PTFE–steel run-in phase and sustained by the dynamic ingress, embedment, and rolling of mineral particles within the contact zone.

For both simulants, the stainless-steel counterface exhibited a dominant micro-ploughing mechanism, confirmed by low Dp values (<0.1), progressive groove formation, and increasing particle embedment. In contrast, the PTFE pins experienced a mixed wear mechanism of micro-ploughing and micro-cutting, where embedded grains acted as cutting tools and produced deep, directional abrasive grooves with increasing sliding distance. LMS1 consistently produced greater friction, higher wear rate, and more severe micro-cutting than LHS1, indicating its higher abrasivity and dynamic instability.

Numerical simulations successfully reproduced bulk particle behaviour and provided a calibrated DEM model capable of predicting changes in angle of repose as a function of interparticle friction and cohesion. Furthermore, the DEM wear framework demonstrated its applicability for reproducing micro-scale abrasive interactions, establishing a transferable modelling workflow adaptable to other extra-terrestrial soils such as Martian dust. This dual experimental-numerical approach forms a robust foundation for predicting component longevity and designing abrasion-resistant mechanisms for planetary surface operations.

Proposals

- Improve sealing materials for lunar environments:
Based on severe micro-cutting observed on PTFE, alternative materials such as filled PTFE composites, polyimides, or reinforced elastomers should be tested to reduce material removal and extend component life.
- Applications of engineered surface treatments on steel counterfaces:
Hard coatings (DLC, nitriding, ceramic PVD layers) or texturing strategies may reduce particle embedment and micro-ploughing. Surface engineering should be explored using the DEM wear model prior to prototyping.
- Optimize seal/shaft geometries through DEM-based pre-screening:
Since DEM wear simulations reproduce regolith interactions at the particle level, they should be used to evaluate contact pressure, track curvature, and groove geometry before manufacturing large-scale test hardware.
- Extend abrasion studies to vacuum and thermal-cycling conditions:
Lunar surface mechanisms operate under extreme temperatures and near-vacuum, which affect PTFE deformation, regolith adhesivity, and third-body dynamics. Replicating these conditions will improve prediction accuracy.
- Investigate multi-particle size distributions and long-duration wear
Real regolith contains extreme fines (<20 µm) and sharp agglutinates, which likely intensify wear beyond the simulants tested. Incorporating fines into experiments and simulations will create more realistic abrasive conditions.

7. SUMMARY

This dissertation, "Experimental and DEM model of abrasion of rotary shaft/seal contact with lunar regolith simulants," addresses the critical challenge of abrasive wear in machinery designed for extra-terrestrial environments, focusing specifically on the highly destructive nature of lunar regolith. The core objective was to develop and validate a robust modelling framework by integrating empirical data from coupon-scale tribological tests with advanced Discrete Element Method (DEM) numerical simulations.

The experimental phase utilized a Pin-on-Disc (PoD) setup to simulate the sliding contact between a stainless steel (SS) disc and a Polytetrafluoroethylene (PTFE) pin, representing a typical shaft/seal interface. The abrasive media consisted of two distinct mineralogical simulants: LHS1 (Anorthosite-rich, Lunar Highland Simulant) and LMS1 (harder, Ilmenite/Pyroxene-rich, Lunar Mare Simulant). Through on-line measurements and detailed post-test analyses (SEM, EDX, 3D surface topography), the study confirmed that both simulants induce third-body abrasive wear, but their distinct compositions result in significant differences in friction and wear kinetics. The softer LHS1 led to a milder tribological response, while the harder LMS1 formed a 200–250% thicker regolith layer and caused higher local friction instabilities. A key finding was the distinction in abrasive micro-mechanisms: the wear on the hard SS disc was dominated by micro-ploughing for both simulants, whereas on the soft PTFE pin, LHS1 induced a mixed wear mechanism (ploughing and cutting), and the aggressive LMS1 caused significantly more detrimental micro-cutting, quantifiable by the exceptionally high Degree of Penetration metric (Dp up to 0.372).

New scientific results emerged from the development of the numerical model. The DEM framework was calibrated by establishing a non-linear logistic relationship (R^2=0.981) between the Angle of Repose (AoR) and the interparticle friction coefficient, allowing for a transferable calibration framework applicable to various regolith simulant batches. Crucially, the DEM simulation established a direct proportionality between volumetric material loss and shear work input for the PTFE specimen. This novel relationship allows for accelerated wear modelling, where researchers can artificially increase the wear coefficient in the simulation and rescale the results, effectively bypassing the enormous computational expense associated with using the actual, high Young's modulus of regolith particles. In conclusion, the research successfully quantified the differential abrasive behaviour of two key lunar regolith types and delivered a validated, computationally efficient DEM-based predictive tool for designing more resilient shaft/seal systems for future deep-space exploration missions.

8. ACKNOWLEDGEMENT

9. DECLARATION ON THE USE OF ARTIFICIAL INTELLIGENCE

I hereby declare that the research and intellectual content of this dissertation are my own original work, under the guidance of my supervisors and sometimes in collaboration with a research team, except where explicitly noted. The core intellectual contributions, including the research questions, data collection, analysis, and interpretation, are entirely my responsibility.

Specific Use of Artificial Intelligence (AI) Software

AI software: Gemini 2.5 Flash, Chat GPT was used exclusively to refine language and expression: Act as an advanced language polishing and editing aid to enhance the clarity, fluency, and professional English expression of the final written text. This included correcting grammar, improving sentence structure, and suggesting precise terminology.

Exclusion of AI in Content Generation

I confirm that AI software **was not used** for:

- Generating any original research ideas, hypotheses, or theoretical frameworks.
- Creating or modifying the core content, including the literature review, methodology, results, or discussion sections.
- Any form of data collection, manipulation, or interpretation.
- The creation or modification of figures, tables, or graphical elements.

The substance and intellectual originality of this dissertation remain my sole responsibility, supported by my supervisors' guidance.

Signature:

Date:

10.REFERENCES

Aela, P., Zong, L., Esmaeili, M., Siahkouhi, M., & Jing, G. (2022). Angle of repose in the numerical modeling of ballast particles focusing on particle-dependent specifications: Parametric study. *Particuology*, *65*, 39–50. https://doi.org/10.1016/j.partic.2021.06.006

Ai, J., Chen, J. F., Rotter, J. M., & Ooi, J. Y. (2011). Assessment of rolling resistance models in discrete element simulations. *Powder Technology*, *206*(3), 269–282. https://doi.org/10.1016/j.powtec.2010.09.030

Ajmal, M., Roessler, T., Richter, C., & Katterfeld, A. (2020). Calibration of cohesive DEM parameters under rapid flow conditions and low consolidation stresses. *Powder Technology*, *374*, 22–32. https://doi.org/10.1016/j.powtec.2020.07.017

Angerhausen, J., Woyciniuk, M., Murrenhoff, H., & Schmitz, K. (2019). Simulation and experimental validation of translational hydraulic seal wear. *Tribology International*, *134*(November 2018), 296–307. https://doi.org/10.1016/j.triboint.2019.01.048

B. Arkwright, P. Buchele, and P. D. L. (1999). Development of a modular two-axis gimbal mechanism for spacecraft antenna and thruster pointing. *Space Mechanism and Tribology, Proceedings of the 8th European Symposium, Held 29 September-1 October, 1999 in Toulouse, France. Edited by D. Danesy. European Space Agency, ESA-SP, 438*, 213.

Bark, G., Keresztes, R., & Shegawu, H. (2023). Abrasion Evaluation of Moon and Mars Simulants on Rotating Shaft / Sealing Materials : Simulants and Structural Materials Review and Selection. *Lubricants 2023, 11, 334.* https://doi.org/10.3390/lubricants11080334

Blau, P. J. (2016). *Friction Science and Technology* (SECOND). CRC PRESS.

Bühler, C. A. (2015). Experimental investigation of lunar dust impact wear. *Wear*, *342–343*, 244–251. https://doi.org/10.1016/j.wear.2015.09.002

Bushan, B. (2001). Modern Tribology handbook. In *Modern Tribology handbook*. CRC Press LLC.

Campello, E. M. B. (2018). A computational model for the simulation of dry granular materials. *International Journal of Non-Linear Mechanics*, *106*(August), 89–107. https://doi.org/10.1016/j.ijnonlinmec.2018.08.010

Cannon, K. M., Britt, D. T., Smith, T. M., Fritsche, R. F., & Batcheldor, D. (2019). Mars global simulant MGS-1: A Rocknest-based open standard for basaltic martian regolith simulants. *Icarus*, *317*(July 2018), 470–478. https://doi.org/10.1016/j.icarus.2018.08.019

Coetzee, C. J. (2017). *Review : Calibration of the discrete element method. 310*, 104–142. https://doi.org/10.1016/j.powtec.2017.01.015

Daneshmand, H., Jafari Eskandari, M., & Araghchi, M. (2023). Reinforced PTFE composites with atomized powder of Inconel 625 alloy for sealing application: Study of structural properties and molecular dynamics simulation. *Materials Today Communications*, *35*(June), 106413. https://doi.org/10.1016/j.mtcomm.2023.106413

Delgado, I. R., & Handschuh, M. J. (2010). Preliminary Assessment of Seals for Dust Mitigation of Mechanical Components for Lunar Surface Systems. *Nasa/Cp-2010-*

216272, *June*, 309–316.

Dotson, B., Sanchez Valencia, D., Millwater, C., Easter, P., Long-Fox, J., Britt, D., & Metzger, P. (2024). Cohesion and shear strength of compacted lunar and Martian regolith simulants. *Icarus*, *411*(January), 115943. https://doi.org/10.1016/j.icarus.2024.115943

Dougherty, S. (2003). Micro-imager dust cover, micro-imager contact sensor, and mössbauer spectrometer contact sensor mechanisms for the mars exploration rovers. *In European Space Agency, (Special Publication) ESA SP, 2003, 524*(Mi), 73–80. https://ui.adsabs.harvard.edu/abs/2003ESASP.524...73D/abstract.

exolithsimulants. (2020). *About our lunar simulants*. https://exolithsimulants.com/

Farfán-Cabrera, L. I., Gallardo-Hernández, E. A., de la Rosa, C. S., & Vite-Torres, M. (2017). Micro-scale abrasive wear of some sealing elastomers. *Wear*, *376–377*, 1347–1355. https://doi.org/10.1016/j.wear.2017.02.004

Farfán-Cabrera, L. I., Gallardo-Hernández, E. A., Pascual-Francisco, J. B., Resendiz-Calderon, C. D., & Sedano De La Rosa, C. (2016). Experimental method for wear assessment of sealing elastomers. *Polymer Testing*, *53*, 116–121. https://doi.org/10.1016/j.polymertesting.2016.04.021

Frölich, D., Magyar, B., & Sauer, B. (2014). A comprehensive model of wear , friction and contact temperature in radial shaft seals. *Wear*, *311*(1–2), 71–80. https://doi.org/10.1016/j.wear.2013.12.030

Galary, J. (2018). Rolling Wear and Fatigue in Lubricated Contacts. *University of Massachusetts at Dartmouth*.

Gewehr, M., Schneider, A., Dalcolmo, J., Klinkner, S., & Gmbh, S. (2021). Design and testing of a novel miniaturised sealed tether-recoil mechanism for the nanokhod microrover. *Esmats-2021*, *1*.

Gong, R., Liu, M., Zhang, H., & Xu, Y. (2015). Experimental investigation on frictional behavior and sealing performance of different composites for seal application. *Wear*, *342–343*, 334–339. https://doi.org/10.1016/j.wear.2015.10.001

Grandy, D., Panek, N., Routhier, G., & Ridolfi, P. (2019). *DEVELOPMENT AND QUALIFICATION OF THE EXOMARS BOGIE ELECTRO-MECHANICAL ASSEMBLY (BEMA) ROTARY ACTUATORS*. *c*(September).

Grasser, D., Corujeira Gallo, S., Pereira, M. P., & Barnett, M. (2024). Wear simulation and validation of composites (insert-reinforced matrix) in the dry sand rubber wheel test. *Minerals Engineering*, *207*(November 2022), 108583. https://doi.org/10.1016/j.mineng.2024.108583

Hokkirigawa, K., & Kato, K. (1988). An experimental and theoretical investigation of ploughing, cutting and wedge formation during abrasive wear. *Tribology International*, *21*(1), 51–57. https://doi.org/10.1016/0301-679X(88)90128-4

Hou, X., Ding, T., Chen, T., Liu, Y., Li, M., & Deng, Z. (2019). Constitutive properties of irregularly shaped lunar soil simulant particles. *Powder Technology*, *346*, 137–149. https://doi.org/10.1016/j.powtec.2019.02.012

Huang, T. C., Lin, C. Y., & Liao, K. C. (2022). Sealing performance assessments of PTFE rotary lip seals based on the elasto-hydrodynamic analysis with the modified archard wear

model. *Tribology International*, *176*(September), 107917. https://doi.org/10.1016/j.triboint.2022.107917

Huang, T. C., Lin, C. Y., & Liao, K. C. (2023). Experimental and numerical investigations of the wear behavior and sealing performance of PTFE rotary lip seals based on the elasto-hydrodynamic analysis with considerations of the asperity contact. *Tribology International*, *187*(June), 108747. https://doi.org/10.1016/j.triboint.2023.108747

Iliescu, D., Gehin, D., Iordanoff, I., Girot, F., & Gutiérrez, M. E. (2010). A discrete element method for the simulation of CFRP cutting. *Composites Science and Technology*, *70*(1), 73–80. https://doi.org/10.1016/j.compscitech.2009.09.007

Jandura, L. (2010). Mars Science Laboratory Sample Acquisition, Sample Processing and Handling: Subsystem Design and Test Challenges. *Proceedings of the 40th Aerospace Mechanisms Symposium*, 233–248.

Jiang, Q., & Xie, C. (2023). A coupled discrete-finite element model for bulk materials transfer simulation and PDSS structural wear prediction. *Energy Reports*, *9*, 6–14. https://doi.org/10.1016/j.egyr.2022.11.158

Jiménez-Herrera, N., Barrios, G. K. P., & Tavares, L. M. (2018). Comparison of breakage models in DEM in simulating impact on particle beds. *Advanced Powder Technology*, *29*(3), 692–706. https://doi.org/10.1016/j.apt.2017.12.006

Kalácska, G., Barkó, G., Shegawu, H., Kalácska, Á., Zsidai, L., Keresztes, R., & Károly, Z. (2024). The Abrasive Effect of Moon and Mars Regolith Simulants on Stainless Steel Rotating Shaft and Polytetrafluoroethylene Sealing Material Pairs. In *Materials* (Vol. 17, Issue 17). https://doi.org/10.3390/ma17174240

Kalapodis, N., Kampas, G., & Ktenidou, O. J. (2020). A review towards the design of extraterrestrial structures: From regolith to human outposts. *Acta Astronautica*, *175*(March), 540–569. https://doi.org/10.1016/j.actaastro.2020.05.038

Kanji, S., & Buratynsky, M. (2019). CHALLENGES ASSOCIATED WITH TESTING MECHANISMS FOR A MARTIAN ENVIRONEMENT. *ESMATS - 18th European Space Mechanisms and Tribology Symposium*, *September*.

Katinas, E., Chotěborský, R., Linda, M., & Kuře, J. (2021). Sensitivity analysis of the influence of particle dynamic friction, rolling resistance and volume/shear work ratio on wear loss and friction force using DEM model of dry sand rubber wheel test. *Tribology International*, *156*(January). https://doi.org/10.1016/j.triboint.2021.106853

Kato, K., & Adachi, K. (2001). Wear mechanisms. In *Modern Tribology Handbook* (pp. 273–300). CRC press.

Kobrick, R. L., Klaus, D. M., & Street, K. W. (2011). Defining an abrasion index for lunar surface systems as a function of dust interaction modes and variable concentration zones. *Planetary and Space Science*, *59*(14), 1749–1757. https://doi.org/10.1016/j.pss.2010.10.010

Kumar, R., Malaval, B., Antonov, M., & Zhao, G. (2020). Performance of polyimide and PTFE based composites under sliding, erosive and high stress abrasive conditions. *Tribology International*, *147*(February), 106282. https://doi.org/10.1016/j.triboint.2020.106282

Lamotte, E., Bozet, J.-L., & Kabuya, A. (2000). Modelling of friction and wear for cryogenic

valve seals of rocket engines,. *Techspace Aero.*

Lee, S. H., Yoo, S. S., Kim, D. E., Kang, B. S., & Kim, H. E. (2012). Accelerated wear test of FKM elastomer for life prediction of seals. *Polymer Testing*, *31*(8), 993–1000. https://doi.org/10.1016/j.polymertesting.2012.07.017

Leonard, B. D., Sadeghi, F., Shinde, S., & Mittelbach, M. (2013). Rough surface and damage mechanics wear modeling using the combined finite-discrete element method. *Wear*, *305*(1–2), 312–321. https://doi.org/10.1016/j.wear.2012.12.034

Li, L. J., Zhu, Q. X., Gou, D. Z., Chan, H. K., Kourmatzis, A., Zhao, G. T., & Yang, R. Y. (2022). DEM modelling of breakage behaviour of semi-brittle agglomerates subject to compaction and impaction. *Powder Technology*, *408*(July). https://doi.org/10.1016/j.powtec.2022.117710

Li, Y., Wang, T., Chen, S., Zhang, X., & Wang, Q. (2024). Dry friction thermal behavior and wear mechanism of polyurethane elastomer for main drive seal of TBM. *Tribology International*, *193*(October 2023), 109367. https://doi.org/10.1016/j.triboint.2024.109367

Lin Shenxing et al., 2005. (2005). E n g i n e e r i n g t r i b o l o g y. *Elsiever Butterworth-Heinemann*, *91*, 399–404.

Liu, X., Song, J., Chen, H., Zhao, G., Qiu, J., & Ding, Q. (2019). Enhanced transfer efficiency of ultrasonic motors with polyimide based frictional materials and surface texture. *Sensors and Actuators, A: Physical*, *295*, 671–677. https://doi.org/10.1016/j.sna.2019.06.033

Long-Fox, J. M., Landsman, Z. A., Easter, P. B., Millwater, C. A., & Britt, D. T. (2023). Geomechanical properties of lunar regolith simulants LHS-1 and LMS-1. *Advances in Space Research*, *71*(12), 5400–5412. https://doi.org/10.1016/j.asr.2023.02.034

Ludema, K. C. (1996). *Friction, Wear, Lubrication: Textbook in Tribology*. CRC press.

Luo, X., Zhao, L., & Dong, H. (2021). Study on DEM parameter calibration and wear characteristics of vanadium-titanium magnetite pellets. *Powder Technology*, *393*, 427–440. https://doi.org/10.1016/j.powtec.2021.07.077

McClendon, M. (2011). *NIRSpec MSS Magnet Actuator Life Test Unit Wear Particle Evaluation.*

Mpagazehe, J. N., Street, K. W., Delgado, I. R., & Fred Higgs, C. (2014). An experimental study of lunar dust erosive wear potential using the JSC-1AF lunar dust simulant. *Wear*, *316*(1–2), 79–91. https://doi.org/10.1016/j.wear.2014.04.018

Nakashima, H., Shioji, Y., Kobayashi, T., Aoki, S., Shimizu, H., Miyasaka, J., & Ohdoi, K. (2011). Determining the angle of repose of sand under low-gravity conditions using discrete element method. *Journal of Terramechanics*, *48*(1), 17–26. https://doi.org/10.1016/j.jterra.2010.09.002

Naser, M. Z., & Chehab, A. I. (2018). Materials and design concepts for space-resilient structures. *Progress in Aerospace Sciences*, *98*(March), 74–90. https://doi.org/10.1016/j.paerosci.2018.03.004

Neale, M. J. (1995). *The tribology handbook* (Second). Elsevier.

Ng, T. C., & Yung, K. L. (2010). Mars Rock Corer and Planetary Micro Sampling Tools. *Proceedings of the 33rd Lunar and Planetary Science Conference.*

Outokumpu. (2020). *Outokumpu datasheets*. https://www.outokumpu.com/

Peng, C., Miao, J., Bauer, N., & Schmitz, K. (2023). Investigation into the inter-lip characteristics of combined seals with double lips in different working conditions. *Tribology International*, *178*(PA), 108036. https://doi.org/10.1016/j.triboint.2022.108036

Perazzo, F., Löhner, R., Labbe, F., Knop, F., & Mascaró, P. (2019). Numerical modeling of the pattern and wear rate on a structural steel plate using DEM. *Minerals Engineering*, *137*(April), 290–302. https://doi.org/10.1016/j.mineng.2019.04.012

Provedo, B., Jaio, G., & Viñals, J. (2017). SEALING CAP FOR METIS INSTRUMENT IN SOLAR ORBITER FDM SUBSYSTEM. *ESMATS*, *September*, 20–22.

Qiao, Z., Guo, Y., Wei, R., Zhang, Z., Wang, B., & Wang, D. (2024). Comparative study on wear properties for rubber elastomers under different downhole condition. *Wear*, *548–549*(April 2023), 205380. https://doi.org/10.1016/j.wear.2024.205380

Qin, K., Zhou, Q., Zhang, K., Feng, Y., Zhang, T., Zheng, G. J., Xia, B., & Liu, B. (2019). Non-uniform abrasive particle size effects on friction characteristics of FKM O-ring seals under three-body abrasion. *Tribology International*, *136*(August 2018), 216–223. https://doi.org/10.1016/j.triboint.2019.03.051

Quattroplast. (2021). *quattro plastic*. https://quattroplast.hu/

Quinteros, V. S., Mikesell, T. D., Griffiths, L., & Jerves, A. X. (2024). Geotechnical laboratory testing of lunar simulants and the importance of standardization. *Icarus*, *408*(September 2023), 115812. https://doi.org/10.1016/j.icarus.2023.115812

Roberts, E. W., & Eiden, M. (2013). A space tribology handbook. *European Space Tribology Laboratory*.

Roessler, T., & Katterfeld, A. (2019). DEM parameter calibration of cohesive bulk materials using a simple angle of repose test. *Particuology*, *45*, 105–115. https://doi.org/10.1016/j.partic.2018.08.005

Rong, W., Qiu, L., Liu, Z., Li, B., & Qi, F. (2023). Numerical study on the abrasive wear of screw flights considering the scaffolding near the bustle pipe zone in a COREX shaft furnace. *Advanced Powder Technology*, *34*(6), 104037. https://doi.org/10.1016/j.apt.2023.104037

Shen, M. X., Dong, F., Zhang, Z. X., Meng, X. K., & Peng, X. D. (2016). Effect of abrasive size on friction and wear characteristics of nitrile butadiene rubber (NBR) in two-body abrasion. *Tribology International*, *103*, 1–11. https://doi.org/10.1016/j.triboint.2016.06.025

Shen, M. xue, Li, B., Li, S., Xiong, G. yao, Ji, D. hui, & Zhang, Z. nan. (2020). Effect of particle concentration on the tribological properties of NBR sealing pairs under contaminated water lubrication conditions. *Wear*, *456–457*(June). https://doi.org/10.1016/j.wear.2020.203381

Singh, K., Sadeghi, F., Correns, M., & Blass, T. (2019). A microstructure based approach to model effects of surface roughness on tensile fatigue. *International Journal of Fatigue*, *129*(June), 105229. https://doi.org/10.1016/j.ijfatigue.2019.105229

Stachowiak, G., & Batchelor, A. W. (2005). *Engineering tribology* (Third (ed.)). Elsevier.

Stachowiak, G. W., & Batchelor, A. W. (2015). *ENGINEERING TRIBOLOGY* (Four). Elsevier.

Sui, P. C., & Anderle, S. (2011). Optimization of contact pressure profile for performance improvement of a rotary elastomeric seal operating in abrasive drilling environment. *Wear*, *271*(9–10), 2466–2470. https://doi.org/10.1016/j.wear.2011.02.021

Sukumaran, A. K., Zhang, C., Nisar, A., Rengifo, S., & Agarwal, A. (2023). Tribological behavior of Al 6061 and Ti6Al4V alloys against lunar regolith simulants at extreme temperatures. *Wear*, *530–531*(March), 205028. https://doi.org/10.1016/j.wear.2023.205028

Tan, B., & Stephens, L. S. (2019). Evaluation of viscoelastic characteristics of PTFE-Based materials. *Tribology International*, *140*(July), 105870. https://doi.org/10.1016/j.triboint.2019.105870

Tan, D., Yang, Q., Yang, W., Hu, Y., He, Q., & Yang, X. (2025). Impact of friction speeds on the wear mechanisms of X-shaped nitrile rubber seals in oil-rich lubrication condition. *Wear*, *September 2024*, 205933. https://doi.org/10.1016/j.wear.2025.205933

Thompson, J. (2023). *Wear and impact analysis of granular materials using Discrete Element Method simulations*. June.

Thompson, J. A., Berry, L., Southern, S., Walls, W. K., Holmes, M. A., & Brown, S. G. R. (2022). The effect of mesh discretisation on damage and wear predictions using the Discrete Element Method. *Applied Mathematical Modelling*, *105*, 690–710. https://doi.org/10.1016/j.apm.2022.01.005

Wilson, B. (1998). Friction, Wear and Lubrication: A Textbook in Tribology. In *Industrial Lubrication and Tribology* (Vol. 50, Issue 5). https://doi.org/10.1108/ilt.1998.01850eae.001

Xiong, D., Qin, Y., Li, J., Wan, Y., & Tyagi, R. (2015). Tribological properties of PTFE/laser surface textured stainless steel under starved oil lubrication. *Tribology International*, *82*(PB), 305–310. https://doi.org/10.1016/j.triboint.2014.07.017

Xu, L., Luo, K., & Zhao, Y. (2018). Numerical prediction of wear in SAG mills based on DEM simulations. *Powder Technology*, *329*, 353–363. https://doi.org/10.1016/j.powtec.2018.02.004

Yang, L., Li, J., Lai, Q., Zhao, L., Li, J., Zeng, R., & Zhang, Z. (2024). Discrete element contact model and parameter calibration for clayey soil particles in the Southwest hill and mountain region. *Journal of Terramechanics*, *111*, 73–87. https://doi.org/10.1016/j.jterra.2023.10.002

Yeom, S. Bin, Ha, E., Kim, M., Jeong, S. H., Hwang, S. J., & Choi, D. H. (2019). Application of the discrete element method for manufacturing process simulation in the pharmaceutical industry. *Pharmaceutics*, *11*(8). https://doi.org/10.3390/pharmaceutics11080414

Yin, S., Taylor, A., & Wong, J. S. S. (2025). Tribology of PTFE in Hydrogen Atmosphere. *Tribology International*, *204*(December 2024), 110481. https://doi.org/10.1016/j.triboint.2024.110481

Zhu, J., Zou, M., Liu, Y., Gao, K., Su, B., & Qi, Y. (2022). Measurement and calibration of

DEM parameters of lunar soil simulant. *Acta Astronautica*, *191*(April 2021), 169–177. https://doi.org/10.1016/j.actaastro.2021.11.009

Žídek, M., Rozbroj, J., Jezerska, L., Diviš, J., Nečas, J., Zegzulka, J., & Demmler, M. (2021). Effective use of DEM to design chain conveyor geometry. *Chemical Engineering Research and Design*, *167*, 25–36. https://doi.org/10.1016/j.cherd.2020.12.017

Zimmermann, M., Herrscher, M., Schwarz, R., Schmalbach, M., Bonduelle, B., & Migliorero, G. (2013). *SEALED BRUSH GEAR MOTOR (SBGM) - QUALIFICATION TESTING WITH FOCUS ON RANDOM VIBRATION TESTING*. *September*, 25–27.

Zolotarevskiy, V., Corujeira Gallo, S., Pereira, M. P., & Barnett, M. R. (2022). Modelling of impeller-tumbler wear test with discrete element method. *Wear*, *510–511*(July), 204509. https://doi.org/10.1016/j.wear.2022.204509